(2)

主論文

Systematic Studies on Electronic and Magnetic Properties of Incommensurate Layer Compounds $(RES)_xNbS_2$ (RE=rare-earth metals; x=1.2, 0.6)

A Thesis Submitted to Kyoto University
for the Degree of Doctor of Science

by

寺嶋　太一

TERASHIMA Taichi

February, 1993

Acknowledgements

The present work has been carried out under the guidance of Professor Norimichi Kojima (Kyoto University). I would like to express my deep gratitude to him for his continuous and valuable guidance.

I also wish heartily to thank Professor Gunzi Saito (Kyoto University) for his continuous encouragement and constructive criticism.

I am grateful to Honorary Professor Ikuji Tsujikawa (Kyoto University) and Professor Koji Kosuge (Kyoto University) for their supports.

I am deeply indebted to Dr. Kazuya Suzuki (Tokyo Institute of Technology) for various helpful discussions and his continuous encouragement.

I wish to thank Professor Toshiaki Enoki (Tokyo Institute of Technology) for his valuable suggestions and keen interest. The specific heat measurements were carried out at his laboratory with the assistance of Dr. Suzuki.

I would like to express my appreciation to Professor Tadaoki Mitani, Dr. Hiroshi Kitagawa, and Dr. Hiroshi Okamoto (Institute for Molecular Science) for their collaboration in the optical reflectivity measurements and helpful suggestions.

I wish to thank Dr. Zenji Hiroi and Professor Yoshichika Bando (Kyoto University) for their collaboration in the electron microscopy experiments.

I am thankful to Dr. Takao Hirajima and Dr. Takeshi Ikeda (Kyoto University) for their collaboration in the EPMA experiments.

I would like to thank Professor Teruya Shinjo, Professor Nobuyoshi Hosoito, and Dr. Ko Mibu (Kyoto University) for their collaboration in the SQUID measurements.

The magnetic measurements with a Faraday balance were carried out at the Instrument Center, Institute for Molecular Science, with the assistance of Dr. Shunji Bandow and Mr. Masahiro Sakai.

I am grateful to Mr. Toshihiro Ban, Dr. Hideki Yamochi, and Dr. Akihiro Ohtsuka (Kyoto University) for their supports and helpful advices.

I would like to thank Dr. Hirohiko Sato for his assistance in the Seebeck coefficient measurements and useful discussions.

I wish to acknowledge the members of Professor Tsujikawa's laboratory and Professor Saito's laboratory for various discussions and their help.

Finally, I would like to express my sincere gratitude to my parents for their hearty encouragement and financial support.

CONTENTS

Chapter 1

General Introduction

§1. Introduction

Incommensurate layer compounds $(MS)_xTS_2$ (M=Sn, Pb, Bi, rare earth metals; T=Nb,Ta; $x \approx 1.2$, 0.6) [1-7] constitute a new class of intercalation compounds of group-V transition-metal dichalcogenides 2H-TS_2. Instead of usual intercalates such as 3*d* transition-metals, alkali metals, or organic molecules, metal sulfide MS layers are inserted into van der Waals gaps of host 2H-TS_2. In the $x \approx 1.2$ and the $x \approx 0.6$ compounds, the intercalate MS layer is separated by one and two TS_2 layers, respectively, and hence the two types of the compounds can be regarded as stage-1 and stage-2 intercalation compounds of 2H-TS_2. In $(MS)_xTS_2$, the intercalate MS layer forms its own lattice whose lattice periodicity is incommensurable with that of the host TS_2 layer along the one inplane direction. This peculiar structure makes these compounds classified into a family of incommensurate (misfit) layer compounds.

In this chapter, first their structures are described in some detail and then the electronic band-structure of the host material

2H-TS_2 and the rigid-band model, a key to electronic properties of intercalation compounds, are presented. The scope of this thesis is briefly described at the end of the chapter.

§2. The Structure of the Incommensurate Layer Compounds $(MS)_xTS_2$

The structure of the incommensurate layer compounds $(MS)_xTS_2$ is analyzed in a composite crystal approach, in which the total structure is divided into two subsystems, i.e., MS and TS_2. The two subsystems are , as a first (but quite good) approximation, independent of each other and hence one can take an individual unit cell on each of the two subsystems.

In Fig. 1 is shown schematically the structure of $(CeS)_{1.2}NbS_2$ determined by Wiegers *et al.* [8] in such a way. In the NbS_2 layer, niobium atoms are trigonal-prismatically coordinated by sulfur atoms as in 2H-NbS_2. An individual NbS_2 layer in $(CeS)_{1.2}NbS_2$ almost retains a hexagonal symmetry of 2H-NbS_2. The intercalate CeS layer can be related to a two-atomic-plane thick (100) slice of pristine CeS with the rock-salt structure. However, the deviation from the original structure is apparent; cerium atoms are pulled toward adjacent NbS_2 layers. The complete 1:1 matching of the two subsystems is established in the b direction, i.e., $b_{NbS_2}=b_{CeS}=b$. On the other hand, the a axes of the two subsystems are mutually incommensurate. Although the ratio a_{NbS_2}/a_{CeS} (=0.5781) is close to a rational number 4/7 (=0.5714), the essential incommensurability has been evidenced by satellite reflections in electron diffraction

patterns. An electron diffraction pattern along the [001] zone axis of $(CeS)_{1.2}NbS_2$ is shown in Fig. 2. The intense spots are easily interpreted as reflections either from the NbS_2 subsystem or from the CeS subsystem. Sequences of closely spaced satellite spots along the a^* direction are due to the incommensurability along the a axis and hence are its direct proof. It is to be noted that from the ratio a_{NbS_2}/a_{CeS} we can calculate the ideal (or structural) composition of x=1.16 (=0.5781×2) in the formula $(CeS)_xNbS_2$. [However we use an "abbreviated" formula of $(RES)_{1.2}NbS_2$ throughout for simplicity unless otherwise noted.]

Beyond the first approximation of the independent two subsystems, there exists a mutual modulation between the two subsystems; the intercalate MS layer is incommensurately modulated with the periodicity of the host TX_2 layer along the a axis and vice versa. In crystal structure determinations of the above approach, this modulation is reflected in anisotropic temperature factors of atoms. Several x-ray crystal structure determinations [8-10] including that for $(CeS)_{1.2}NbS_2$ indicate that the TS_2 layer is rather rigid, while the MS layer is the more susceptible to the mutual structural modulation.

§3. The Electronic Band-structure of the Group-V Transition-metal Dichalcogenide TX_2 and the Rigid-band Model

The electronic band-structure of the group-V transition-metal dichalcogenide 2H-TX_2 (T=Nb,Ta; X=S,Se) has extensively been studied both experimentally and theoretically. [11] In Fig. 3 is shown

the schematic density-of-states diagram for 2H-TX_2.[12] The upper valence bands are of predominantly p character of chalcogens with certain hybridization with transition-metal d states and hence labeled p/d. The Fermi level lies in a narrow (~1 eV) conduction band called the d_{z^2} band which is half-filled in pure TX_2 and is able to accept one more electron. Although earlier band-structure calculations [13,14] predicted a gap between the p/d valence band and the d_{z^2} conduction band, photoemission measurements [15,16] as well as recent self-consistent band-structure calculations [17–19] support an overlap between these two types of the bands as shown in Fig. 3. The upper d conduction bands are separated from the d_{z^2} band by a hybridization gap of about 1 eV. These bands also contain some contributions from chalcogen p states, so that they are labeled d/p.

The electronic properties of the TX_2 intercalation compounds have successfully been interpreted with the rigid-band model. [20] In the rigid-band model, it is assumed that the shape and position of the host electronic band-structure is virtually unchanged after intercalation. Intercalation results only in increased filling of the d_{z^2} conduction band due to a charge transfer from intercalate species to this band and hence the band becomes more than half-filled. Thus the rigid-band model implies that the intercalate species play only a minor role in the electronic properties of the intercalation compounds as a mere source of the electronic charge.

The rigid-band model is widely supported by experimental and theoretical investigations on the TX_2 intercalation compounds. [20] Guo and Liang have calculated and compared band structures of 2H-$LiTaS_2$ and 2H-TaS_2. [17] They have noted the two band structures

are substantially similar in terms of bond character, shape and ordering of the energy band. Beal, Liang, and their coworkers have systematically investigated optical transmission and reflectivity spectra of Li- or 3*d* transition-metal intercalated TX_2. [12,21,22] The optical spectra of the intercalated TX_2 show features very similar to those of the host TX_2 in the interband transition region of the spectra, which indicates the outlines of the electronic band-structure do not differ between the intercalated and the host materials. The electrical transport properties of the TX_2 intercalation compounds are dominated by the d_z^2 band. Parkin and Friend have carried out an intensive study on the transport and magnetic properties of the 3*d* transition-metal intercalated TX_2. [23,24] The Hall coefficients of the intercalation compounds are positive as is expected from the more than half-filled d_z^2 band. They have found the magnitudes of the Hall coefficients are consistent with a simple valence argument. That is, if the valence state of the intercalate 3*d* transition-metal ion M is $+v$, then the d_z^2 band contains $(1-xv)$ holes per unit formula of M_xTX_2. Thus calculated carrier concentrations have shown good agreements with the observed Hall coefficients.

In these studies, non-rigid-band effects have also been observed. The interband transitions in the optical spectra of the intercalation compounds are broadened, compared with those of the host materials. Parkin and Beal have attributed it to increased bandwidths due to increased bonding between the layers in the intercalation compounds. [22] Parkin and Friend have observed large spin-disorder resistivities of order of $100\mu\Omega$cm for the 3*d* transition-metal intercalation compounds, which indicates there

exists a strong interaction between the local $3d$ moments and the d_z^2 carriers. [24] However, these non-rigid-band effects are minor corrections to the model and the overall validity of the rigid-band model in the TX_2 intercalation compounds model is now widely accepted.

The only exception is those compounds fully intercalated with post-transition metals such as $SnTaS_2$. In this case, the intercalate species are dense in the intercalate layer due to their large concentration and hence form their own energy-band. The electronic band-structure calculation for $SnTaS_2$ has shown Sn $5p_x$ and $5p_y$ states exhibit strong metal-metal bonding in the intercalate layer and that the Fermi level is crossed by a very wide band composed of these states, which has been confirmed by angle-resolved photoemission spectra. [18]

§4. The Scope of This Thesis

Although the incommensurate layer compounds have the structure reminiscent of the intercalation compound, it does not necessarily result in the fact that their electronic structures are interpreted as intercalation compounds. In the usual intercalation compounds, the intercalate species are molecules or metal ions, which are sufficiently separated from each other in the intercalate plane (except the fully intercalated compounds with post-transition metals). Hence the rigid-band model which claims that the electronic properties are exclusively ruled by the host electronic structures is rather plausible. On the other hand, in the

incommensurate layer compounds, the intercalate layer is a part of another compounds. Especially, in the case of the rare-earth based compounds $(RES)_xTS_2$ (RE=rare-earth metals), some of which we are going to deal with, pristine rare-earth sulfides RES are metallic compounds. Hence it is interesting to examine the validity of the rigid-band model in them. Although Wiegers and his coworkers have already reported some transport properties of several of the stage-1 compounds $(MS)_{1.2}TS_2$, [2,8,10,25] their electronic structures are not yet understood enough.

In this study, the rare-earth based stage-1 compounds $(RES)_{1.2}NbS_2$ (RE=La,Ce,Pr,Nd,Sm,Gd,Dy,Er,Yb) and the stage-2 compounds $(LaS)_{0.6}NbS_2$ and $(CeS)_{0.6}NbS_2$ have been synthesized and their electronic structures have been investigated by means of electrical resistivity, Seebeck coefficient, and optical reflectivity measurements. The author has put his emphasis on a stage-dependent study; the stage-2 compounds $(LaS)_{0.6}NbS_2$ and $(CeS)_{0.6}NbS_2$ are novel compounds of this study. The stage-dependent study is useful for investigating the rigid-band model, since different stages immediately correlate with different charge transfer rates and hence different band fillings. In addition, the optical measurements employed in this study are a more direct probe into the electronic structure than the transport measurements.

Another interest comes from the fact that these compounds can be a model compound for quasi two-dimensional magnetism; the magnetic RES layer is separated by the non-magnetic metallic NbS_2 layer in $(RES)_xNbS_2$. Careful choice of rare earth elements may give

an opportunity to realize model systems for various types of magnetic interaction, e.g. the Ising, XY, and Heisenberg models, with different spin values. The RKKY-type indirect exchange interaction mediated by the conduction electron may play a role in the weak magnetic interaction between the intercalate RES layers. The RKKY interaction is of long-range and oscillates with distance. Such interaction may give rise to a long-period magnetic structure along the *c* axis. The author has focused on the Ce based compounds $(CeS)_{1.2}NbS_2$ and $(CeS)_{0.6}NbS_2$ and investigated the magnetic interaction and ordering in them through the magnetic susceptibility and magnetization measurements. A quasi two-dimensional nature of the magnetic spin system in $(CeS)_{1.2}NbS_2$ has also been verified by magnetic specific heat measurements.

Finally, the most prominent feature in the incommensurate layer compounds is, of course, the structural incommensurability along the *a* axis. It is natural and valuable to pursue its influence on their physical properties. Efforts in this direction have also been made; attempts are done to correlate some aspects of their electronic and magnetic properties with the structural incommensurability.

The preparation and characterization of the stage-1 compounds $(RES)_{1.2}NbS_2$ (RE=La,Ce,Pr,Nd,Sm,Gd,Dy,Er,Yb) and the stage-2 compounds $(LaS)_{0.6}NbS_2$ and $(CeS)_{0.6}NbS_2$ are described in chapter 2. Electron diffraction observations of $(LaS)_{0.6}NbS_2$, which is a novel compound of the present study together with $(CeS)_{0.6}NbS_2$, are reported in chapter 3. The electronic transport properties of

$(RES)_{1.2}NbS_2$ and $(RES)_{0.6}NbS_2$ are investigated in chapter 4. The optical reflectivity spectra of $(CeS)_{1.2}NbS_2$ and $(CeS)_{0.6}NbS_2$ are presented in chapter 5. The magnetic properties of $(CeS)_{1.2}NbS_2$ and $(CeS)_{0.6}NbS_2$ are investigated through the magnetic susceptibility and magnetization measurements in chapter 6 and through the magnetic specific heat of the former compound in chapter 7. Some general conclusions of this thesis will be drawn in chapter 8.

References

1) L. Guemas, P. Rabu, A. Meerschaut, and J. Rouxel: Mater. Res. Bull. **23** (1988) 1061.

2) G. A. Wiegers, A. Meetsma, R. J. Haange, and J. L. de Boer: Mater. Res. Bull. **23** (1988) 1551.

3) A. Meerschaut, P. Rabu, and J. Rouxel: J. Solid State Chem. **78** (1989) 35.

4) Y. Gotoh, M. Onoda, K. Uchida, Y. Tanaka, T. Iida, H. Hayakawa, and Y. Oosawa: Chem. Let. (1989) 1559.

5) Y. Oosawa, Y. Gotoh, and M. Onoda: Chem. Let. (1989) 1563.

6) K. Suzuki, N. Kojima, T. Ban, and I. Tsujikawa: J. Phys. Soc. Jpn. **59** (1990) 266.

7) A. Meerschaut, L. Guemas, C. Auriel, and J. Rouxel: Eur. J. Solid State Inorg. Chem. **27** (1990) 557.

8) G. A. Wiegers, A. Meetsma, R. J. Haange, and J. L. de Boer: J. Solid State Chem. **89** (1990) 328.

9) A. Meetsma, G. A. Wiegers, R. J. Haange, and J. L. de Boer: Acta. Cryst. A **45** (1989) 285.

10) J. Wulff, A. Meetsma, S. van Smaalen, R. J. Haange, J. L. de Boer, and G. A. Wiegers: J. Solid State Chem. **84** (1990) 118.

11) E. Doni and R. Girlanda: *Electronic Structure and Electronic Transitions in Layered Materials*, ed. V. Grasso (D. Reidel, Dordrecht, 1986), p.1.

12) A. R. Beal and S. Nulsen: Philos. Mag. B **43** (1981) 985.

13) L. F. Mattheiss: Phys. Rev. B **8** (1973) 3719.

14) G. Wexler and A. M. Woolley: J. Phys. C: Solid State Phys. **9** (1976) 1185.

15) N. V. Smith and M. M. Traum: Phys. Rev. B **11** (1975) 2087.

16) F. Minami, M. Sekita, M. Aono., and N. Tsuda: Solid State Commun. **29** (1979) 459.

17) G. Y. Guo and W. Y. Liang: J. Phys. C: Solid State Phys. **20** (1987) 4315.

18) J. Dijkstra, E. A. Broekhuizen, C. F. van Bruggen, C. Haas, R. A. de Groot, and H. P. van der Meulen: Phys. Rev. B **40** (1989) 12111.

19) P. Blaha: J. Phys.: Condens. Matter **3** (1991) 9381.

20) R. H. Friend and A. D. Yoffe: Adv. Phys. **36** (1987) 1.

21) A. R. Beal and W. Y. Liang: Philos. Mag. **33** (1976) 121.

22) S. S. P. Parkin and A. R. Beal: Philos. Mag. B **42** (1980) 627.

23) S. S. P. Parkin and R. H. Friend: Philos. Mag. B **41** (1980) 65.

24) S. S. P. Parkin and R. H. Friend: Philos. Mag. B **41** (1980) 95.

25) G. A. Wiegers and R. J. Haange: J. Phys.: Condens. Matter **2** (1990) 455.

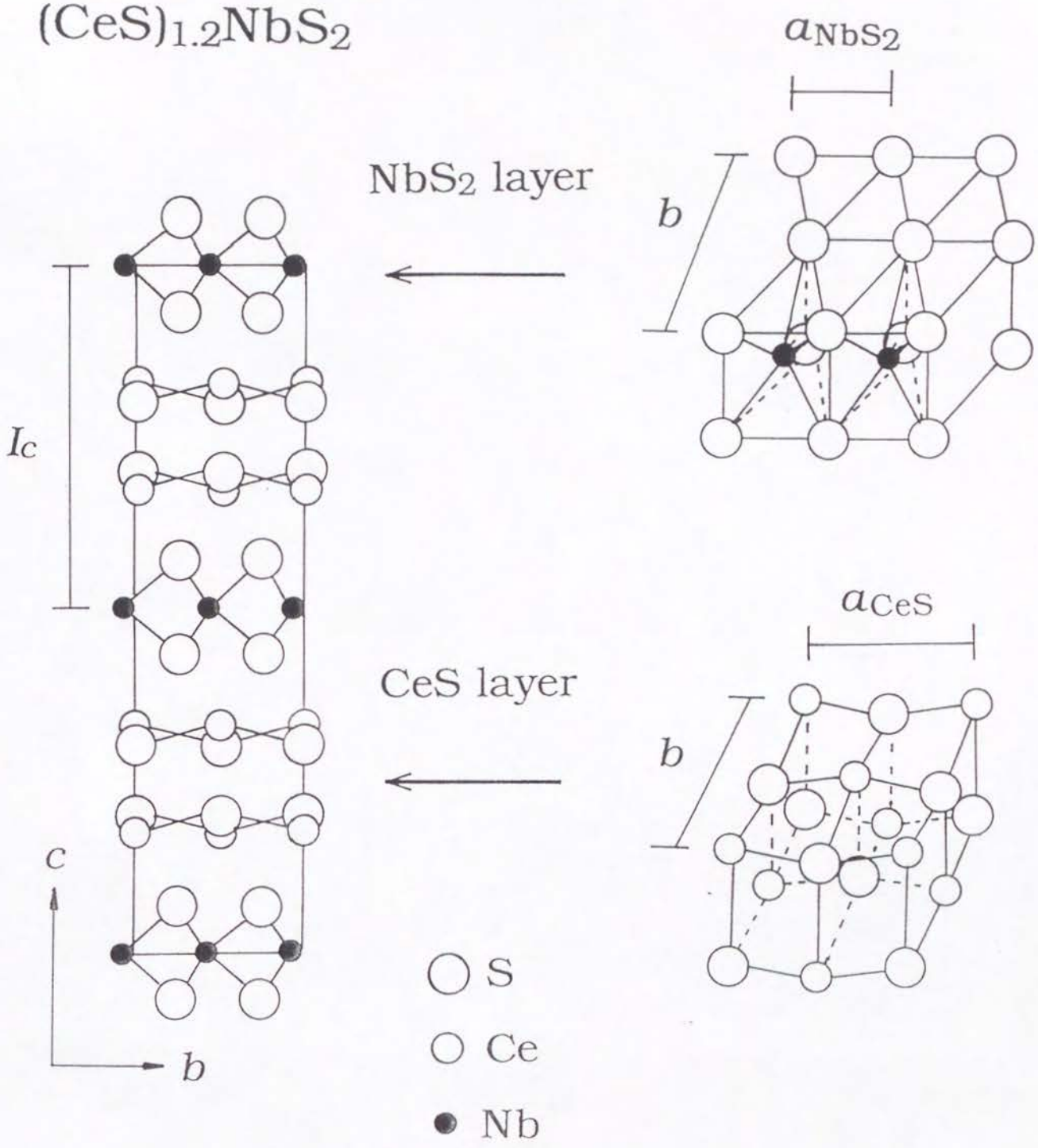

Fig. 1. The incommensurate layer compound $(CeS)_{1.2}NbS_2$ is composed of the two structural subsystems, CeS and NbS_2. Each of the two subsystems is described in a centered orthorhombic lattice; the CeS subsystem has a space group $Cm2a$ with a_{CeS}=5.727Å, b_{CeS}=5.765Å, c_{CeS}=11.41Å, and Z=4, while the NbS_2 subsystem has a space group $Fm2m$ with a_{NbS_2}=3.311Å, b_{NbS_2}=5.765Å, c_{NbS_2}=22.82Å, and Z=4. [8] Note that $b_{CeS}=b_{NbS_2}$ (=b) and that $c_{CeS}=c_{NbS_2}/2$ (=I_c).

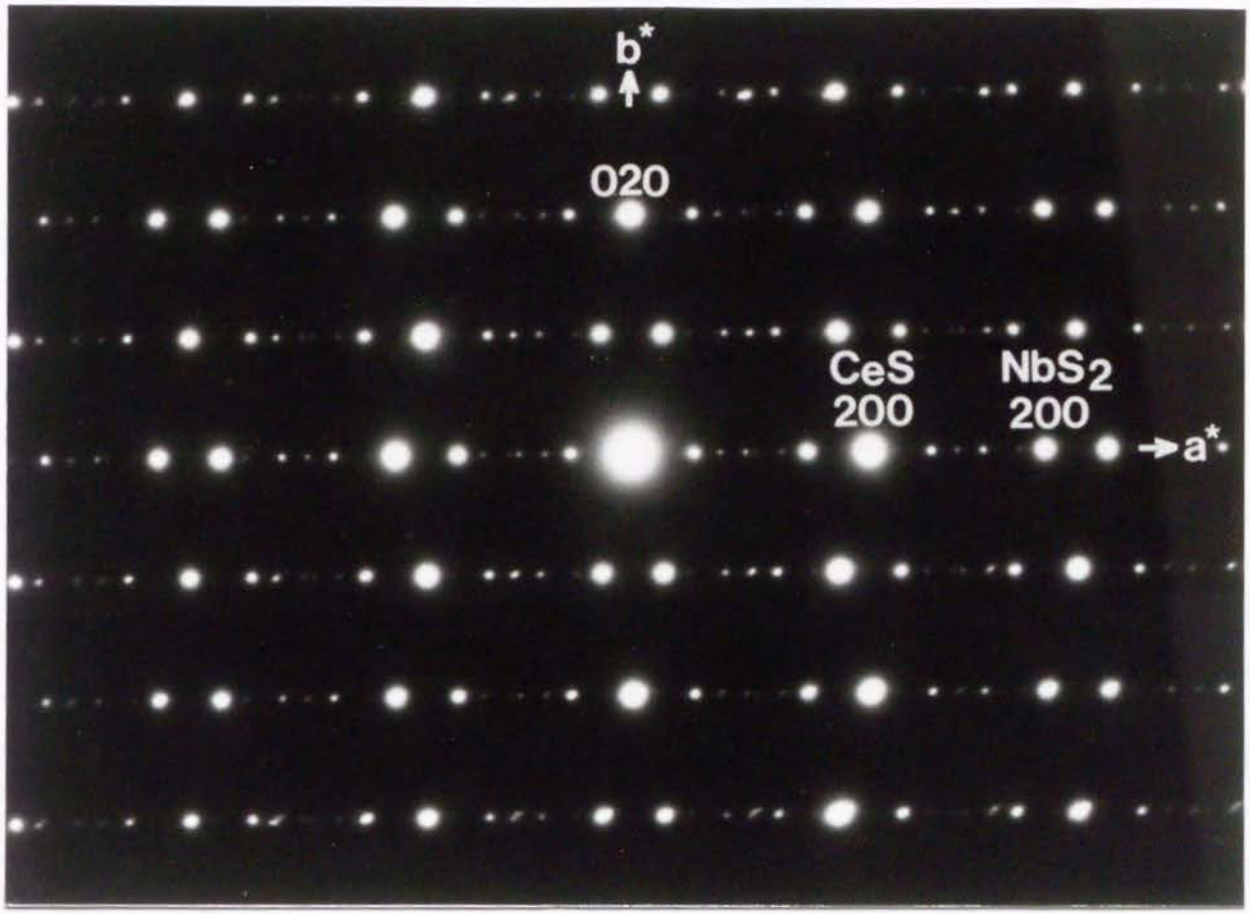

Fig. 2. Electron diffraction pattern along the [001] zone axis of $(CeS)_{1.2}NbS_2$. The intense spots are reflections from the NbS_2 subsystem or from the CeS subsytem. The 020 reflection is common to both the subsystems. Sequences of closely and not eqally spaced satellite spots along the a^* direction is due to the incommensurability along the a axis.

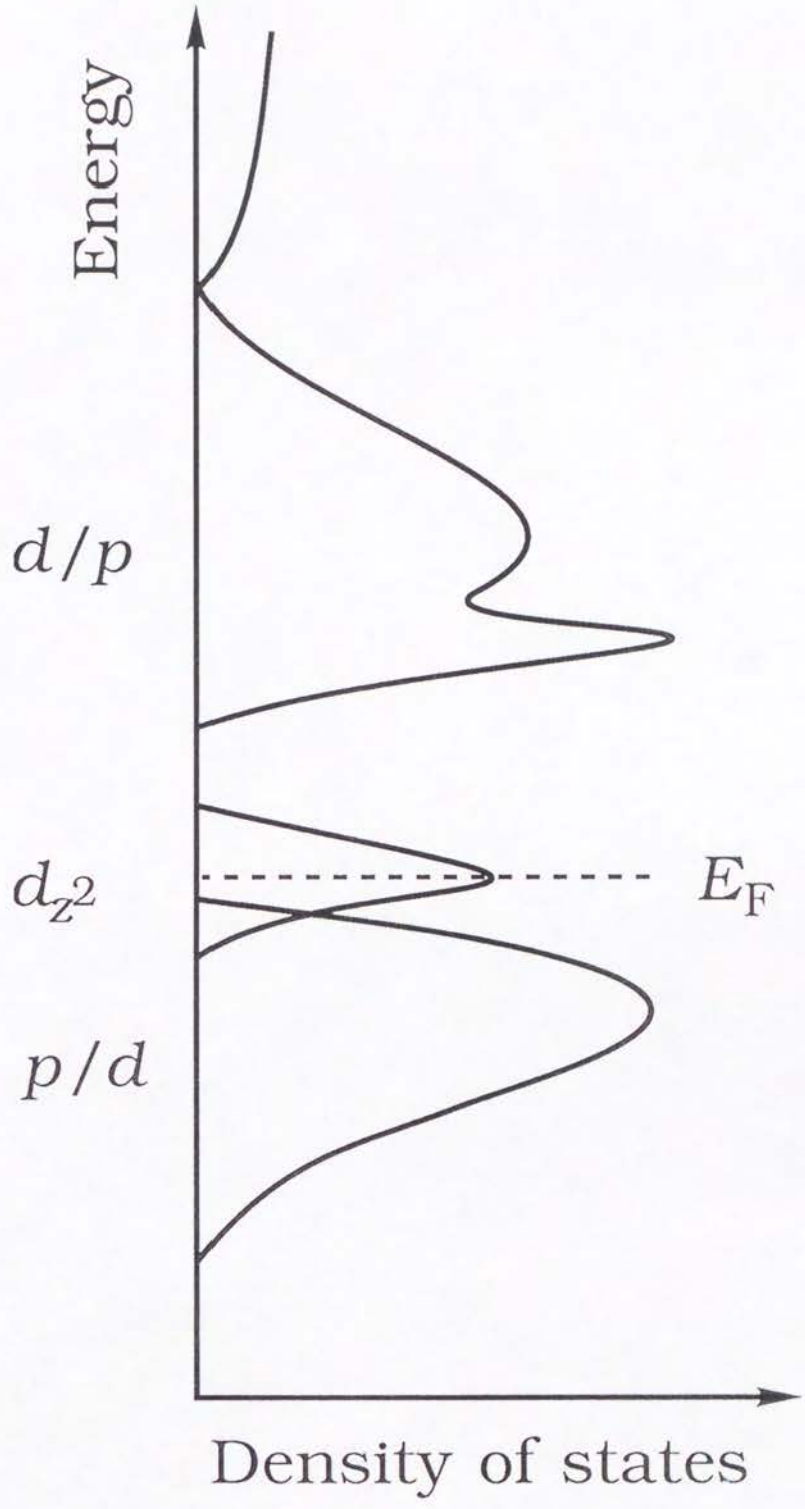

Fig. 3. The schematic density-of-states diagram for the transition-metal dichalcogenides 2H-TX_2 (T=Nb,Ta; X=S,Se). [12]

Chapter 2

Sample Preparation and Characterization

§1. Sample Preparation

Crystals of the stage-1 compounds $(RES)_{1.2}NbS_2$ (RE=La, Ce, Pr, Nd, Sm, Gd, Dy, Er, Yb) were prepared from the constituent elements. A nearly stoichiometric mixture of RE (99.9%), Nb (99.96%), and S (99.999%) in an about 1:1:3 molar ratio was sealed with iodine (5mg/cc) in an evacuated quartz tube and heated in a temperature gradient of ca. 1000–900°C for one month [the purities indicated in the parentheses are nominal (commercial) ones]. Crystals of dimensions up to $2\times2\times0.05$ mm^3 were obtained at the high temperature zone where the starting powder was placed. The addition of iodine was necessary for crystal growth. In early attempts, the starting mixture without iodine was pre-reacted at 950°C for one week prior to the crystal growth. This procedure was however found unnecessary and later omitted.

Crystals of the stage-2 compounds $(LaS)_{0.6}NbS_2$ and $(CeS)_{0.6}NbS_2$ were prepared in the same way but from an off-stoichiometric mixture of the constituent elements. The molar ratio of the starting mixture was 1:6:12 for $(LaS)_{0.6}NbS_2$ and 1:4:8 or 1:2:5 for $(CeS)_{0.6}NbS_2$. Small crystals of $1\times0.5\times0.02$ mm^3 were obtained as minor product.

Detailed conditions for each preparation batch are summarized in Table I.

§2. Sample Characterization

Energy-dispersive x-ray microanalyses were carried out on $(LaS)_{1.2}NbS_2$ and $(LaS)_{0.6}NbS_2$. The $L\alpha$ lines were used to determine the concentrations of La and Nb, while the $K\alpha$ lines were used to determine the sulfur content. The standard materials were $\underline{La}F_3$, $\underline{Nb}$ metal, and $Fe\underline{S}_2$. Due to strong overlap between the sulfur *K*-lines and the niobium *L*-lines and difficulty in deconvoluting the lanthanum *L*-lines, the accuracy of the analyses was less than usual and estimated at ca. ±5 (relative) %. The found composition are close to the structurally expected ideal ones, $(LaS)_{1.14}NbS_2$ and $(LaS)_{0.57}NbS_2$ (Table II).

The stage index and staging fidelity of crystals were characterized using (00*l*) x-ray diffraction. The samples used for the measurements were verified to be pure and single-staged according to the x-ray spectra.

The interlayer repeat distances I_c of the stage-1 compounds $(RES)_{1.2}NbS_2$ determined from the (00*l*) x-ray spectra are plotted as

a function of the rare-earth element in Fig.1, where the lattice parameters a of pristine rare-earth monosulfides RES [1-5] are also shown. In pristine RES, an expansion of the lattice parameter can be seen at RE=Sm,Eu,Yb due to the divalent RE ion. On the other hand, the interlayer repeat distance of $(RES)_{1.2}NbS_2$ shows only a monotonous decrease due to the lanthanoid contraction, which indicates that the RE ions in $(RES)_{1.2}NbS_2$ including the RE=Sm,Yb compounds have a usual trivalent state. The interlayer repeat distances of $(LaS)_{1.2}NbS_2$ and $(CeS)_{1.2}NbS_2$ are in good agreement with the values of 11.51 Å and 11.41 Å reported by Wiegers *et al.*, respectively. [6]

The interlayer repeat distances of the stage-2 compounds, $(LaS)_{0.6}NbS_2$ and $(CeS)_{0.6}NbS_2$, are 17.47 Å and 17.35 Å, respectively. The difference in I_c between the stage-1 and stage-2 compounds is 5.98 Å and 5.94 Å for the La and Ce compounds, respectively. These values are close to the one layer thickness of 2H-NbS_2 (5.98 Å). [7]

References

1) E. Bucher, K. Andres, F. J. Di Salvo, J. P. Maita, A. C. Gossard, A. S. Cooper, and G. W. Hull Jr.: Phys Rev. B **11** (1975) 500.

2) E. Bucher, V. Narayaanmurti, and A. Jayaraman: J. Appl. Phys. **42** (1971) 1741.

3) G. M. Loginov, V. M. Sergeeva, and M. F. Bryzhina: Sov. Phys. JETP **32** (1971) 1054.

4) P. Wachter: Phys. Rep. **44** (1978) 159.

5) F. Hulliger, B. Natterer, and H. R. Ott: J. Magn. & Magn. Mater. **8** (1978) 87.

6) G. A. Wiegers, A. Meetsma, R. J. Haange, and J. L. de Boer: J. Solid State Chem. **89** (1990) 328.

7) W. G. Fisher and M. J. Sienko: Inorg. Chem. **19** (1980) 39.

Table I. Sample preparation conditions.

RE	batch #	starting ratio RE:Nb:S	pre-reaction temperature	crystal growth temperature
stage-1 $(RES)_{1.2}NbS_2$				
La	#19	1 : 1 : 3	950°C	1000–900°C
	#28	1 : 1 : 3	950°C	1000–900°C
Ce	#10	1 : 1 : 3	950°C	950–850°C
	#15	1 : 1 : 3	950°C	950–850°C
	#18	1 : 1 : 3	950°C	1000–900°C
	#25	1 : 1 : 3	950°C	1000–900°C
	#26	1 : 1 : 3	950°C	1050–950°C
	#101	1 : 1 : 3	—	1050–880°C
Pr	#1	1.2 : 1 : 3.2	—	1000–900°C
Nd	#1	1 : 1 : 3	—	1050–950°C
Sm	#1	1 : 1 : 3	—	1050–950°C
Gd	#1	1 : 1 : 3	—	1050–950°C
Dy	#1	1 : 1 : 3	—	1050–950°C
Er	#1	1.2 : 1 : 3.2	—	1000–900°C
Yb	#1	1 : 1 : 3	950°C	1000–850°C
	#2	1.2 : 1 : 3.5	—	1000–900°C
stage-2 $(RES)_{0.6}NbS_2$				
La	#30	1 : 6 : 12	950°C	1000–900°C
Ce	#103	1 : 4 : 8	—	1000–900°C
	#106	1 : 2 : 5	—	1000–900°C

Table II. Results of the EPMA analyses for $(LaS)_{1.14}NbS_2$ and $(LaS)_{0.57}NbS_2$.

	La (%)	Nb (%)	S (%)
stage-1 $(LaS)_{1.14}NbS_2$			
calc.	45.0	26.4	28.6
found	43.5	26.0	28.2
stage-2 $(LaS)_{0.57}NbS_2$			
calc.	32.4	36.5	31.1
found	29.3	37.7	30.8

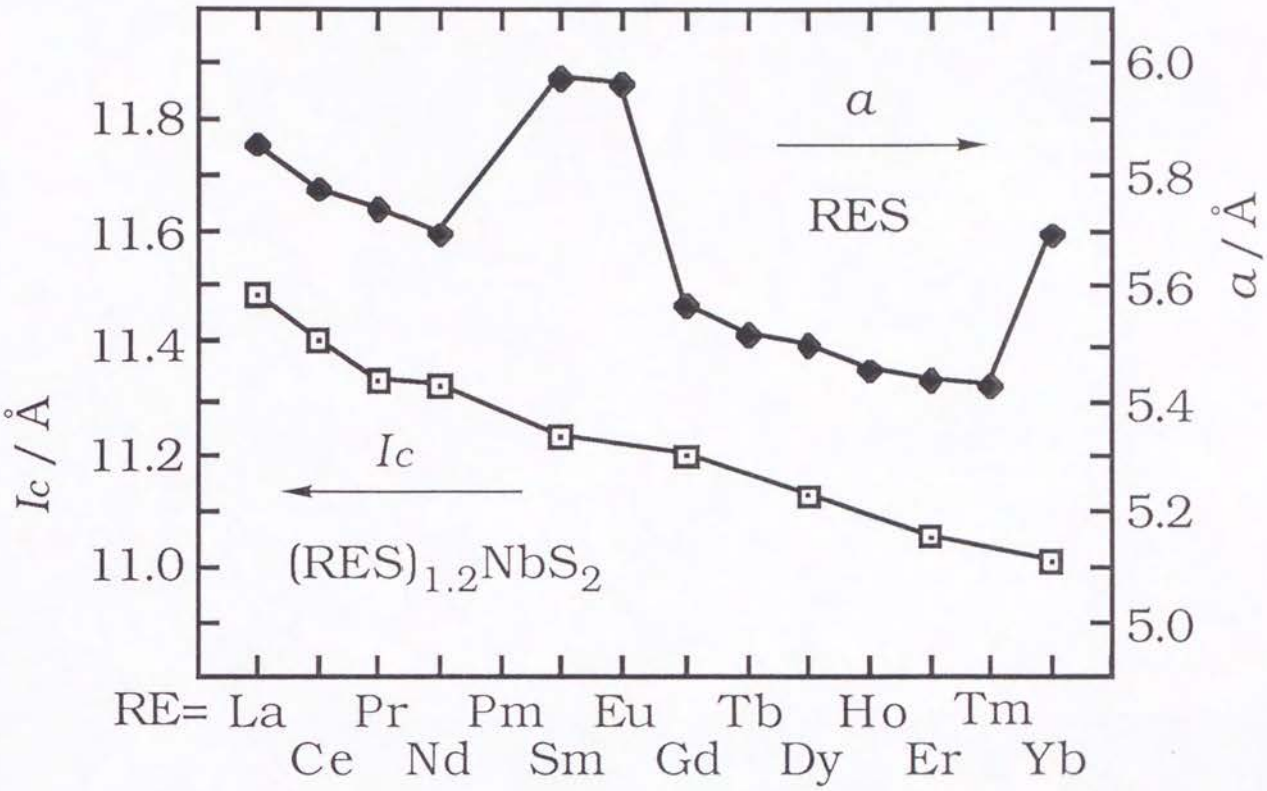

Fig. 1. The interlayer repeat distances I_c of the stage-1 compounds $(RES)_{1.2}NbS_2$ as a function of the rare-earth element RE. The lattice parameters a of rare-earth monosulfides RES (the NaCl structure) [1–5] are shown together.

Chapter 3

Electron Diffraction and Microscopy Observations of the Stage-2 Compound $(LaS)_{0.6}NbS_2$

§1. Introduction

The structural details in various stage-1 compounds $(MS)_{1.2}TS_2$ (M=Sn, Pb, Bi, rare earth metals; T=Nb,Ta) have extensively been investigated by means of both x-ray and electron diffraction. [1-5] On the other hand, as far as the stage-2 compounds concern, there has been little information about their structures; in most cases, only the interlayer repeat distances have been reported. [6-8] The x-ray structure determination has been performed only on $(PbS)_{1.14}(NbS_2)_2$ [$(PbS)_{0.57}NbS_2$ in our nomenclature] by A. Meerschaut *et al.* [9] In this chapter, we report the electron microscopy observations of a new stage-2 compound $(LaS)_{0.57}NbS_2$. Possible structure models of the compound will be discussed.

§2. Experimental

Crystals of $(LaS)_{0.57}NbS_2$ were prepared with the method described in chapter 2. The detailed preparation conditions are shown in Table I of chapter 2.

Electron microscopy specimens were prepared by successively cleaving crystal platelets with an adhesive tape. Thus obtained specimens were thin foils elongated along the *b* axis. They were examined in JEOL 2000EX microscope operating at 200 kV. Because of the lamellar morphology, observations were mostly limited to those along the [001] zone axis. In some cases, however, edges of foils were curled up so as to enclose the *b* axis, which enabled us to observe [100] zone axis patterns and images.

§3. Results

3.1 The [001] zone axis

Figure 1 shows an electron diffraction pattern along the [001] zone axis, which much resembles those reported for the stage-1 compounds such as $(LaS)_{1.14}NbS_2$.[4,5] Intense spots are easily interpreted as reflections either from the pseudo-hexagonal layer (the NbS_2 layer) or from the pseudo-tetragonal layer (the LaS layer). These main reflections exhibit a systematic reflection condition indicative of the C-centering of both the sublattices, i.e., *hk*0 $h+k$=even. The reciprocal lattice vectors of the two kinds of layers coincide in one direction (the *b* direction). Taking centered

rectangular unit cells on this projection, the cell dimensions of the two kind of layers are a_1=3.32Å, a_2=5.86Å, and $b'=b_1'=b_2'$=5.76Å, where the subscripts 1 and 2 refer to the NbS_2 and the LaS sublattice, respectively. The parameter b' is the projected b axis, i.e., $b'=b\sin\alpha$. Since the monoclinic angle α differs only slightly from 90° (see below), b' practically equals to b within our experimental accuracy. From the inverse of the ratio a_2/a_1=1.76, we can derive the ideal (or structural) composition of x=0.57 in the formula $(LaS)_xNbS_2$. Although this ratio is close to a rational number 7/4, it is essentially irrational. This incommensurability along the a axis is reflected by sequences of closely and not equally spaced satellite spots along the a^* direction. These satellite spots can be interpreted as arising from multiple diffractions, or as a result of the mutual modulation between the two kinds of layers, as discussed by Kuypers *et al.* [4,5] Whichever interpretation is taken, the diffraction vector $\boldsymbol{q}$ should be expressed as $\boldsymbol{q}=H\boldsymbol{a}_1^*+K\boldsymbol{a}_2^*+L\boldsymbol{b}^*+M\boldsymbol{c}^*$ (H,K,L,M; integer), as really observed [Fig. 1(b)]. The systematic reflection condition is observed; $H+K+L$=2n for $HKL0$ reflections.

Figure 2(a) shows a typical lattice image along the [001] zone axis. The pseudo-hexagonal pattern of dots can be interpreted as representing the NbS_2 layer. Rows of the dots running parallel to the a axis are separated by $b'/2$. The spacing of the dots in the rows equals a_1. In each row along the a axis, four or three bright dots and three or four less bright dots alternate in an almost periodic way, which is consistent with an approximate supercell with a dimension of $7a_1$ ($\approx 4a_2$) along the a axis. The phase of the periodic brightness modulation in one row differs by π from that in the adjacent row. An

interesting lattice image [Fig. 2(b)] was obtained at a different area within the same foil as Fig. 2(a). In this image the pseudo-hexagonal pattern (region A) smoothly varies into the pseudo-tetragonal pattern (region B). Image simulations for the stage-1 compound $(LaS)_{1.14}NbS_2$ have revealed that the pseudo-hexagonal or the pseudo-tetragonal pattern, which respectively represent the NbS_2 or the LaS layer, can be observed according to thickness of foils. [4,5] However, there seems to be some doubt whether this explanation is applicable for the present image. The transitional region spreads over only a few dots and the transition is very smooth. There is no reason to expect the foil thickness substantially changes within such a narrow region.

3.2 The [100] zone axis

Figure 3 shows an electron diffraction pattern along the [100] zone axis. The spots are closely spaced along the c^* axis and shows the interlayer repeat distance of 17.4Å consistent with the $00l$ x-ray diffractogram. Trying connecting the spots horizontally, it is evident that the b^* axis forms an oblique angle with the c^* axis, i.e., $\alpha^* \neq 90°$. Two possible cell choices are indicated in Fig. 3, and the monoclinic angle α^* is 84° or alternatively 87°. Streaks along the a^* axis are observed not only between the $0kl$ (k=even) spots but also on the $0kl$ (k=odd) rows, which may indicate disorder along the c axis and violation of the C-centering. However the fact that the $00l$ x-ray diffractograms show sharp peaks casts some doubt whether these are intrinsic or caused by the preparation procedure. Figure 4 shows the corresponding lattice image. This image shows (001) layer stacking

with the interlayer repeat distance of ca. 17Å. The spacing of dots resolved in horizontal rows is 2.9Å, which corresponds to $b/2$.

§4. Discussion

On the basis of the structure data of the stage-1 compounds $(MS)_{1.2}TS_2$, Wiegers *et al.* [10] have proposed a simple building principle in these compounds. According to them, the metal atoms M of the MS layer fall in grooves between sulfur atom rows of the adjacent TS_2 layer which run parallel to the a axis. This building principle has succeeded in explaining the occurrence of orthorhombic and monoclinic (or triclinic) symmetries in the stage-1 compounds. The spacings of the grooves are $b/2$, which gives rise to other variations in the structure; each layer of one kind can stack either just vertically above the preceding one or displaced by $b/2$ relative to the preceding one. For example, in $(LaS)_{1.14}NbS_2$ the LaS layer stacks vertically without relative shift, resulting in a C-centered orthorhombic lattice, whereas the NbS_2 layer stacks with systematic shift of $b/2$, resulting in a F-centered orthorhombic lattice with a doubled c dimension. However, it is to be noted that Kuypers *et al.* have argued from their electron microscopy observations that such a relative shift of successive layers is not very systematic and that the region with the systematic shift and that with no shift coexist even within one crystal foil. [5]

The structure of the stage-2 compound $(PbS)_{1.12}(NbS_2)_2$ [9] suggests that the building principle above is also applicable for stage-2 compounds. We therefore discuss possible structures of the stage-

2 compound $(LaS)_{0.57}NbS_2$ based on this principle. We assume that the two consecutive NbS_2 layers between two successive intercalate layers stack in the same way as two adjacent layers of 3R-NbS_2, since this arrangement is really observed in $(PbS)_{1.12}(NbS_2)_2$. Such a double NbS_2 layer is shown in Fig. 5. It is easily seen that the grooves of one side of the double layer are displaced by $b/3$ relatively to those on the other side. Since the spacings of the grooves are $b/2$, there exist two different stacking modes analogous to the C-centering and the F-centering in the stage-1 compound, i.e., two successive layers of one kind can be displaced by $b/3$ or $b/6$ ($=b/2-b/3$). Accordingly one obtains four structure models A-D for $(LaS)_{0.57}NbS_2$ as shown in Fig. 6. The NbS_2 sublattice in all the models and the LaS sublattice in the models A and D are described in a C-centered monoclinic cell, while the LaS sublattice in the models B and C is described in an F-centered monoclinic cell with a doubled c dimension in order to keep the c direction common to the NbS_2 and the LaS sublattice.

We restrict ourselves to the projection along the [100] zone axis. This corresponds to neglecting a distinction between open and solid circles in the figures, and hence each projection of the four structures cannot be distinguished from another. The c axis can be chosen as $\boldsymbol{c}=\boldsymbol{c}_{\perp}-\boldsymbol{b}/3$ or $\boldsymbol{c}=\boldsymbol{c}_{\perp}-\boldsymbol{b}/6$, where $\boldsymbol{c}_{\perp}$ is the vector perpendicular to the ab plane with the length of the interlayer repeat distance I_c. The monoclinic angle α can be calculated by $\alpha=90°+\arctan(b/3I_c)$ or $\alpha=90°+\arctan(b/6I_c)$, respectively. Using the values of I_c=17.47Å and b=5.76Å, α is 96.1° or 93.1° and the relation $\cos\alpha^*=-\cos\alpha$ yields α^*=83.7° or 86.9°. These values are in good

agreement with the experimental values calculated from the [100] axis pattern.

§5. Summary and Conclusions

We have carried out the electron diffraction and microscopy observations of a new incommensurate layer compound $(LaS)_{0.57}NbS_2$ with a stage-2 structure. The [001] zone axis electron diffraction pattern and lattice image clearly show the incommensurability in the structure. The monoclinic angle α^* of 84° or 87° observed in the [100] zone axis pattern is successfully explained by the structure models based on the building principle of Wiegers *et al.* [10]

References

1) G. A. Wiegers, A. Meetsma, R. J. Haange, and J. L. de Boer: J. Solid State Chem. **89** (1990) 328.

2) J. Wulff, A. Meetsma, S. van Smaalen, R. J. Haange, J. L. de Boer, and G. A. Wiegers: J. Solid State Chem. **84** (1990) 118.

3) A. Meetsma, G. A. Wiegers, R. J. Haange, and J. L. de Boer: Acta Crstallogr. A **45** (1989) 285.

4) S. Kuypers, G. Van Tendeloo, J. Van Landuyt, and S. Amelinckx: Acta Crystallogr. A **45** (1989) 291.

5) S. Kuypers, J. Van Landuyt, and S. Amelinckx: J. Solid State Chem. (1990) 212.

6) L. Guemas, P. Rabu, A. Meerschaut, and J. Rouxel: Mater. Res. Bull. **23** (1988) 1061.

7) K. Suzuki, N. Kojima, T. Ban, and I. Tsujikawa: J. Phys. Soc. Jpn. **59** (1990) 266.

8) Y. Oosawa, Y. Gotoh, and M. Onoda: Chem. Let. (1989) 1563.

9) A. Meerschaut, L. Guemas, C. Auriel, and J. Rouxel: Eur. J. Solid State Inorg. Chem. **27** (1990) 557.

10) G. A. Wiegers, A. Meetsma, S. van Smaalen, R. J. Haange, and J. L. de Boer: Solid State Commun. **75** (1990) 689.

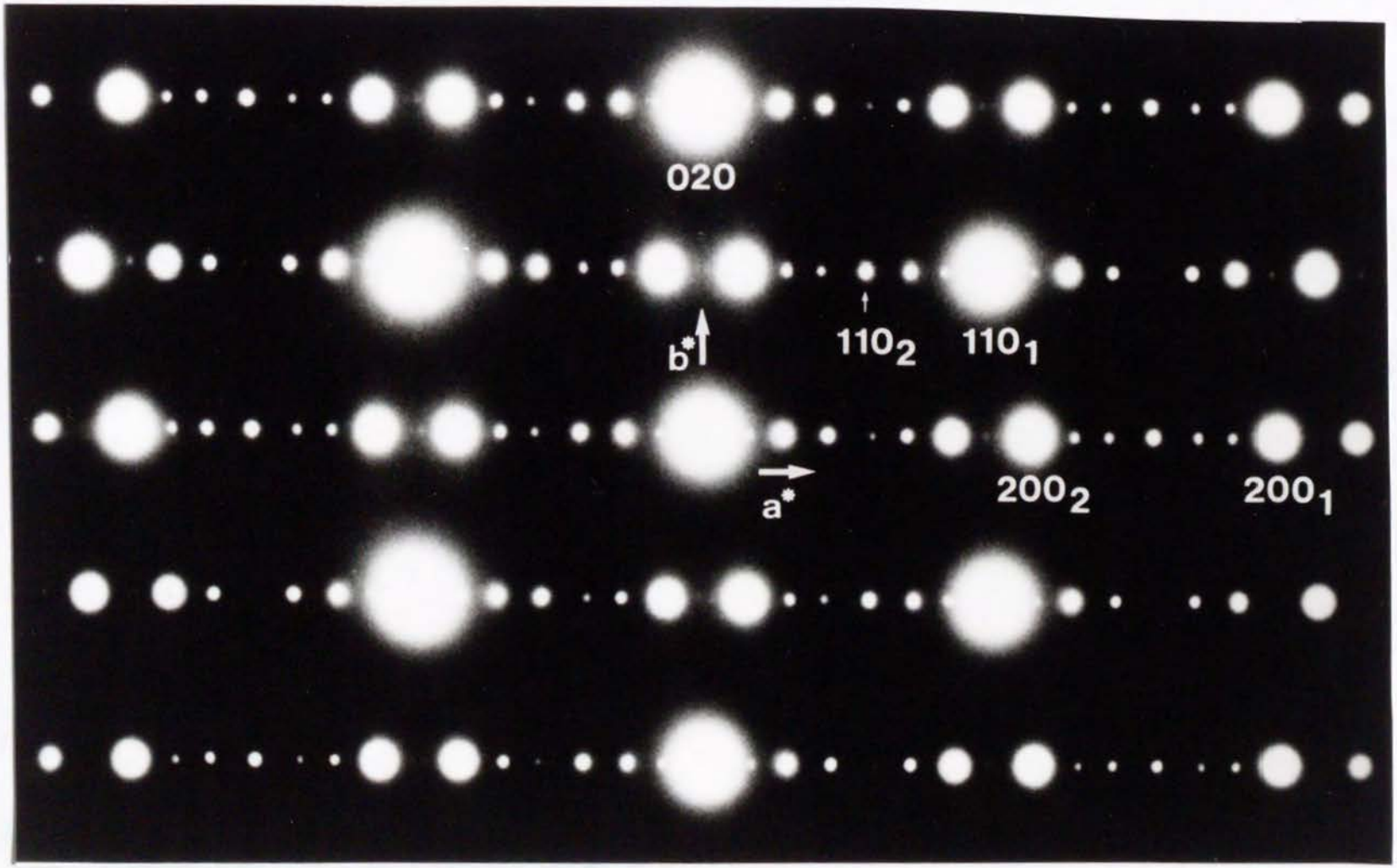

Fig. 1(a). Electron diffraction pattern along the [001] zone axis of $(LaS)_{0.57}NbS_2$. Intense spots are reflections from the NbS_2 layer (1) or from the LaS layer (2). The 020 reflection is common to both the layers.

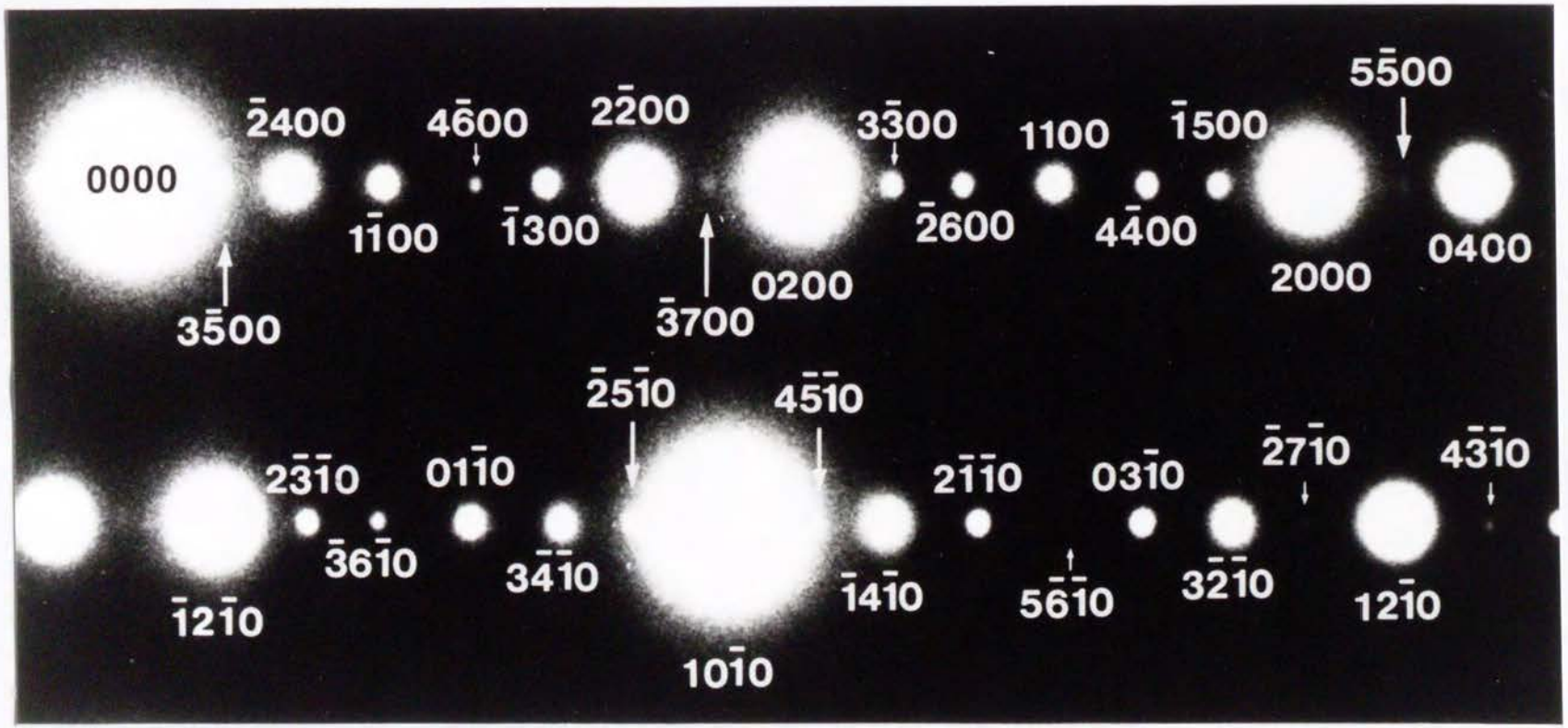

Fig. 1(b). Enlargement of Fig. 1(a). Satellite spots are indexed by four integers H,K,L,M, where the diffraction vector $\boldsymbol{q}$ is expressed as $\boldsymbol{q}=H\boldsymbol{a}_1^*+K\boldsymbol{a}_2^*+L\boldsymbol{b}^*+M\boldsymbol{c}^*$.

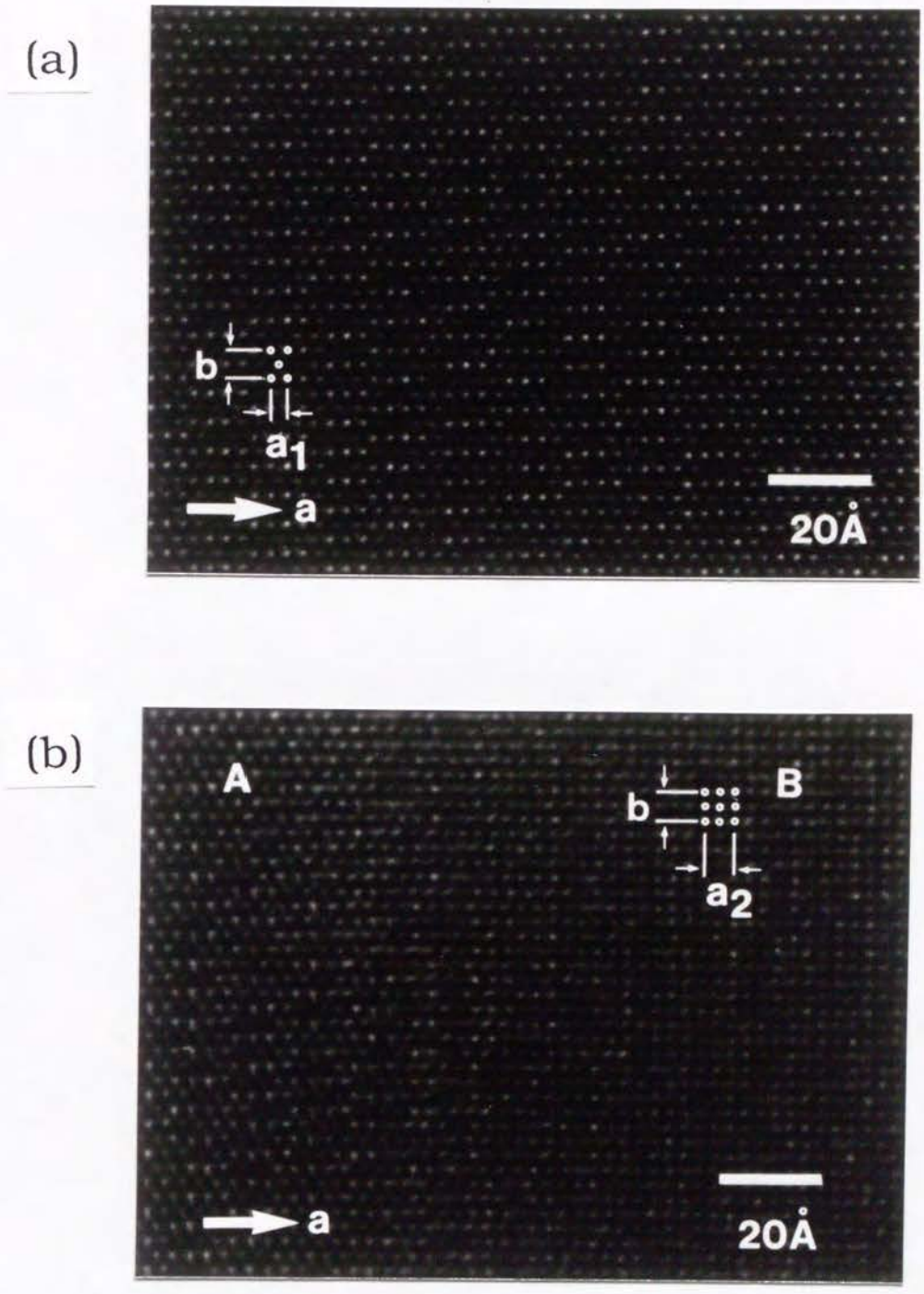

Fig. 2. Lattice images along the [001] zone axis of $(LaS)_{0.57}NbS_2$ at two different areas of the same foil. (a) The pseudo-hexagonal pattern of dots represents the NbS_2 layer. The dots show an underlying pseudo orthohexagonal lattice and their brightness varies almost periodically along the *a* axis. (b) The pseudo hexagonal pattern of dots (region A) smoothly varies into the pseudo tetragonal pattern (region B) representing the LaS layer.

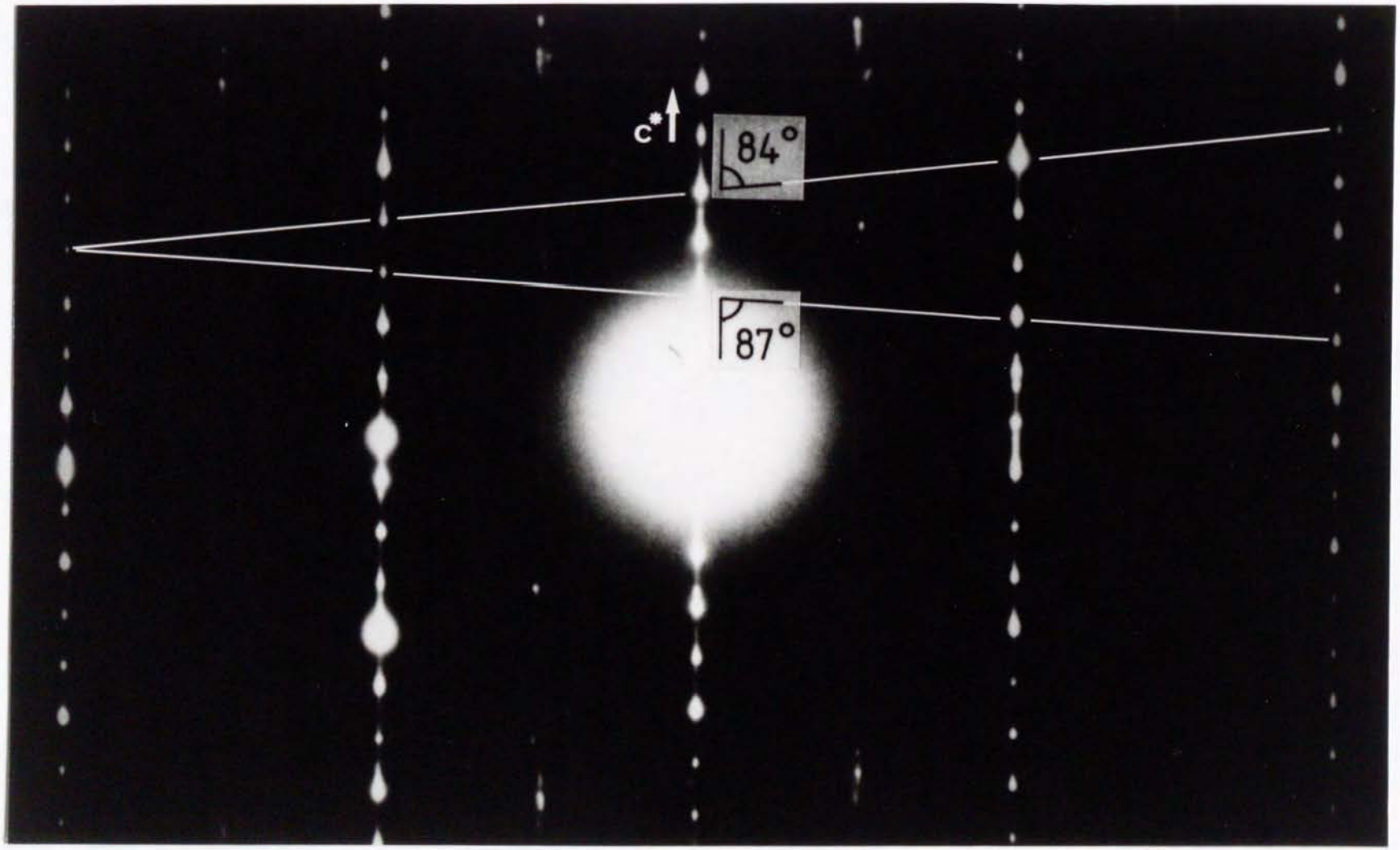

Fig. 3. Electron diffraction pattern along the [100] zone axis of $(LaS)_{0.57}NbS_2$. Two cell choices with the monoclinic angle α^* of 84° or 87° are possible.

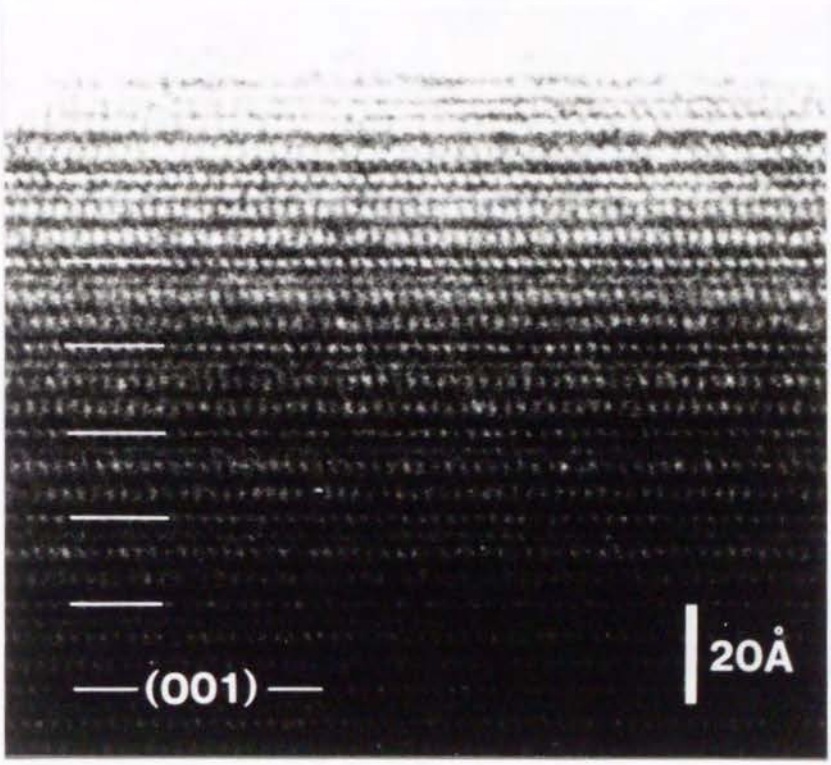

Fig. 4. Lattice image along the [100] zone axis of $(LaS)_{0.57}NbS_2$ showing (001) layer stacking with the interlayer repeat distance of ca. 17Å.

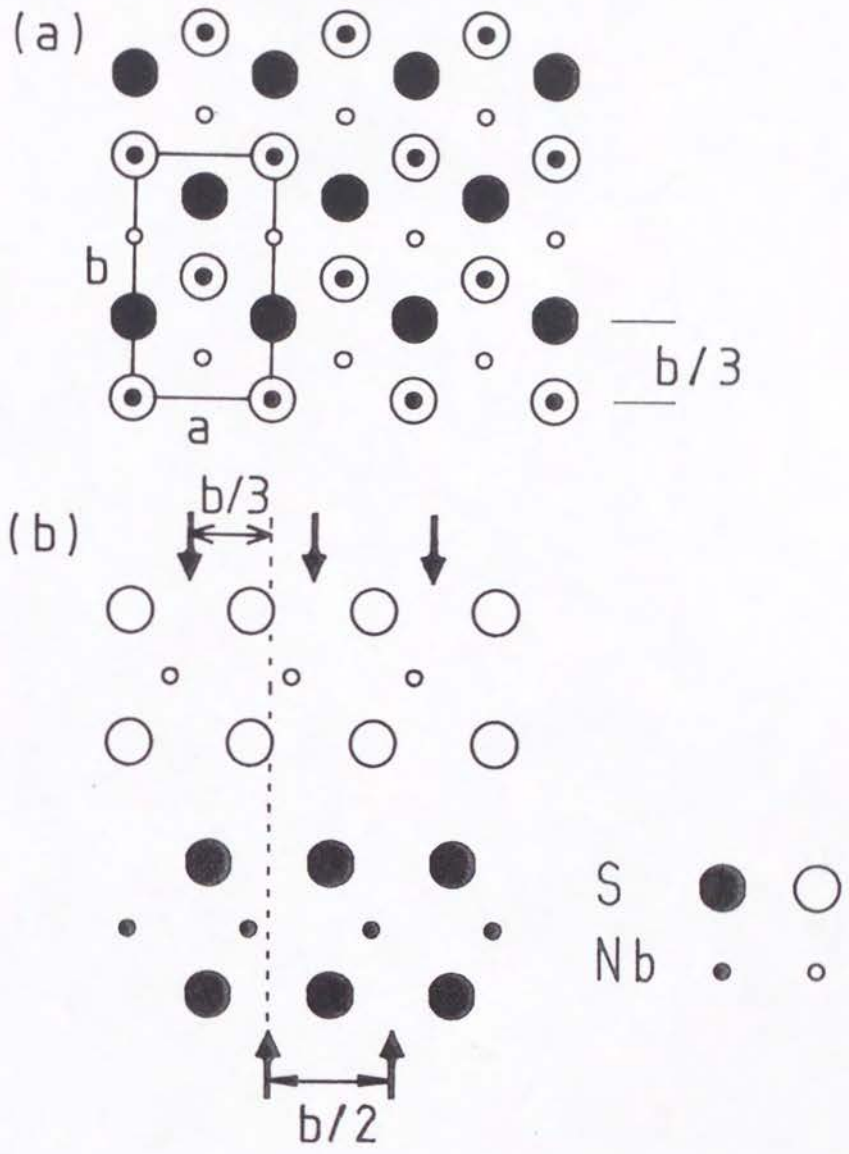

Fig. 5. Two adjacent layers in 3R-NbS_2 are viewed (a) along the *c* axis and (b) along the *a* axis of the orthohexagonal cell defined in (a). The sulfur atom rows run parallel to the *a* axis. The rows of the upper layer are displaced by *b*/3 from those of the lower layer. The grooves between the sulfur atom rows are indicated by arrows in (b).

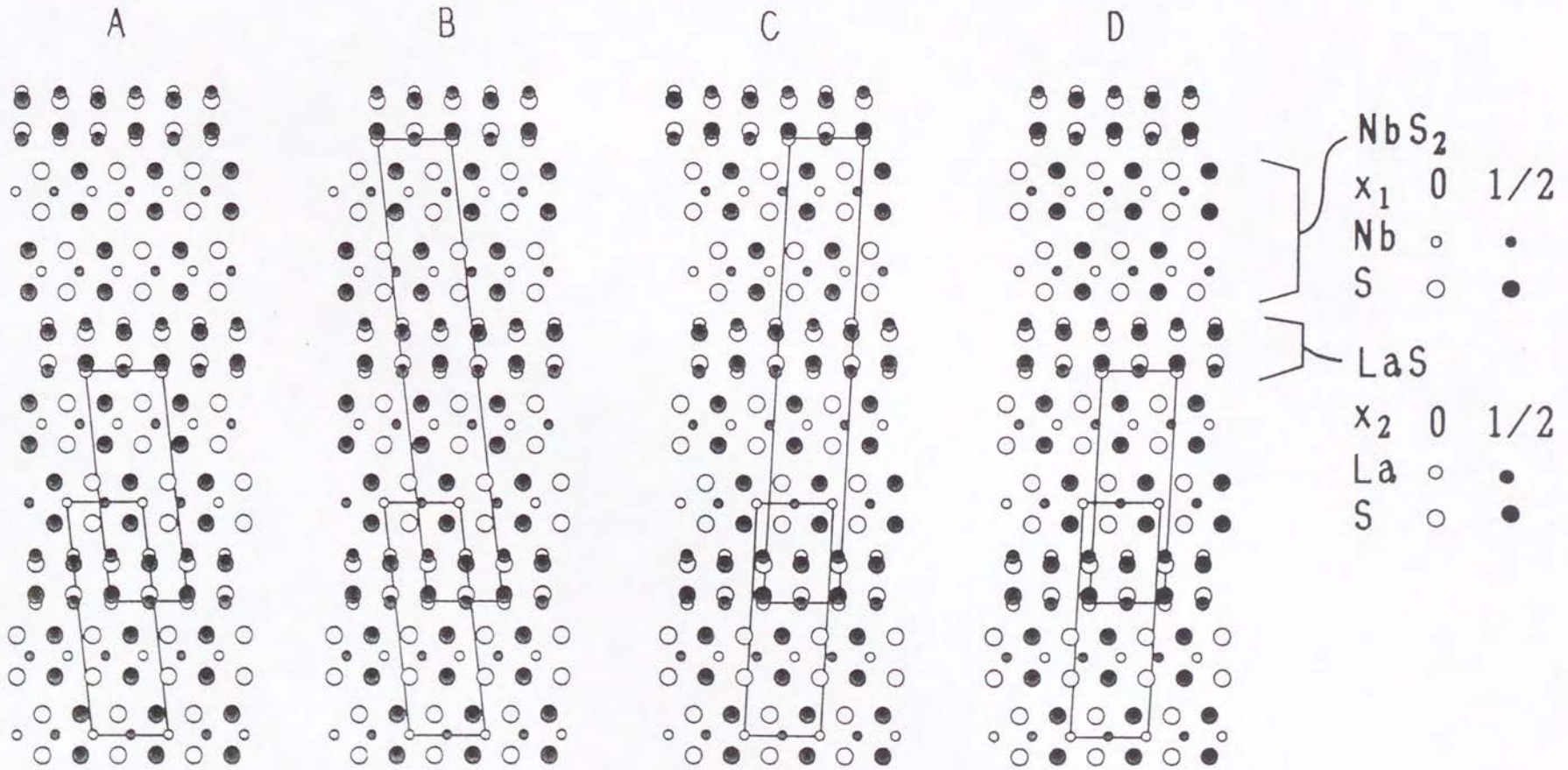

Fig. 6. Four structure models A-D for $(LaS)_{0.57}NbS_2$ viewed along the [100] zone axis. In the models B and C, the LaS sublattice is described with an F-centered monoclinic cell with a doubled *c* dimension in order to keep the *c* direction common to the NbS_2 and the LaS sublattice.

Chapter 4

Electrical Transport Properties of the Incommensurate Layer Compounds $(RES)_xNbS_2$ (RE=rare-earth metals; x=1.2, 0.6)

§1. Introduction

This chapter is mainly composed of the results of the resistivity and Seebeck coefficient measurements carried out on various compounds of $(RES)_xNbS_2$ (x=1.2, 0.6). In the course of the resistivity measurements, an anomalous decrease in the resistivity has often been observed at low temperatures for most of samples. Accordingly, we have carried out the ac magnetic susceptibility measurements on $(LaS)_{1.2}NbS_2$ in order to clarify whether the resistivity decrease is due to bulk superconductivity or not.

In addition, the dc magnetic susceptibility of $(LaS)_{1.2}NbS_2$ are also reported. From this measurement we can deduce the Pauli

paramagnetic susceptibility of the compound, which is a measure of the density of states at the Fermi level.

§2. Experimental

All the samples have been prepared as described in chapter 2.

The basal-plane resistivity ρ_{ab} was measured between 1.5 and 300 K using standard four-contact method. In the case of the single crystal #26-B of $(CeS)_{1.2}NbS_2$ taken from the batch #26, the orientation of whose a and b axes was determined by x-ray Weissenberg photographs, two successive measurements, one with a current parallel to the a axis and the other with a current parallel to the b axis, were carried out to estimate the basal-plane anisotropy in the resistivity. (The crystal #26-B has also been used in chapters 5 and 6) A similar experiment was also done on a single crystal of $(LaS)_{1.2}NbS_2$.

The c-axis resistivity ρ_c was measured for two samples of $(LaS)_{1.2}NbS_2$ using Schnabel's method. [1] The geometry of electrodes is shown in Fig. 1(a). First, a current I_{AC} is passed through the contacts A and C and the resulting voltage V_{BD} is measured between B and D. The pseudo resistance R_I is defined as $R_I=V_{BD}/I_{AC}$. Then a current I_{AB} is passed through the contacts A and B and the voltage V_{CD} is measured between C and D. The pseudo resistance R_{II} is defined as $R_{II}=V_{CD}/I_{AB}$. From the ratio $r=R_I/R_{II}$, the probe distance s, and the sample thickness w, we can decide ρ_{ab} and ρ_c simultaneously using functions calculated by Schnabel. [1] In our measurements, the current was limited to ~10 A so as to avoid

sample heating and damage. Typical voltage output across the layer, V_{BD}, in this case was only about 100 nV. In order to obtain stable readings of such a low voltage, the electrodes were made by evaporating gold.

In these resistivity measurements, the main source of error is in the estimation of the sample dimensions, especially the thickness. The typical thickness was of a few tens of μm and not very homogeneous across the sample area. Thus absolute values of the resistivity are, in general, estimated to be inaccurate by about 20% and in the worst cases of very thin and small samples the error is expected to be as large as 50%.

The Seebeck coefficient was measured between 10–300 K as follows. Two Au+0.07 at.%Fe vs. chromel thermocouples were attached to both ends of a sample [Fig. 1(b)]. With a temperature gradient, $\Delta T \leq 1$ K, applied, the voltage between the two Au+0.07 at.%Fe leads, V_{AF}, and that between the two chromel leads, V_{Ch}, were measured. The Seebeck coefficient S of the sample can be calculated by

$$S = S_{Ch} + \frac{V_{Ch}}{V_{AF} - V_{Ch}} S_{AF,Ch} \quad , \qquad (1)$$

where S_{Ch} is the Seebeck coefficient of chromel and $S_{AF,Ch}$ is a thermoelectric power of the Au+0.07 at.%Fe vs. chromel thermocouple. Unfortunately, the uncertainty in S_{Ch} and $S_{AF,Ch}$ at low temperatures and a small voltage output make it difficult a reliable measurement of a small Seebeck coefficient ($S \approx 0$) below ~50 K, which was the case with the stage-2 compounds.

The dc magnetic susceptibility of $(LaS)_{1.2}NbS_2$ was measured between 2~230 K with a Faraday balance. The sample consisted of ca. 120 mg of randomly oriented small crystals.

The ac magnetic susceptibility of $(LaS)_{1.2}NbS_2$ was measured between 1.2~4.2 K by means of a Hartshorn bridge operating at 86.9 Hz. Measuring fields of 0.1~1 Oe were applied parallel and perpendicular to the *c* axis. The sample consisted of ca. 100mg of crystals whose *c* axes were appropriately oriented to the measuring field.

§3. Results

3.1 The resistivity of the stage-1 compounds $(RES)_{1.2}NbS_2$

We start with the basal-plane anisotropy in the resistivity. In Fig. 2 are shown the *a*-axis and the *b*-axis resistivities measured for the single crystal #26-B of $(CeS)_{1.2}NbS_2$. The temperature dependence and absolute values show almost no difference between the *a*-axis and *b*-axis resistivities; ρ_a/ρ_b is 1.02 at 280 K and 0.98 at 4.2 K. An anomalous decrease in the resistivity below about 2.5 K is due to a fractional superconductivity, which will be described in detail in §3.3. In the case of a single crystal of $(LaS)_{1.2}NbS_2$, a small anisotropy is observed; ρ_a/ρ_b is 1.19 at 280 K and 1.31 at 4.2 K. This slight anisotropy, however, seems to be not intrinsic but rather due to cracks. In the crystal used for this measurement, several apparent cracks were found developing along the *b* axis and they probably made an effective cross section where a current parallel to the *a* axis could pass smaller. Thus we conclude that these two compounds

have practically no anisotropy in the basal-plane resistivity and this is probably applicable to the other compounds treated here including the stage-2 compounds.

The results of the basal-plane resistivity, ρ_{ab}, measurements are briefly summarized in Fig. 3 for the stage-1 compounds $(RES)_{1.2}NbS_2$ (RE=La,Ce,Pr,Nd,Sm,Gd,Dy,Er,Yb) [and also for the stage-2 compounds $(LaS)_{0.6}NbS_2$ and $(CeS)_{0.6}NbS_2$]. The room-temperature resistivities are several hundred $\mu\Omega$•cm. It seems that the compounds based on the heavier rare-earth metals such as Dy, Er, and Yb tend to have larger resistivities. These larger resistivities may be attributed to small changes in the carrier concentration, since the residual resistivity and a temperature-dependent part of ρ_{ab} increase in proportion. [The large resistivity of $(PrS)_{1.2}NbS_2$ is an exception and probably attributed to a large error in the estimation of the thin sample thickness (9 μm) and also to accidental poor quality of the sample as judged from considerably small residual resistivity ratio.] The residual resistivity ratio $\rho_{ab}(280\ K)/\rho_{ab,res}$ is small around 2.5 for all the stage-1 compounds due to the large residual resistivity $\rho_{ab,res}$ at 4.2 K, which indicates that the conduction carrier is strongly scattered by a random potential. This seems to have some relevance to the structural incommensurability in the present compounds and will be discussed in §4.3.

All the stage-1 compounds except $(YbS)_{1.2}NbS_2$ show very similar metallic temperature dependence of the basal-plane resistivity. To illustrate this, we have plotted normalized temperature dependences, $[\rho_{ab}(T)-\rho_{ab,res}]/[\rho_{ab}(280\ K)-\rho_{ab,res}]$, in the range of 4.2–300 K for some of the stage-1 compounds (Fig. 4).

The basal-plane resistivity shows an almost linear temperature dependence down to ~100 K and decreases as $T^3 \sim T^4$ below ~40 K. The nearly T^3 dependence of the basal-plane resistivity, not a usual T^5 law, has also been observed for pure 2H-NbS_2 and 2H-$NbSe_2$ below ~25 K. [2] In the case of $(YbS)_{1.2}NbS_2$, a slight convex curvature is seen between 100~300 K. In some samples, a very shallow minimum is observed around 10 K.

The *c*-axis resistivity ρ_c of $(LaS)_{1.2}NbS_2$ also shows a metallic behavior (Fig. 5). The anisotropy ratio ρ_c/ρ_{ab} slightly increases from 44 at 280 K to 49 at 4.2 K for one sample and from 21 at 280 K to 32 at 4.2 K for the other. In general, measurements of the resistivity perpendicular to the layer plane in layered compounds suffer from experimental problems such as interlayer shorts or internal sample cleavage. In addition to them, in the case of the present experimental setup, when a slight horizontal misalignment between the contacts B and D exists [Fig. 1(a)], the voltage V_{BD} across the layer will contain an undesirable contribution from a voltage drop along the layer. Thus the above values of the anisotropy ratio should be regarded as the lower bound. However, even then, there seems to remain a pronounced discrepancy between our result and a previous one reported by Wiegers and Haange, who have measured ρ_c of the same compound $(LaS)_{1.2}NbS_2$ by a two contact method and reported the anisotropy ratio ρ_c/ρ_{ab} of 2×10^4 at T=4.2 K. [3] We also tried two-contact measurements of ρ_c but the sample resistance was too small to be masked by the contact resistance of a few Ω.

In magnetic compounds the resistivity near the magnetic transition temperature is expected to bring certain information about

the magnetic interaction between the conduction carrier and the local magnetic moment. Unfortunately the magnetic transition temperatures in the present compounds are rather low and the fractional superconductivity often masked the intrinsic resistivities of the compounds near their magnetic transition temperatures. Thus we don't have much data on this point. The basal-plane resistivities of $(CeS)_{1.2}NbS_2$ (T_N=3.2 K, see chapter 6) and $(GdS)_{1.2}NbS_2$ (T_N=4.6 K) [4] near the respective Néel temperatures T_N show no anomaly at T_N except that the resistivity of the latter compound decreases very slightly (ca. 0.2 μΩ•cm) below T_N (Fig. 6). [For $(CeS)_{1.2}NbS_2$, see Fig. 9.] This suggests that the magnetic interaction between the conduction carrier and the local 4*f* moment is quite weak in these compounds.

3.2 The resistivity of the stage-2 compounds $(RES)_{0.6}NbS_2$

The basal-plane resistivities of the stage-2 compounds, $(LaS)_{0.6}NbS_2$ and $(CeS)_{0.6}NbS_2$, show a metallic behavior similar to the stage-1 compound (Fig. 7). However rather definite resistivity minima were observed at ca. 20 K for all the four samples examined. Defining the residual resistivity as the value at the resistivity minimum, the residual resistivity ratio is ca. 2 and smaller than a typical value of ca. 2.5 for the stage-1 compound. Below the resistivity minima, the resistivities are nearly linear to ln*T* for both the La and Ce compounds [Fig. 7(b)], which will be discussed later in §4.3 in connection with the weak localization of the conduction carrier. In $(CeS)_{0.6}NbS_2$, the basal-plane resistivity shows no anomaly at its Néel temperature (T_N=3.0 K, see chapter 6). The anomalous

resistivity drop probably due to the fractional superconductivity of the same origin as the stage-1 compounds was observed below around 2 K for two samples of $(CeS)_{0.6}NbS_2$, but the magnitude of the decrease is considerably smaller than that typically observed in the stage-1 compound.

3.3 The fractional superconductivity

Not all the samples but most of the samples of all the compounds studied here except $(LaS)_{0.6}NbS_2$ show an anomalous current-sensitive resistivity decrease at low temperatures, although this type of the anomalous behavior is omitted in Fig. 4 for simplicity. We have been interested in this phenomena and carried out an intensive resistivity measurements at low temperatures for a number of samples.

For example, we have examined the basal-plane resistivities of the five $(LaS)_{1.2}NbS_2$ samples and all of them show, more or less, the anomalous decrease. The onset temperatures of the anomaly are widely scattered between 1.5~5.5 K. The magnitude of the decrease much varies from sample to sample; the resistivities at 1.5 K are ranged from almost 0% to almost 100% of the values above the anomaly depending on a sample (and a measuring current). The resistivity curve below the onset of the anomaly is very sensitive to a small current density of 1~10 A/cm^2. The "transition" width is very broad. In some cases, the resistivity does not steadily decreases approaching to zero but levels off at a finite value (Fig. 8).

The present single-crystal resistivity measurements indicate that this resistivity decrease is anisotropic; in the case of a current

parallel to the *b* axis the onset temperature appears slightly higher and the decrease is more pronounced compared with the results with a current parallel to the *a* axis [see Fig. 9, which is an enlargement of the low temperature part of Fig. 2].

The ac magnetic susceptibility (real part) of $(LaS)_{1.2}NbS_2$ are shown in Fig. 10. A diamagnetic signal develops below ca. 2.2 K and the susceptibilities with a measuring field of 0.1 Oe parallel and perpendicular to the *c* axis reach about 30% and 10% of the perfect diamagnetism at 1.2 K, respectively. A measuring field of 1 Oe is enough to suppress the diamagnetism by about one order of magnitude. (This extremely small "critical field" makes it practically impossible to detect a diamagnetic signal by means of a usual Faraday method.) The imaginary part of the ac susceptibility gradually increases below the onset of the diamagnetism. This indicates that the shielding current flows through Josephson junctions and consequently that the Meissner volume fraction above has overestimated the true volume of the superconducting portion.

Although the diamagnetism evidences that the anomaly in the resistivity is due to superconductivity, the experimental observations mentioned above are very different from those expected for a bulk superconductor.

3.4 The Seebeck coefficient

The Seebeck coefficients of the stage-1 compounds $(LaS)_{1.2}NbS_2$ and $(CeS)_{1.2}NbS_2$ are 46 and 39 $\mu V \cdot K^{-1}$ at 280 K, respectively, and decreases with temperature as consistent with the metallic behavior of the conduction of these compounds (Fig. 11). A

small convex curvature is probably attributed to the phonon drag effect. A close value of 47 $\mu V \cdot K^{-1}$ at 280 K has been reported for $(LaS)_{1.2}NbS_2$ by Wiegers and Haange but their results show an almost linear temperature dependence different from our slightly convex curve. [3] In the case of $(CeS)_{1.2}NbS_2$, Wiegers *et al.* have reported a rather smaller value of 28 $\mu V \cdot K^{-1}$ at 280 K. [5] These disagreements are probably due to the fact that the two previous measurements were made on powder compacts.

The Seebeck coefficients of the stage-2 compounds $(LaS)_{0.6}NbS_2$ and $(CeS)_{0.6}NbS_2$ are considerably smaller and 2.8 and 5.8 $\mu V \cdot K^{-1}$, respectively (Fig. 12). The Seebeck coefficients of the two compounds decrease linearly with temperature down to ~50 K. The data below 50 K are omitted because of the experimental problem mentioned in §2.

3.5 The dc magnetic susceptibility of $(LaS)_{1.2}NbS_2$

The dc magnetic susceptibility of $(LaS)_{1.2}NbS_2$ is shown as a function of temperature in Fig. 13. The observed susceptibility is well fitted to the formula

$$\chi = \frac{C}{T-\theta} + \chi_0 \quad , \qquad (2)$$

with $C=3.29\times10^{-3}$ emu•K/mol-La, $\theta=-0.67$ K, and $\chi_0=1.6\times10^{-5}$ emu/mol-La = 1.8×10^{-5} emu/mol-Nb. The value of the Curie constant C corresponds to the fact that 0.9% of the non-magnetic La is replaced by magnetic ions with $g=2$ and $s=1/2$. This concentration of the magnetic moment is well accounted for by impurities (probably

rare-earth elements), when the nominal (commercial) purity of the starting La (99.9%) is considered. The temperature-independent term χ_0 can be regarded as the sum of the Pauli paramagnetic susceptibility of the conduction carrier and the orbital diamagnetism of ion cores.

Our results are in complete disagreement with previous results. Wiegers and Haange have reported the values of $C=0.11$ emu•K/mol-La and $\theta=-35$ K for the same compound and their susceptibility shows a strange jump at about 40 K. [3] Peña *et al.* have reported the values of C=0.03 emu•K/mol-La and $\theta=-3.5$ K. [4]

Wiegers and Haange have proposed coexistence of La^{2+} with one localized 4*f* electron and La^{3+} in $(LaS)_{1.2}NbS_2$ on the basis of their large Curie constant, which corresponds to the fact that 14% of La is divalent with one 4*f* electron in $(LaS)_{1.2}NbS_2$. [3] However, our results never support such a magnetic La^{2+} ion. Considering the large discrepancy between the Curie constants of $(LaS)_{1.2}NbS_2$ deduced by the different authors, the large magnetic moment observed by Wiegers and Haange seems to be not intrinsic.

§4. Discussion

4.1 Rigid-band model considerations

The pristine trivalent rare-earth monosulfides RES with the rock-salt structure are metallic compounds in which one electron occupies a conduction band of mainly rare-earth 5*d* character. [6] This RE 5*d* electron will be transferred to the d_{z^2} band of the host

NbS_2 layer when rare-earth sulfide layers are inserted into NbS_2 to form $(RES)_xNbS_2$.

In the case of the stage-1 compound $(RES)_{1.2}NbS_2$, some of the RE 5*d* electrons must remain on the RES layer, since there are more than one RE 5*d* electron per Nb. Hence the intercalate RES layer may sustain conduction carriers. In other words, the intercalate band of mainly RE 5*d* character is expected to exist at the Fermi level besides the d_z^2 band of the host layer from a naive expansion of the rigid-band model, i.e., if we impose the rigid-band model not only on the host band-structure but also on the intercalate one. However, Wiegers *et al.* have observed the almost temperature-independent Hall coefficient, which is characteristic of a single-carrier system, for the stage-1 compound $(CeS)_{1.2}NbS_2$ and the observed Hall coefficient is positive, which is consistent with the more than half-filled d_z2 band. [5] Hence they have attributed this carrier to holes in the d_z^2 band and have estimated its concentration at 0.04 hole/Nb (an average of two single-crystal measurements), employing a single-carrier model. [5] This hole concentration corresponds to a large charge transfer rate of 0.83 electron per Ce. (Wiegers *et al.* have remarked that the Hall coefficients determined for the two single crystals differ by a factor of 2.3 and have attributed it to an error in the estimation of the thickness of the very thin crystals. [5] Accordingly the carrier concentration quoted above contains a considerable error of up to ~50%, while this error brings only relatively small uncertainty in the charge transfer rate.) Although the assumption of the single-carrier system is not fully self-evident, we will show our results support this assumption.

In the case of the stage-2 compound, the charge transfer rate per Nb will be almost halved due to the doubled NbS_2 layer. Accordingly, even though the complete charge transfer occurs, i.e., one electron per RE is transferred into the d_{z^2} band, the d_{z^2} band still contains 0.4 hole/Nb, which is one order of magnitude larger than the hole concentration in the stage-1 compound. Thus a pronounced change in the carrier concentration is expected from the rigid-band model for the host band-structure.

On the basis of these considerations with the rigid-band model, we discuss implications of our results below.

Assuming Matthiessen's rule, the electrical resistivity ρ in magnetic compounds can be expressed as

$$\rho = \rho_{res} + \rho_{ph} + \rho_{mag} , \qquad (3)$$

where ρ_{res} is the temperature-independent residual resistivity due to lattice defects and impurities, ρ_{ph} is the resistivity arising from the scattering of the conduction carrier by phonons, and ρ_{mag} is due to the scattering by local magnetic moments. The magnetic resistivity ρ_{mag} is expected to depend on the particular rare-earth element of $(RES)_xNbS_2$ and to be proportional to the de Gennes factor $(g_J-1)^2J(J+1)$ at high temperatures if we assume the exchange coupling between the conduction carrier and the local $4f$ moment is the same among compounds based on different rare-earth metals. [7] In addition, the magnetic resistivity, generally, shows an anomaly such as a rapid decrease or a cusp at the magnetic transition temperature. However the resistivities of $(RES)_xNbS_2$ show little difference in the temperature dependence among the same stage compounds and no correlation between the room-temperature values

and the de Gennes factor can be seen. The resistivities of $(CeS)_{1.2}NbS_2$, $(GdS)_{1.2}NbS_2$, and $(CeS)_{0.6}NbS_2$ show almost no anomaly near the respective magnetic transition temperatures T_N. These facts indicate that ρ_{mag} in these compounds is very small, which is quite unlikely if the conduction carriers are predominantly the RE 5*d* electrons. Hence the metallic conduction of $(RES)_xNbS_2$ is dominated by the d_{z^2} band of NbS_2, which can be another justification for the single-carrier assumption, and the exchange coupling between this carrier and the local 4*f* moment is rather small.

The anisotropy ratio ρ_c/ρ_{ab} measured for the stage-1 compound $(LaS)_{1.2}NbS_2$ is 21~44 (T=280 K), which indicates that the electronic structure of the compound is a quasi two-dimensional one reflecting the quasi two-dimensional structure. However this anisotropy ratio is 40~90 times smaller than that for pure 2H-NbS_2 (ρ_c/ρ_{ab}=1900 at 300 K). [8] In general, intercalation replaces the weak interlayer interaction of van der Waals type in pure materials with interaction of somewhat bonding character between the intercalate and the host layer in intercalation compounds. For example, Pfalzgraf *et al.* have reported a still smaller anisotropy of ρ_c/ρ_{ab}=4 for copper intercalated NbS_2, $Cu_{1/2}NbS_2$, and have attributed it to strong interlayer coupling via the inserted copper atoms. [9] Hence the smaller anisotropy ratio observed for $(LaS)_{1.2}NbS_2$ is not unexpected.

The Seebeck coefficient decreases by about one order of magnitude when one goes from the stage-1 compound to the stage-2 compound. The Seebeck coefficient S of metals consists of two separate contributions, namely, the diffusion thermopower of the

conduction electron S_d and the phonon drag effect S_{ph}. [10] (Here we neglect the magnon drag term, which would be small in the present compounds as the magnetic resistivity.) The diffusion thermopower S_d is inversely proportional to the Fermi energy ε_F and varies linearly with temperature as

$$S_d = \frac{\pi^2 k_B{}^2 T}{3e\,\varepsilon_F}(p+d)\ , \qquad (4)$$

where d equals 1 or 3/2 for two- or three-dimensional metals, respectively. [11] The scattering parameter p characterizes the energy dependence of the relaxation time τ of the conduction electron as $\tau \propto \varepsilon^p$; p=−1/2 for ionized impurity scattering and 3/2 for acoustic phonon scattering, for example. The phonon drag thermopower S_{ph} increases as T^3 at low temperatures, shows a maximum around $0.1\theta_D$~$0.2\theta_D$, where θ_D is the Debye temperature, and then decreases as T^{-1} at high temperatures. [10]

The overall shapes of the Seebeck coefficient curves of the stage-1 and stage-2 compounds are fairly linear to temperature, especially at high temperatures, indicating the diffusion thermopower S_d is the dominant term. Hence the drastic reduction of the Seebeck coefficient in the stage-2 compound should primarily be ascribed to a considerable increase in the Fermi energy. Using eq. (4) with d=1, p=1/2, and the values at 280 K as the diffusion thermopower, we obtain

ε_F = 0.23 and 0.28 eV for $(LaS)_{1.2}NbS_2$ and $(CeS)_{1.2}NbS_2$, respectively, and

ε_F = 3.7 and 1.8 eV for $(LaS)_{0.6}NbS_2$ and $(CeS)_{0.6}NbS_2$, respectively. However, it is to be noted that these values are rough estimates and must be viewed in a qualitative manner because of the crude approximations explicitly and implicitly made.

The Fermi energy of the stage-1 compounds is really small as is consistent with the small carrier concentration that is deduced from the Hall coefficient measurements with the single-carrier assumption. It is quite likely that the two stage-1 compounds have practically the same Fermi energy, since the charge transfer ratio is probably almost the same for the two compounds. The about one order of magnitude larger Fermi energies calculated for the stage-2 compounds indicate a substantial increase in the carrier concentration, which is just expected from the rigid-band model for the host band-structure as discussed above. However the values for $(LaS)_{0.6}NbS_2$ and $(CeS)_{0.6}NbS_2$ differ by a factor of two and, even though we take into account the approximate nature of the estimations, the Fermi energy of the former compound seems to be too large for the narrow d_{z^2} band. This might imply that the Seebeck coefficient of $(LaS)_{0.6}NbS_2$ contains some negative contribution from the electron-like Fermi surface. Although several band-structure calculations of NbS_2 predict only the hole-like Fermi surface [12] and the Hall coefficient of NbS_2 is positive, [2] the Seebeck coefficient of NbS_2 is negative, [13] indicating some electron-like Fermi surface coexists with the major hole-like one. In intercalation compounds, such an electron-like Fermi surface might survive when the charge transfer is not very large as has been pointed out by Bouwmeester *et*

al. in connection with negative Seebeck coefficients of Ag_xNbS_2 (x=0.25,0.6). [14] This might be the case with $(LaS)_{0.6}NbS_2$.

The Pauli paramagnetic susceptibility χ_p, which is proportional to the density of states at the Fermi energy, of $(LaS)_{1.2}NbS_2$ can be estimated by subtracting the diamagnetic susceptibility of the ion core χ_d from the observed temperature-independent susceptibility χ_0. Using the values of $\chi_d(La^{3+})=-20\times10^{-6}$ emu/mol, [15] $\chi_d(Nb^{5+})=-9\times10^{-6}$ emu/mol, [15] and $\chi_d(S^{2-})=-21\times10^{-6}$ emu/mol, [16] we obtain $\chi_p=1.2\times10^{-4}$ emu/mol-Nb. Pure 2H-NbS_2 shows almost temperature-independent magnetic susceptibility of about 2.0×10^{-4} emu/mol. [17] Applying the same correction for the diamagnetism, the Pauli paramagnetic susceptibility of 2H-NbS_2 is estimated at 2.5×10^{-4} emu/mol. Hence the density of states at the Fermi energy of $(LaS)_{0.6}NbS_2$ is reduced from that of the host NbS_2 by a factor of two. This is qualitatively consistent with the increased occupation of the d_{z^2} band by the charge transfer, since the density of states of 2H-NbS_2 has a maximum at slightly lower energy than its Fermi energy and decreases toward both ends of the d_{z^2} band. [12] Such a comparison of the Pauli paramagnetic susceptibility would be more meaningful if we could utilize that of the stage-2 compound $(LaS)_{0.6}NbS_2$. However, unfortunately, it was impossible to measure the magnetic susceptibility of $(LaS)_{0.6}NbS_2$ since only a quite small amount of the specimens were available.

Thus we can well interpret the transport and magnetic results by applying the rigid-band model to the host band-structure and incorporating a large charge transfer from the intercalate RES layer to the host d_{z^2} band. There has appeared no need to take account of

the intercalate band of mainly RE 5*d* character, although we have noted that it can exist at the Fermi level in the stage-1 compound $(RES)_{1.2}NbS_2$. As will be reported in chapter 6, we have found a large crystal-field splitting of the $^2F_{5/2}$ state of Ce^{3+} in the stage-1 compound $(CeS)_{1.2}NbS_2$ from the analysis of the magnetic susceptibility. The found overall splitting of more than 500 K is even larger than that in semiconducting Ce_2S_3 (385 K), [18] which indicates that the crystal field around the Ce^{3+} ions in $(CeS)_{1.2}NbS_2$ is hardly screened by the free carriers. Combining this with the present results, we infer that the intercalate RE 5*d* band has a vanishing or only negligibly small density of states at the Fermi level.

4.2 The fractional superconductivity

The anomalous resistivity decrease at low temperatures often observed in $(RES)_xNbS_2$ has been a controversial problem. A similar anomaly has been reported for $(LaS)_{1.2}NbS_2$ by Meerschaut *et al.* [19] and for $(RES)_{1.2}NbS_2$ (RE=La, Ce, Sm, Y) by Peña *et al.* [4] The authors of both the papers have attributed it to a superconducting transition. On the contrary, Reefman *et al.* have stated that the compounds $(RES)_{1.2}NbS_2$ (RE=La, Sm) do not become superconducting down to 0.07 K on the basis of the ac magnetic susceptibility data. [20] Suzuki *et al.* have observed the same type of a resistivity drop in related compounds $(RES)_xTaS_2$ (RE=La, Ce; $x \approx 1.2$, 0.6) and regarded it as a fractional superconductivity occurring at interfaces of the intercalate domains. [21]

The present ac susceptibility data show the resistivity anomaly is due to superconductivity. However the experimental

characteristics seem to imply that the superconductivity is not a bulk but a fractional one, i.e., only some portions of the samples become superconducting. The portion that is responsible for this fractional superconductivity cannot be a macroscopic quantity of superconducting impurities, since our samples are verified to be single-phased by the (00*l*) x-ray diffractgrams. Especially, the crystal #26-B of $(CeS)_{1.2}NbS_2$, which does exhibit the resistivity decrease as can be seen Fig. 9, is a single crystal as far as the x-ray Weissenberg photographs concern. Very similar fractional superconductivity has often been observed for transition-metal trichalcogenides such as $NbSe_3$, [22] $TaSe_3$, [22] and $ZrSe_3$. [23] In the case of $NbSe_3$, careful experiments by Kawabata and Ido have proved that the fractional superconductivity occurs only near crystal boundaries between single crystals. [24] A similar explanation seems to be applicable to the present case.

The present single-crystal resistivity measurements show that the resistivity decrease is more pronounced for $I//b$ than for $I//a$, which indicates that the superconducting portions are aligned parallel to the *b* axis. If we assume that crystals are sub-divided into domains by micro-boundaries running parallel to the *b* axis, that the intercalate RES layer is absent near such micro-boundaries, and that un-intercalated NbS_2 thus formed at the micro-boundaries are responsible for this fractional superconductivity, the observed anisotropy is well explained. Although the superconducting transition temperature of pristine 2H-NbS_2 is 6.23 K, [17] the influence of stress, inhomogeneity, off-stoichiometry, etc. on NbS_2 at

the micro-boundaries could account for the wide scattering of the onset temperatures and the broad transition widths.

The existence of such micro-boundaries can be rationalized by structural considerations on the incommensurability along the *a* axis between the intercalate RES and the host NbS_2 layer and on the pinning of the former to the latter. In real crystals, the intercalate layer is never ideally incommensurate with the host layer throughout a crystal, but is pinned at several points due to impurities, defects, etc. of the host layer. When two intercalate domains pinned at different positions meet, there is no *a priori* reason that they smoothly connect along the incommensurate *a* axis. Thus micro-boundaries of mismatching region are formed along the *b* axis and the intercalate RES may `be vacant there. In this connection, it is worth while noting the following experimental observations: (i) When crystals are cleaved, cleaved thin foils are found to be elongated along the *b* axis. (ii) Crystals are easy to bend so as to enclose the *b* axis and also to cut along the *b* axis. These facts seem to suggest that crystals are sub-divided into domains elongated along the *b* axis.

4.3 The large residual resistivity and the carrier localization

In general, the intercalation compound is not expected to have a very high residual resistivity ratio, which is an indication of the structural perfection of crystals, since the structure of the intercalate layer is not very regular. The disorder in the intercalate layer will act on the conduction electron associated with the host layer as a random potential scattering it. The magnitude of the random

potential experienced by the conduction electron will depend on the nature and the strength of the interlayer interaction between the host and the intercalate layer. Thus various values of the residual resistivity ratio have been found for intercalation compounds: For example, the residual resistivity ratio has been reported to be 4 for $Ag_{2/3}TaS_2$, [25] 8 for $Ag_{1/3}TaS_2$, [25] 14 for $Cu_{1/2}NbS_2$, [9] and 20–40 for $K_x(H_2O)_y$ TaS_2 ($0.27<x<0.4$). [26]

In the case of the 3*d* transition-metal intercalated TX_2, M_xTX_2, the intercalate layer forms $\sqrt{3} \times \sqrt{3}$ and 2×2 superlattices for $x=1/3$ and $1/4$, respectively. [27] The residual resistivity, in this case, is known to be a sensitive index of the superlattice ordering and hence the stoichiometry of the compound; the stoichiometric compound with a well-ordered intercalate superlattice has a low residual resistivity of a few tens of μΩcm, while the off-stoichiometric compound exhibits a large residual resistivity of several hundred μΩcm. [28,29]

The present compounds show large residual resistivities of ca. 100~300 μΩ•cm and hence the residual resistivity ratios are small, typically 2.5 for the stage-1 compounds and 2.0 for the stage-2 compounds. Comparing these values with the above cited ones, one might conclude that the present compounds are much disordered in their structures. However, this seems rather curious, since the intercalate RES layer of the present compounds forms its own regular lattice.

It has been known that under the presence of an incommensurate charge-density-wave (CDW) a small amount of impurities or defects causes a very large residual resistivity. [30,31]

This has been attributed to a local distortion of the CDW around the impurities or defects: [30,31] Not only the random potential arising from each impurity or defect but also this distortion will contribute the scattering of the conduction electron. Thus the effect of impurities and defects are effectively enhanced with the incommensurate CDW present.

In the present compounds, the host NbS_2 layer and hence its electronic structure are perturbed by an incommensurate potential arising from the mutual modulation between the host NbS_2 and the intercalate RES layer. It is helpful to consider this incommensurate potential by analogy with the incommensurate CDW. This modulation potential has a well-defined periodicity of the intercalate layer, although it is incommensurable with that of the host NbS_2 layer, and can give rise to only a matrix element connecting two states separated by the wave vector corresponding to this periodicity. This incommensurate potential, probably, cannot be an origin of the residual resistivity as far as its phase is coherent throughout a crystal. However we have to take into account the fact that the intercalate layer is randomly pinned at impurities or defects of the NbS_2 layer; the impurities and defects in the host NbS_2 layer will attract or repel the RE ions near them, leading to a distortion of the intercalate structure. Thus the modulation potential is disturbed and Fourier components other than that with the basic periodicity of the intercalate layer emerge. They, in turn, scatter the conduction electron, contributing the residual resistivity.

Summarizing this, the effect of the random potential arising from impurities or defects of the host NbS_2 layer on the conduction

electron is amplified through the local adjustment of the intercalate structure. This probably account for the large residual resistivity and the quite small residual resistivity ratio in the present compounds. It is interesting to note that fairly large residual resistivity ratios exceeding 10 have been reported for some other incommensurate layer compounds such as $(SnS)_{1.2}NbS_2$ [32] or $(PbS)_{1.2}TaS_2$, [33] which may be attributed to the difference in the strength of the interlayer interaction between the present compounds and them.

In the case of the stage-1 compounds, some of the samples show a very slight resistivity minimum at around 10 K. On the contrary, the resistivities of the stage-2 compounds, $(LaS)_{0.6}NbS_2$ and $(CeS)_{0.6}NbS_2$, show rather pronounced minima at around 20 K and exhibit clear logarithmic temperature dependences below these minima. The impurity Kondo effect and the weak localization of the two-dimensional carrier under a random potential both may account for such logarithmic temperature dependences. The latter possibility is more likely when we take account of the quasi two-dimensional nature of the present compounds and recall the fact that the stage-2 compound has a smaller residual resistivity ratio of ca. 2.0 and hence that the conduction carrier is probably more influenced by the random potential.

Taking into account the weak localization and the electron-electron interaction in a random potential, the resistance $R(T)$ of the two-dimensional metal at low temperatures can be expressed as [34]

$$\frac{R(T)-R(T_m)}{R(T_m)} = -AR_{\square}(T_m)\frac{e^2}{2\hbar\pi^2}\ln\left(\frac{T}{T_m}\right) , \qquad (5)$$

where T_m is the temperature where the resistance minimum is observed and A is a parameter of order of unity characterizing the system. Assuming that the carrier in $(RES)_{0.6}NbS_2$ is confined to the host NbS_2 layer, we define the sheet resistance per a doubled NbS_2 layer, $R_\square$,as the sample resistivity divided by the interlayer repeat distance I_c. Fitting the eq. (5) to the experimental low temperature resistances, we obtain the values of A of 1.1 and 0.6 for two samples of $(LaS)_{0.6}NbS_2$ and of 1.5 and 0.5 for two samples of $(CeS)_{0.6}NbS_2$. The scattering in these values are probably due to errors in estimations of the small sample dimensions. Indeed, if we employ the quantity $AR_\square(T_m)e^2/2\hbar\pi^2$ that is free of the error in the sample dimensions, a universal feature of the phenomena can be seen; its value is well converged between 0.010~0.011 except one sample which has a smaller value of 0.007.

§5. Summary and Conclusions

The basal-plane resistivities of the stage-1 compounds $(RES)_{1.2}NbS_2$ (RE=La, Ce, Pr, Nd, Sm, Gd, Dy, Er, Yb) and the stage-2 compounds, $(LaS)_{0.6}NbS_2$ and $(CeS)_{0.6}NbS_2$, and the Seebeck coefficients of some of them have been measured. The c-axis resistivity and the dc and ac magnetic susceptibilities have also been measured for $(LaS)_{1.2}NbS_2$. Some of our results show disagreements with the previous ones.

The basal-plane resistivities show a very similar metallic temperature dependence among the same-stage compounds and they exhibit almost no anomaly at the magnetic transition temperatures.

The Seebeck coefficients of the stage-2 compounds are about one order of magnitude smaller than those of the stage-1 compounds, indicating the Fermi energy and hence the carrier concentration in the former compounds are considerably larger. The Pauli paramagnetic susceptibility of $(LaS)_{1.2}NbS_2$ is about half of that of 2H-NbS_2. These results are well interpreted within the rigid-band model by incorporating the large charge transfer from the intercalate RES layer to the host d_z^2 band. There appears to be no need to take into account the intercalate RE 5*d* band possibly existing at the Fermi level.

Most of the samples show an anomalous resistivity decrease at low temperatures, which is ascribed to not bulk but fractional superconductivity. We infer that its origin is un-intercalated NbS_2 at microboundaries of mismatching regions elongating along the *b* axis between intercalate domains.

The logarithmic temperature dependence of the basal-plane resistivity is found for the stage-2 compounds below ca. 20 K. We attribute it to the weak localization arising from the two-dimensional character of the carriers confined in the host NbS_2 layer.

References

1) P. Schnabel: Philips Res. Rep. **19** (1964) 43.

2) M. Naito and S. Tanaka: J. Phys. Soc. Jpn. **51** (1982) 219.

3) G. A. Wiegers and R. J. Haange: J. Phys.: Condens. Matter **2** (1990) 455.

4) O. Peña, P.Rabu, and A. Meerschaut: J. Phys.: Condens. Matter **3** (1991) 9929.

5) G. A. Wiegers, A. Meetsma, R. J. Haange, and J. L. de Boer: J. Solid State Chem. **89** (1990) 328.

6) P. Wachter: Phys. Rep. **44** (1978) 159.

7) S. Legvold: *Magnetic Properties of Rare Earth Metals*, ed. R. J. Elliott (Plenum, London, 1972), p.335.

8) B. W. Pfalzgraf and H Spreckels: J. Phys. C **27** (1987) 4359.

9) B. W. Pfalzgraf, H. Spreckels, W. Paulus, and R. Schöllhorn: J. Phys. F: **17** (1987) 857.

10) R. D. Barnard: *Thermoelectricity in Metals and Alloys*, (Taylor & Francis, London, 1972).

11) A. Amara, Y. Frongillo, M. J. Aubin, S. Jandl, J. M. Lopez-Castillo, and J. -P. Jay-Gerin: Phys. Rev. B **36** (1987) 6415.

12) E. Doni and R. Girlanda: *Electronic Structure and Electronic Transitions in Layered Materials*, ed. V. Grasso (D. Reidel, Dordrecht, 1986), p.1.

13) M. H. van Maaren and H. B. Harland: Phys. Lett. A **29** (1969) 571.

14) H. J. M. Bouwmeester, A. van der Lee, S van Smaalen, and G. A. Wiegers: Phys. Rev. B **43** (1991) 9431.

15) *Kagaku Binran Kisohen* (Chemistry Handbook), ed. The Chemical Society of Japan, (Maruzen, Tokyo, 1984) 3rd. ed., vol. II, p.508 [in Japanese].

16) F. J. Di Salvo, G. W. Hull Jr., L. H. Schwartz, J. M. Voorhoeve, and J. V. Waszczak: J. Chem. Phys. **59** (1973) 1922.

17) W. G. Fisher and M. J. Sienko: Inorg. Chem. **19** (1980) 39.

18) I. Mörke, E. Kaldis and P. Wachter: Phys. Rev. B **33** (1986) 3392.

19) A. Meerschaut, P. Rabu, J.Rouxel, P. Monceau, and A. Smontara: Mater. Res. Bull. **25** (1990) 855.

20) D. Reefman, J. Baak, H. B. Brom, and G. A. Wiegers: Solid State Commun. **75** (1990) 47.

21) K. Suzuki, N. Kojima, T. Ban, and I. Tsujikawa: J. Phys. Soc. Jpn. **59** (1990) 266.

22) R. A. Buhrman, C. M. Bastuscheck, J. C. Scott, and J. D. Kulick: *Proc. Conf. Inhomogeneous Superconductors, Berkeley Spring, 1979*, A. I. P. Conf. Proc., Vol. 58 (1980), p. 207.

23) T. Sambongi, K. Yamaya, and K. Nomura: Jpn. J. Appl. Phys. Series 1, Superconducting Materials (1988), p.146.

24) K. Kawabata and M. Ido: Solid State Commun. **44** (1982) 1539.

25) G. A. Scholz and R. F. Frindt: Phys. Status Solidi. A **79** (1983) 483.

26) W. Biberacher, W. Joss, J. M. van Ruitenbeek, and A. Lerf: Phys. Rev. B **40** (1989) 115.

27) R. H. Friend and A. D. Yoffe: Adv. Phys. **36** (1987) 1.

28) A. Le Blanc-Soreau, J. Rouxel, M. F. Gardette, and O. Gorochov: Mater. Res. Bull. **11** (1976) 1061.

29) S. S. P. Parkin and R. H. Friend: Philos. Mag. B **41** (1980) 95.

30) W. W. Fuller, P. M. Chaikin, N. P. Ong: Solid State Commun. **39** (1981) 547.

31) F. J. Di Salvo, J. A. Wilson, and J. V. Waszczak: Phys. Rev. Lett. **36** (1976) 885.

32) G. A. Wiegers, A. Meetsma, R. J. Haange, and J. L. de Boer: Mater. Res. Bull. **23** (1988) 1551.

33) J. Wulff, A. Meetsma, S. van Smaalen, R. J. Haange, J. L. de Boer, and G. A. Wiegers: J. Solid State Chem. **84** (1990) 118.

34) P. A. Lee and T. V. Ramakrishnan: Rev. Mod. Phys. **57** (1985) 287.

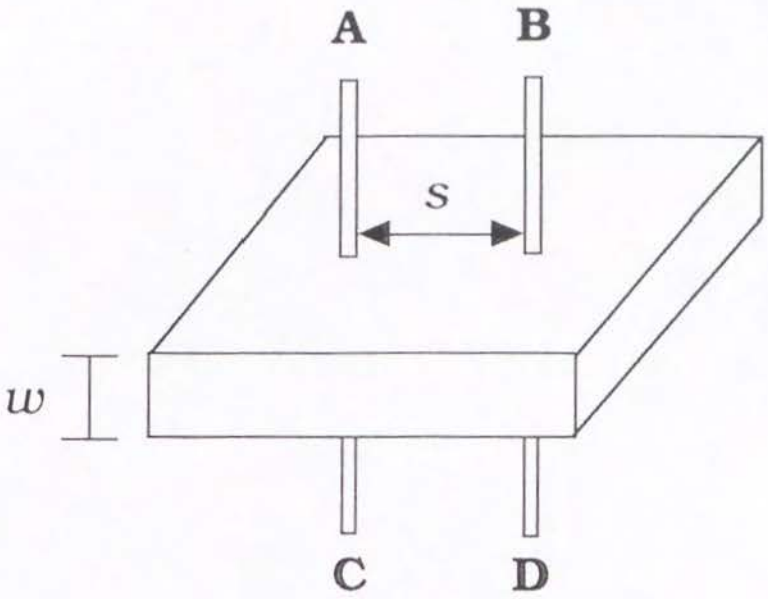

(a)

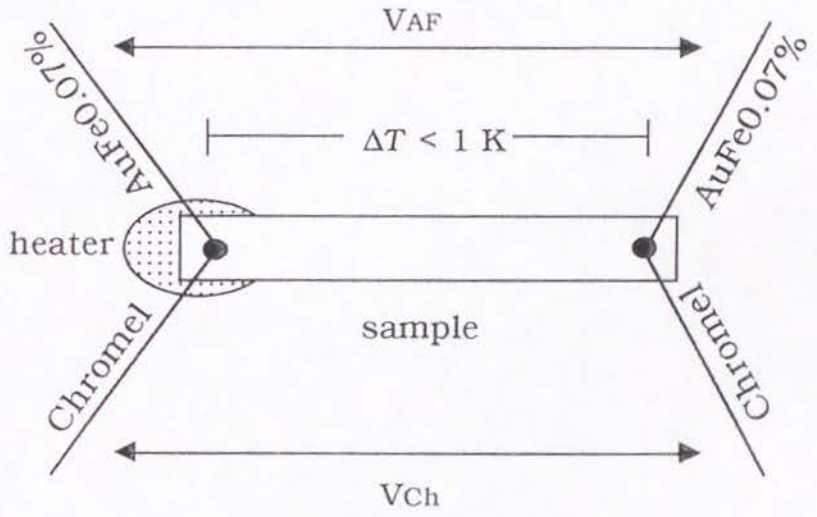

(b)

Fig. 1. (a) The geometry of electrodes for Scnabel's method; w is the sample thickness and s is the distance between the electrodes. (b) The thermocouple arrangement for the Seebeck coefficient measurements. Two Au+0.07 at.%Fe vs. chromel thermocouples are attached to both ends of a sample. With a temperature gradient, $\Delta T \leq 1$ K, applied, the voltage V_{AF} between the two Au+0.07 at.%Fe leads and the voltage V_{Ch} between the two chromel leads are measured.

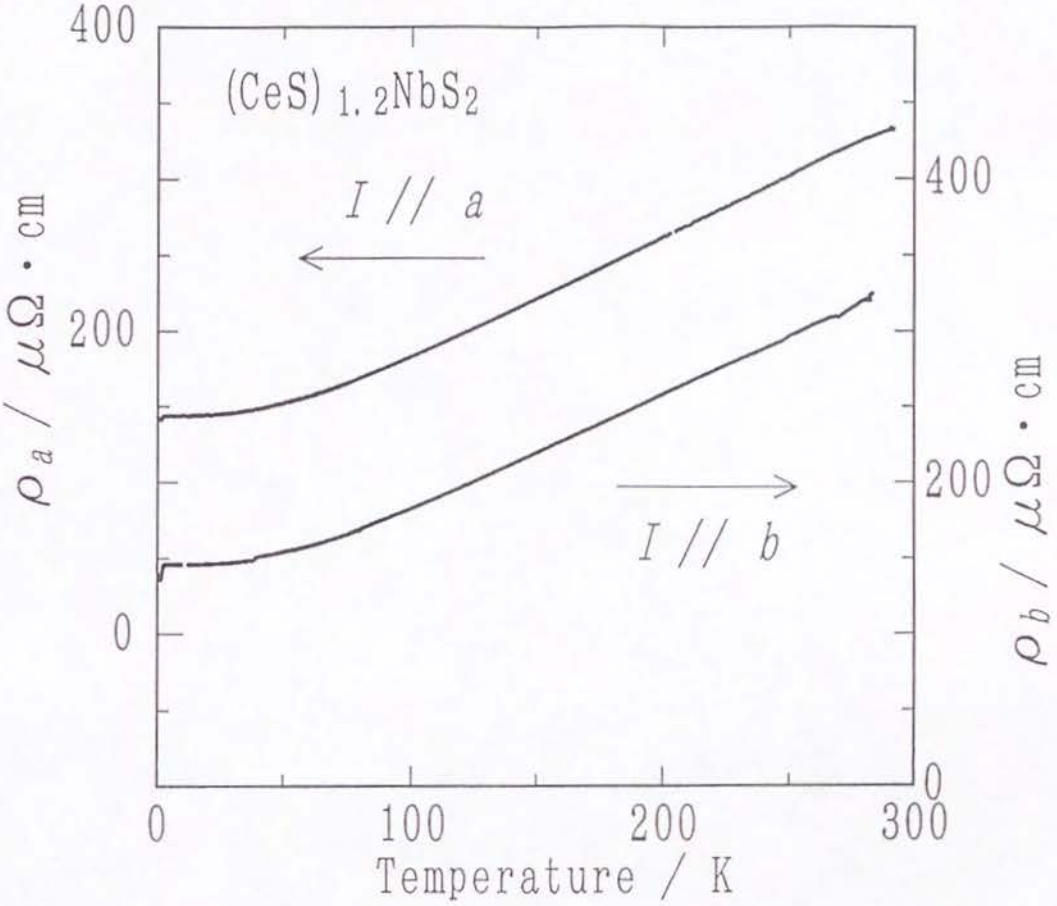

Fig. 2. The *a*-axis and *b*-axis resistivities measured for the single crystal #26-B of $(CeS)_{1.2}NbS_2$.

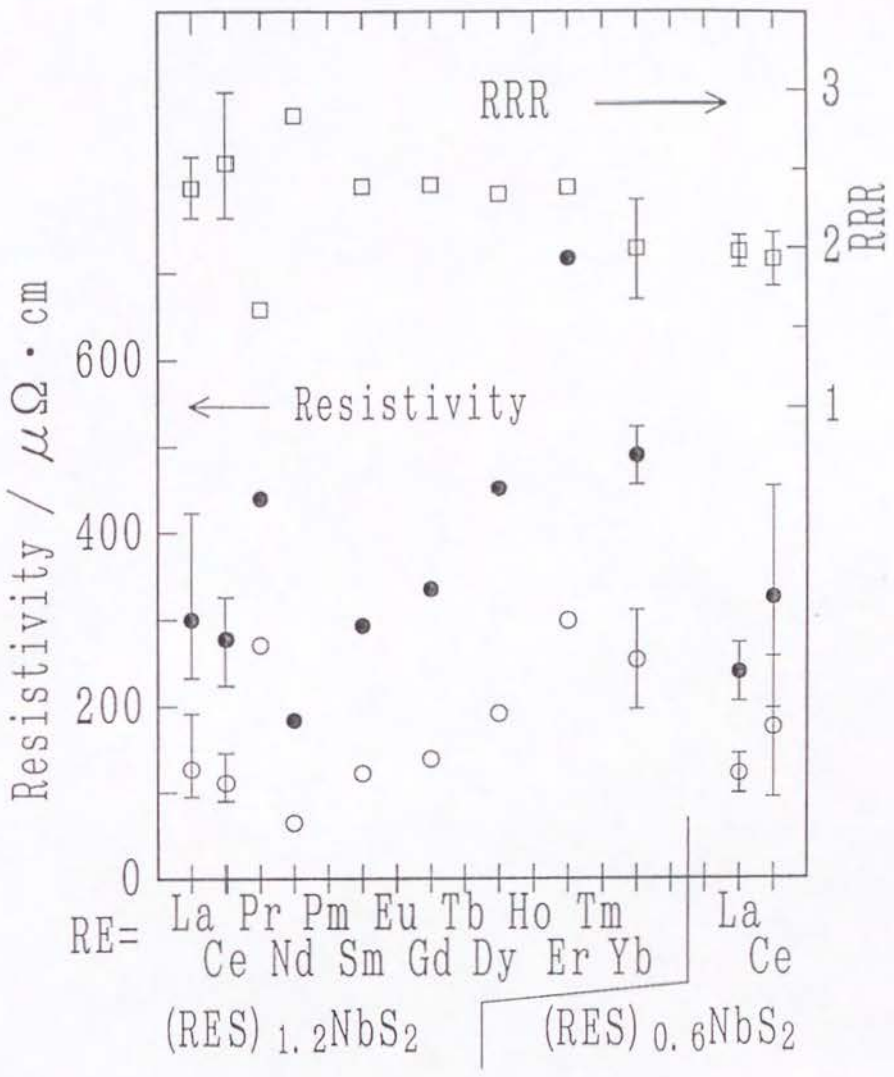

Fig. 3. The basal-plane resistivities at 4.2 K (open circles) and at 280 K (solid circles), and the residual resistivity ratios RRR=ρ_{ab}(280 K)/ρ_{ab}(4.2 K) (squares) of the stage-1 compounds $(RES)_{1.2}NbS_2$ and the stage-2 compounds $(RES)_{0.6}NbS_2$.

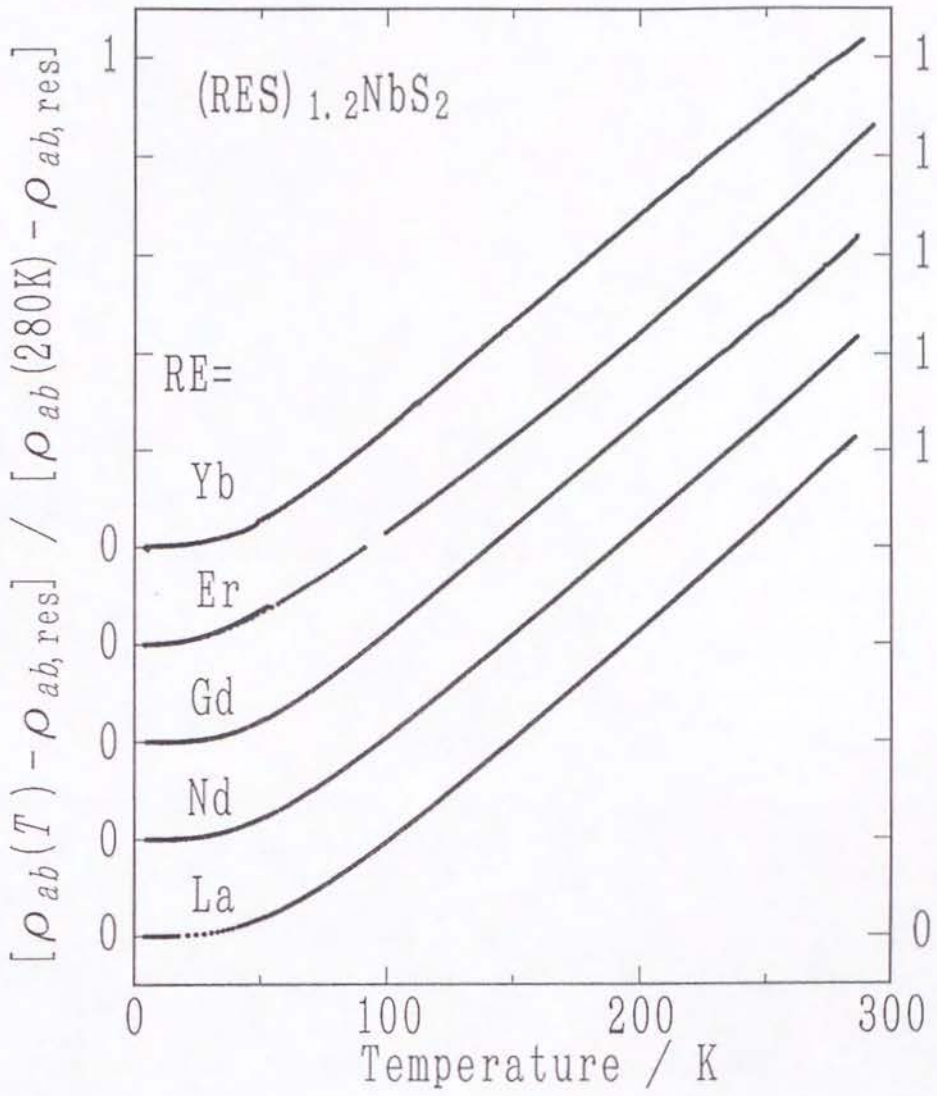

Fig. 4. The normalized temperature dependence of the basal-plane resistivity $[\rho_{ab}(T)-\rho_{ab,res}]/[\rho_{ab}(280\ K)-\rho_{ab,res}]$ for the stage-1 compounds $(RES)_{1.2}NbS_2$ (RE=La,Nd,Gd,Er,Yb).

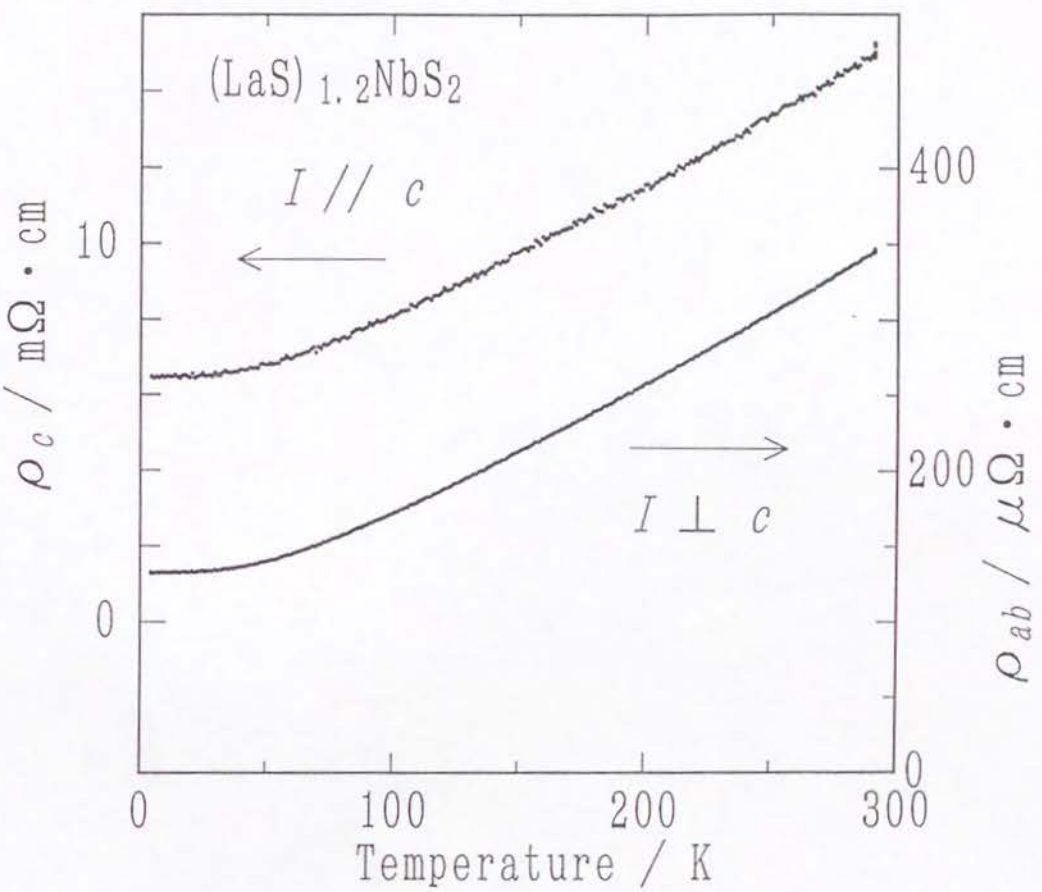

Fig. 5. The *c*-axis and the basal-plane resistivity of $(LaS)_{1.2}NbS_2$.

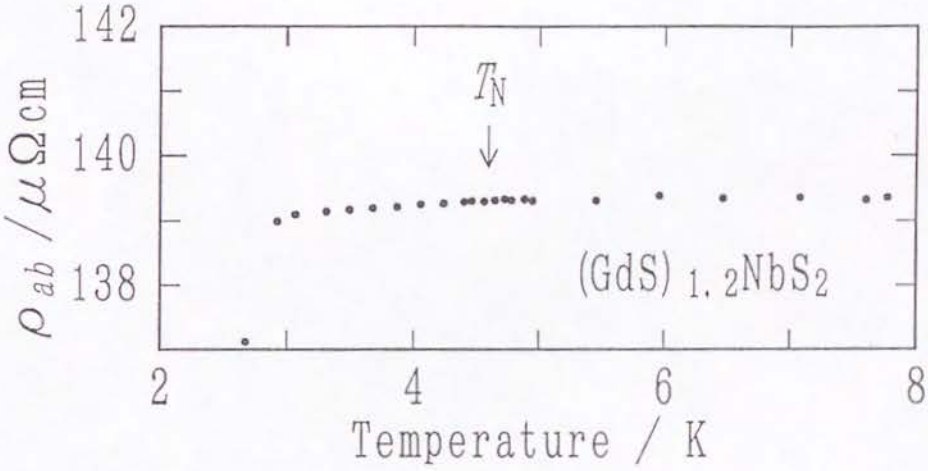

Fig. 6. The basal-plane resistivity of $(GdS)_{1.2}NbS_2$ near the magnetic transition temperature (T_N=4.6 K) [4]. An abrupt decrease below ca. 3 K is due to the fractional superconductivity.

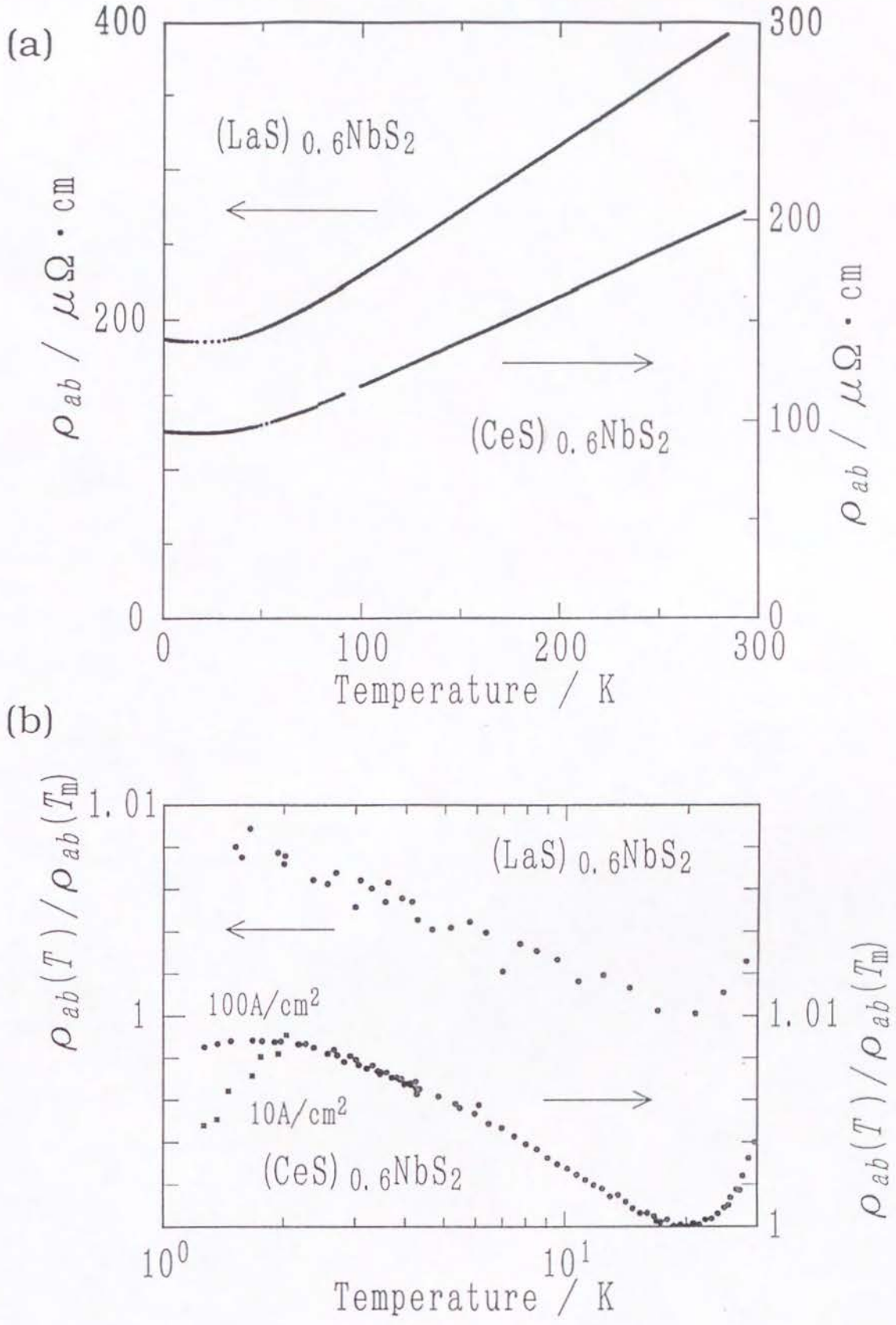

Fig. 7. (a) The basal-plane resistivities of the stage-2 compounds $(LaS)_{0.6}NbS_2$ and $(CeS)_{0.6}NbS_2$. (b) Logarithmic temperature dependences at low temperatures. T_m is the temperature where the resistivity has a maximum. The current-sensitive decrease below ca. 2 K in $(CeS)_{0.6}NbS_2$ is due to the fractional superconductivity.

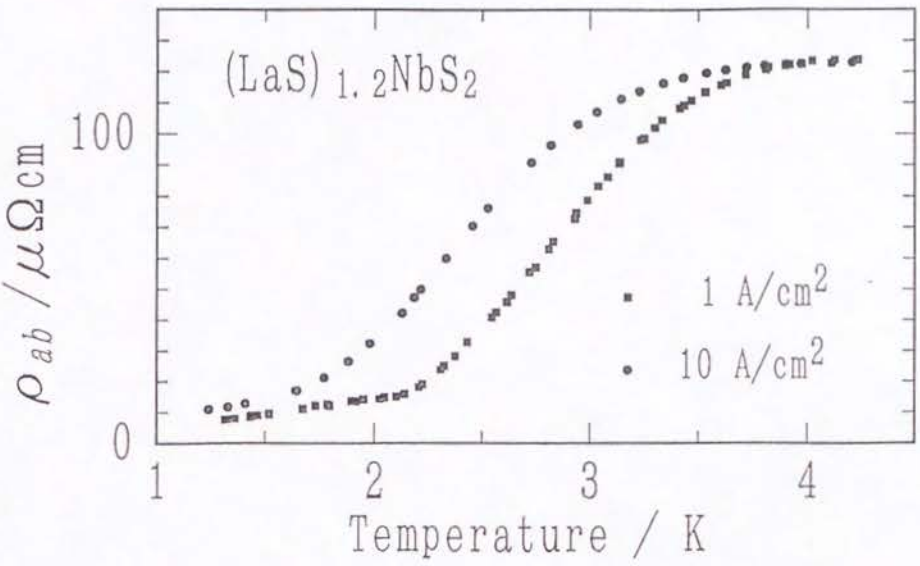

Fig. 8. The basal-plane resistivity of $(LaS)_{1.2}NbS_2$ with two different current densities showing an anomalous decrease due to the fractional superconductivity.

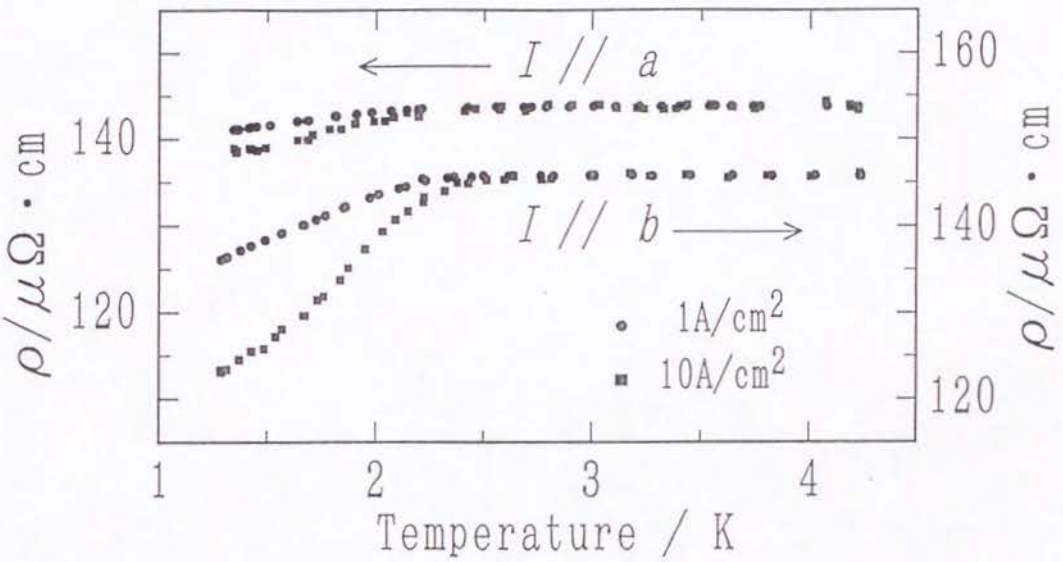

Fig. 9. The *a*-axis and *b*-axis resistivities measured for the single crystal #26-B of $(CeS)_{1.2}NbS_2$ at low temperatures. The figure corresponds to an enlargement of the low temperature part of Fig. 2. A gradual decrease below ca. 2.5 K is due to the fractional superconductivity. No anomaly is seen at the magnetic transition temperature (T_N=3.2 K, see chapter 6).

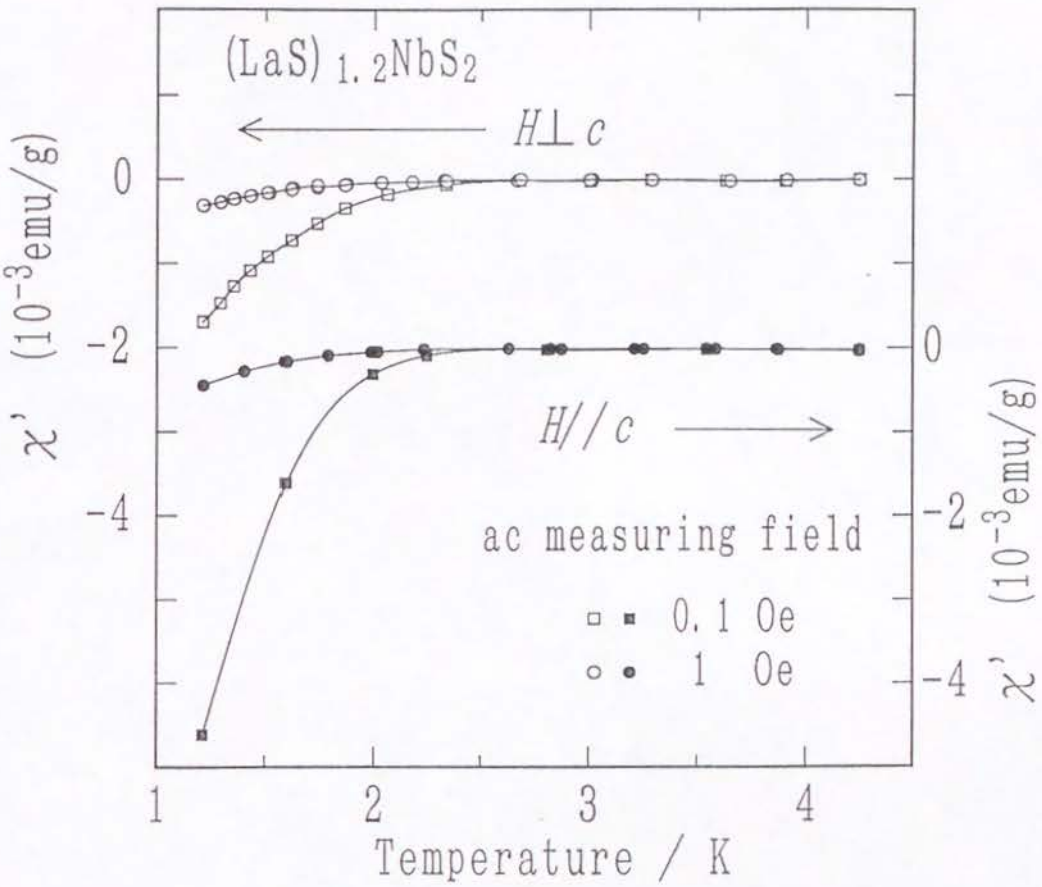

Fig. 10. The ac magnetic susceptibility (real part) χ' of $(LaS)_{1.2}NbS_2$ with two different strengths of the measuring field (86.9Hz).

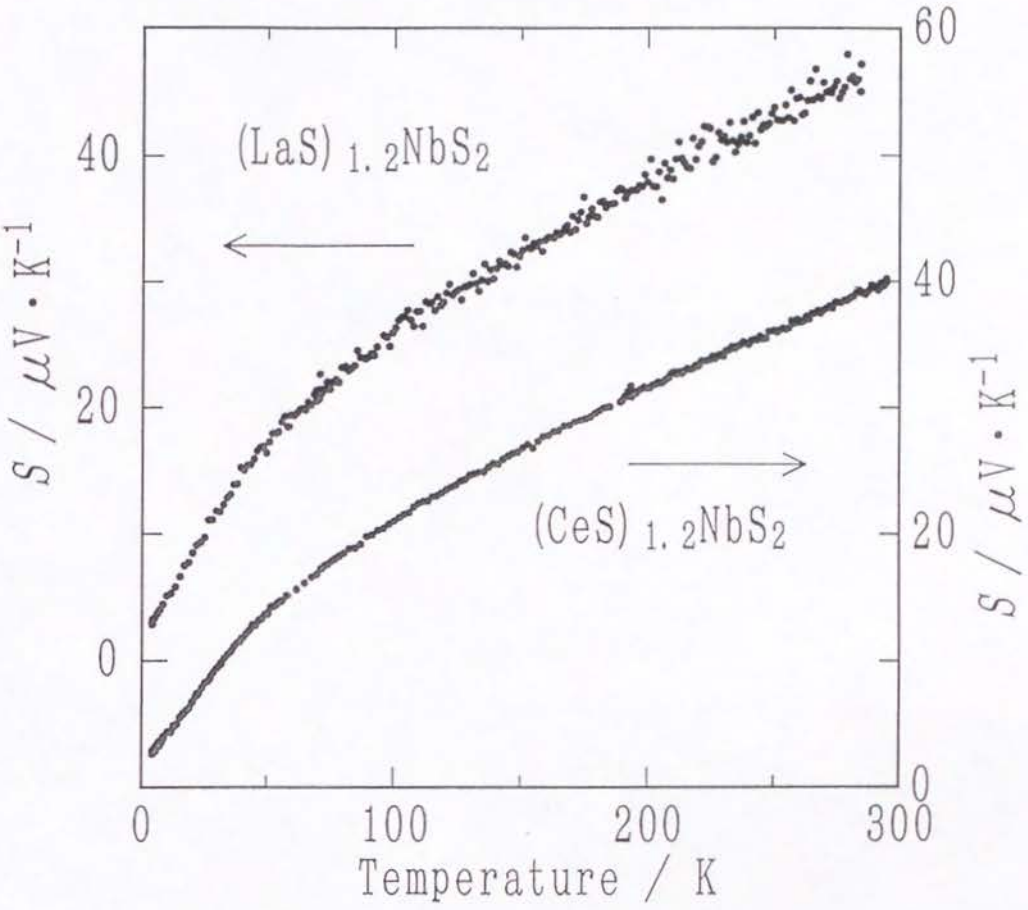

Fig. 11. The Seebeck coefficient of the stage-1 compounds $(LaS)_{1.2}NbS_2$ and $(CeS)_{1.2}NbS_2$.

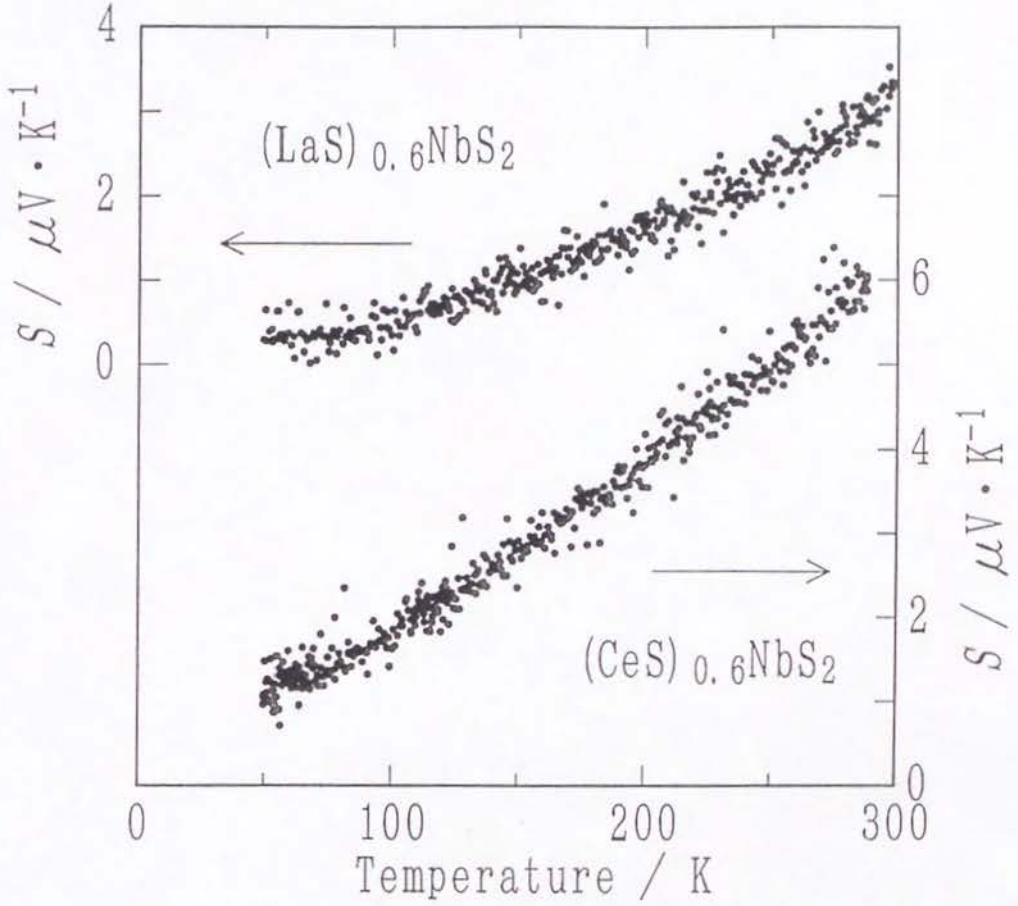

Fig. 12. The Seebeck coefficient of the stage-1 compounds $(LaS)_{0.6}NbS_2$ and $(CeS)_{0.6}NbS_2$.

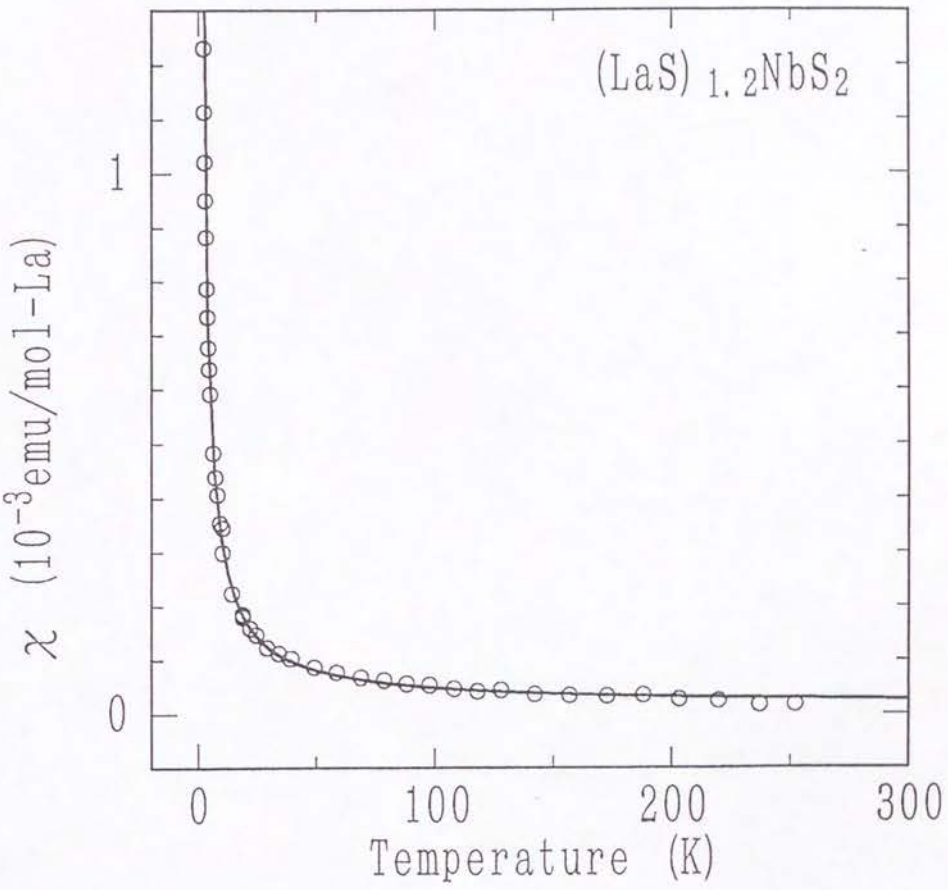

Fig. 13. The dc magnetic susceptibility χ of $(LaS)_{1.2}NbS_2$. The solid line is a Curie-Weiss fit [eq. (2)].

Chapter 5

Optical Properties of the Stage-1 Compound $(CeS)_{1.2}NbS_2$ and the Stage-2 Compound $(CeS)_{0.6}NbS_2$

§1. Introduction

In this chapter, we report the stage-dependent study on the polarized optical reflectivity spectra of the stage-1 compound $(CeS)_{1.2}NbS_2$ and the stage-2 compound $(CeS)_{0.6}NbS_2$. The optical measurement is a direct probe into the electronic structure and different stage correlates immediately with different band filling. These two facts allow us to examine the validity of the rigid-band model in these compounds. In addition, the polarized spectra may reflect the mutual modulation along the incommensurate *a* axis.

The experimental procedures are briefly described in §2. The measured reflectivity spectra and an oscillator fitting to the spectra around the Drude edge are presented in §3. In §4 spectral features arising from interband transitions and characteristics concerning the free carrier reflectivities are discussed in comparison with the reflectivity spectrum of the host material NbS_2.

§2. Experimental

The sample of $(CeS)_{1.2}NbS_2$ were the crystal #26-B from the preparation batch #26, which is the same crystal that used for the single-crystal resistivity measurements in chapter 4.

The sample of $(CeS)_{0.6}NbS_2$ were taken from the preparation batch #103.

Polarized optical reflectivities from freshly-cleaved basal planes were measured at room temperature over the photon energy range of 0.1 eV to 4.1 eV using the microspectrophotometric technique. The incident electric light vector was polarized parallel to the a axis ($E//a$) as well as the b axis ($E//b$). Absolute reflectivities were obtained by normalizing the data with respect to aluminium.

§3. Results

Optical reflectivities of the stage-1 compound $(CeS)_{1.2}NbS_2$ and the stage-2 compound $(CeS)_{0.6}NbS_2$ at room temperature are shown in Figs. 1 and 2, respectively. The overall shapes of the spectra much resemble the reflectivity spectrum of pure NbS_2 for light

polarized $E \perp c$ (E parallel to the basal plane). [1,2] All the spectra show a sharp dip structure, the Drude edge, at low photon energies. The associated reflectivity minima occur at ca. 0.5 eV and 0.7 eV for $(CeS)_{1.2}NbS_2$ and $(CeS)_{0.6}NbS_2$, respectively. These values are considerably smaller than that of pure NbS_2 (ca. 1.1 eV), suggesting a decrease in the plasma frequency ω_p due to smaller carrier concentration.

In the energy region higher than the Drude edge, the spectra are dominated by one broad reflectivity peak B at about 2.3–2.5 eV. The peak B exhibits little anisotropy between the two polarizations of light, $E//a$ and $E//b$. Between the peak B and the Drude edge, a small peak A, although in the case of $(CeS)_{1.2}NbS_2$ a shoulder rather than a well-developed peak, exists around 1 eV. It is somewhat ambiguous whether the shoulder A in the spectra of $(CeS)_{1.2}NbS_2$ is due to interband transitions or not, since the reflectivity above the Drude minimum often shows a convex curvature similar to that in the spectra of $(CeS)_{1.2}NbS_2$. However, we infer from the results of the oscillator fitting mentioned below that interband transitions contribute to this shoulder to some extent. Another small peak, denoted C, can be seen in the $E//b$ spectrum of $(CeS)_{1.2}NbS_2$ around 3.1 eV, whereas such a peak is absent in the $E//a$ spectrum. In the case of $(CeS)_{0.6}NbS_2$, the $E//b$ reflectivity is swelled around 3 eV, compared with the $E//a$ spectrum. This slight bulge, denoted (C), in the $E//b$ spectrum may be of the same origin as the peak C in the $E//b$ spectrum of $(CeS)_{1.2}NbS_2$. Beyond the reflectivity minima at ca. 3.5–3.7 eV, the reflectivities of both the compounds again start to increase, indicating another peak at higher energies.

In order to evaluate plasma frequencies ω_p in these compounds, the experimental reflectivity curves were fitted to a theoretical model. The model dielectric function $\varepsilon(\omega)$ is given by [3]

$$\varepsilon(\omega)=\varepsilon_{core}-\frac{\omega_p^2}{\omega^2+i\gamma\omega}+\sum_{j=A,B}\frac{\Omega_j^2}{\omega_j^2-\omega^2-i\Gamma_j\omega} \quad . \tag{1}$$

The first term ε_{core} is a frequency independent core term describing contributions to the dielectric function from interband transitions in the high energy range. The second term describes the Drude behavior of the free carriers; ω_p is the plasma frequency and γ is a carrier relaxation rate. The last term, two Lorentz oscillators A and B, is introduced to examine the influence of the two peaks A and B on the Drude behavior; ω_j is the frequency of the oscillator, Γ_j is a relaxation rate, and the oscillator strength is proportional to Ω_j^2. From the dielectric function, the reflectivity R can be calculated by [3]

$$R=\frac{1+|\varepsilon|-[2(|\varepsilon|+\mathrm{Re}\ \varepsilon)]^{1/2}}{1+|\varepsilon|+[2(|\varepsilon|+\mathrm{Re}\ \varepsilon)]^{1/2}} \quad . \tag{2}$$

The fitted parameters are listed in Table I and the quality of the fit is exemplified in Fig. 3, where some of the experimental data points for the $E//a$ spectra of $(CeS)_{1.2}NbS_2$ and $(CeS)_{0.6}NbS_2$ are shown together with the fitted theoretical curves. The deviation from the experimental data points above ~ 2.7 eV is due to the effect of neglected reflectivity peak at higher energies.

The parameters concerning the Lorentz oscillators A and B and the core term ε_{core} could not be determined very uniquely. In

connection with the shoulder A, we tried two different types of fits to the spectra of $(CeS)_{1.2}NbS_2$, one with the Lorentz oscillator A and the other without it. The oscillator A appeared necessary to reproduce a small bend of the spectra at ca. 1.5 eV. However, the shoulder A of $(CeS)_{1.2}NbS_2$ and the peak A of $(CeS)_{0.6}NbS_2$ were both too weak structures to decide their parameters accurately. Some ambiguity also existed in the way to distribute the oscillator strength between the Lorentz oscillator B and the core term.

In spite of all these problems, reliable estimations of the plasma frequency ω_p and the carrier relaxation rate γ were obtained, since the values of ω_p and γ were found to be hardly affected by a change in the other parameters as far as they give a reasonable fit to the spectra in the neighborhood of the Drude minima up to about 1 eV.

§4. Discussion

4.1 The interband transitions

We first discuss the features in the interband transition region of the spectra in comparison with those of the host material 2H-NbS_2 on the basis of the rigid-band model. A schematic density-of-states diagram for the host NbS_2 is given in Fig. 3 of chapter 1.

The optical reflectivity spectra (E // the basal plane) of 2H or 3R modifications of NbS_2 have been reported by Beal and Liang [1] and more recently by Parkin and Beal [2] together with its intercalation compounds with Mn, Fe, Co, and Ni. The spectrum of pure NbS_2 shows strong free carrier reflectivity starting from the reflectivity

minimum at ca. 1.1 eV to lower energies. Beyond this reflectivity minimum, there is a poorly-defined structure around 1.5 eV, which is assigned to the transitions from a high density-of-states region of the p/d valence band to the unoccupied portion of the d_{z^2} conduction band. [1,2] The corresponding structure is the peak A in the spectra of the stage-2 compound $(CeS)_{0.6}NbS_2$. The same type of interband transitions probably contributes to the shoulder A in the spectra of the stage-1 compound $(CeS)_{1.2}NbS_2$ as suggested by the oscillator fitting but never develops a well-defined peak. This is quite likely, since the d_{z^2} band is almost filled in $(CeS)_{1.2}NbS_2$ and the unoccupied states above the Fermi level and hence possible transitions to the d_{z^2} band themselves are largely reduced.

The spectrum of pure NbS_2 above 2 eV to ~3.5 eV is dominated by one reflectivity peak at about 2.8 eV. This peak was originally assigned by Beal and Liang [1] to the interband transitions from the high density of states region of the p/d valence band to the d/p conduction band. However, Parkin and Beal [2] have re-assigned the same peak to the interband transitions from the d_{z^2} conduction band to the upper d/p conduction band. It underlies this new assignment that the selection rule which inhibits pure d-d transitions must be relaxed in this case because of the hybridization between the transition-metal d states and the chalcogen p states in the d/p conduction band. The latter assignment is consistent with the joint density-of-states calculated by Mattheiss [4] and by Guo and Liang. [5] It is also experimentally supported by thermoreflectance measurements [7] and by the systematic investigation on the transmission spectra of pure and Li-intercalated TX_2. [8] Therefore,

instead of the original assignment by Beal and Liang, we proceed with the new assignment that the reflectivity peak at about 2.8 eV of NbS_2 is due to the interband transitions from the occupied states of the d_z2 band to the d/p conduction band.

The corresponding structures in $(CeS)_{1.2}NbS_2$ and $(CeS)_{0.6}NbS_2$ are the peak B. Comparing positions of the reflectivity maxima in pure NbS_2 and the present compounds, one can recognize a simple trend. The energy of the reflectivity peak corresponding to the d_z^2–d/p transitions decreases from ca. 2.8 eV through ca. 2.5 eV to ca. 2.3 eV when one going from NbS_2 through the stage-2 compound $(CeS)_{0.6}NbS_2$ to the stage-1 compound $(CeS)_{1.2}NbS_2$. (In the case of the present compounds, this trend also appears in the values of ω_B in the oscillator fitting.) This red shift is reasonably interpreted as arising from the increased filling of the d_z2 band, which lowers the onset energy of the d_z2–d/p transitions. The similar red shift has also been observed in the transmission spectra of Li-intercalated TX_2. For example, the low energy absorption peak due to the d_z2–d/p transitions is located at 3.5 eV in pure 2H-TaS_2 and moves downward upon Li-intercalation, and finally reaches 2.5 eV in the saturated compound $LiTaS_2$. [8]

In the spectra of pure NbS_2 above ~3.5 eV, there exists another much broader peak around 4.8 eV, which is attributed to the transitions from the p/d valence band to the d/p conduction band. [2] The same type of transitions is probably responsible for the reflectivity increase above ~3.5 eV in $(CeS)_{1.2}NbS_2$ and $(CeS)_{0.6}NbS_2$.

In summary, the three main features appeared in the reflectivity spectra of $(CeS)_{1.2}NbS_2$ and $(CeS)_{0.6}NbS_2$ are reasonably

accounted for within the rigid-band model as follows; the peak A results from the p/d–d_z2 transitions, the peak B is due to the d_z2–d/p transitions, and the reflectivity upturn above ~3.5 eV is attributed to the p/d–d/p transitions. It is to be noted these three features show almost no anisotropy between the $E//a$ and the $E//b$ spectrum for both the compounds except that the $E//a$ reflectivity is slightly smaller than the $E//b$ one. The six-fold rotation symmetry of the individual host NbS_2 layer is almost retained in the present compounds; the ratio of the b axis to the a axis of the NbS_2 layer, i.e., b/a_{NbS_2}, in $(CeS)_{1.2}NbS_2$ is 1.741, [6] which is very close to $\sqrt{3}$, the ideal value for the six-fold rotation symmetry. Thus the absence of the inplane anisotropy in the interband transitions associated with the host NbS_2 layer is quite likely.

The rest is the structure denoted C [or (C)], whose origin should be looked for within the intercalate CeS layer. In pristine CeS, the valence band is mainly composed of S $3p$ states, while the conduction band, which is filled with one electron, is of predominantly $5d$ character of cerium. [9] Between them is located the well-localized Ce $4f$ level. The gap between the valence and conduction bands has been estimated at 2.8 eV from x-ray spectroscopic measurements on CeS. [10] If we assume that the energy separation between the S $3p$ states and the Ce $5d$ states in the intercalate CeS layer does not much differ from this value, the structure C may be attributed to transitions from S $3p$ states to Ce $5d$ states in the intercalate CeS layer.

The apparent anisotropy of the structure C, which can be seen only for $E//b$, may be correlated with the structural

incommensurability along the a axis. As has been mentioned in chapter 1, Wiegers *et al.* [6] have analyzed the crystal structure of $(CeS)_{1.2}NbS_2$, dividing the total structure into the two subsystems NbS_2 and CeS. They have remarked that the CeS subsystem is more susceptible to the mutual modulation judging from its larger temperature factors. The electronic structure of the intercalate CeS layer is, therefore, more modulated along the incommensurate a direction by the incommensurate potential forced by the adjacent NbS_2 layer, which may broaden the structure C for $E//a$ and make it discernible in the $E//a$ spectra.

4.2 The plasma frequency and optical effective mass

The parameters ω_p and γ characterizing the Drude behavior of free carriers for both the compounds show practically no anisotropy between the two polarizations, $E//a$ and $E//b$, as the interband transitions attributed to the host NbS_2 layer. It is useful to compare the optically derived dc conductivity σ_{opt} and the results of the resistivity measurements. Using the formula

$$\sigma_{opt} = \frac{{\omega_p}^2}{4\pi\gamma} \quad , \tag{3}$$

we obtain $\sigma_{opt}=3.6\times10^3$ S/cm for$(CeS)_{1.2}NbS_2$ and $\sigma_{opt}=3.0\times10^3$ S/cm for $(CeS)_{0.6}NbS_2$. The basal-plane resistivity measurements for the same crystal of $(CeS)_{1.2}NbS_2$ that used in this study give $\sigma=3.1\times10^3$ S/cm at T=280 K (see chapter 4). In the case of $(CeS)_{0.6}NbS_2$, the resistivity measurements could not be carried out on the present crystal but those done on another two crystals give an

average value of $\sigma=3.1\times10^3$ S/cm at T=280 K (see chapter 4). Taking into account the fact that the values of the resistivity measurements involve an error arising from the estimation of the thin sample thickness, the agreement is satisfactory.

The red shift of the Drude edge already mentioned can be examined quantitatively using the values of the plasma frequency ω_p; $\hbar\omega_p$ is 1.3 eV for $(CeS)_{1.2}NbS_2$ and 1.9 eV for $(CeS)_{0.6}NbS_2$. Unfortunately the plasma frequency in pure NbS_2 was not deduced by Beal and Liang [1] nor by Parkin and Beal, [2] since the small and crumpled crystal surface of NbS_2 made it difficult to decide the absolute values of the reflectivities and hence to estimate the precise value of ω_p by fitting. However, the value of ω_p in 2H–$NbSe_2$ ($\hbar\omega_p$=3.9 eV) [2] can be taken as a good approximation of ω_p in pure NbS_2. Thus it is evident that the plasma frequencies in $(CeS)_{1.2}NbS_2$ and $(CeS)_{0.6}NbS_2$ are largely reduced owing to the large charge transfer from the intercalate CeS layer to the host d_{z^2} band. It is reasonable that the stage-1 compound $(CeS)_{1.2}NbS_2$ has the smaller ω_p than the stage-2 compound $(CeS)_{0.6}NbS_2$, since the charge transfer rate per niobium atom is almost halved in the latter compound.

The optical effective mass m^* of the free carriers can be obtained from ω_p using the relation, [3]

$$\omega_p^2 = \frac{4\pi n e^2}{m^*} \quad , \tag{4}$$

provided the carrier concentration n is known. The carrier concentration in $(CeS)_{1.2}NbS_2$ can be inferred from the Hall

coefficient measurements by Wiegers *et al.* as 0.04 hole/Nb. [6] In the case of $(CeS)_{0.6}NbS_2$, we tentatively assume the complete charge transfer, i.e. one electron/Ce, and hence the value of 0.4 hole/Nb. Then the optical effective masses associated with the carrier motion in the basal plane are estimated at ~$0.3m_e$ and ~$1.8m_e$ for the stage-1 compound $(CeS)_{1.2}NbS_2$ and the stage-2 compound $(CeS)_{0.6}NbS_2$, respectively, although we should bear the error and the uncertainty in the carrier concentrations in mind. The optical effective mass (E // the basal plane) for 2H-$NbSe_2$ is $1.4m_e$, [2] which is again presumed to be an approximation for pure NbS_2. Hence the optical effective mass of the stage-1 compound $(CeS)_{1.2}NbS_2$ is largely reduced from that of host NbS_2, while the optical effective mass of the stage-2 compound $(CeS)_{0.6}NbS_2$ is a little larger.

In general, the optical effective mass is a function of the position of the Fermi level, even within the rigid band-model, unless nearly-free-electron band-structures are dealt with. This is probably enough to account for the slightly larger value of m^* for $(CeS)_{0.6}NbS_2$. However the effective mass of $(CeS)_{1.2}NbS_2$ is too much reduced from that of host NbS_2. Even if we take account of the error in the carrier estimation noted by Wiegers *et al.* [6] (see chapter 4) and adopt a 50% larger value for the carrier concentration, the effective mass is still ~$0.45m_e$. Smaller values of the optical effective mass have also been reported for the 3*d* transition-metal intercalated NbS_2; m^*/m_e is ~1.0 for $Mn_{1/3}NbS_2$ and $Fe_{1/3}NbS_2$, and ~0.4 in $Co_{1/3}NbS_2$ and $Ni_{1/3}NbS_2$. [2] Parkin and Beal [2] have argued this reduction in the optical effective masses in terms of a broadening of the d_{z^2} band due to increased interlayer

bonding; that is, intercalation replaces the weak interlayer interaction of van der Waals type in pure materials with interaction of somewhat bonding character between the intercalate and the host layer in intercalation compounds, which would result in increased bandwidths and hence a smaller effective mass. In comparison with the stage-2 compound $(CeS)_{0.6}NbS_2$, such an effect would be more important in the stage-1 compound $(CeS)_{1.2}NbS_2$, since in the latter compound the intercalate CeS layer is inserted into every one host NbS_2 layer. This might account for the largely reduced optical effective mass in $(CeS)_{1.2}NbS_2$.

§5. Conclusions

We have measured the optical reflectivity spectra of the stage-1 compound $(CeS)_{1.2}NbS_2$ and the stage-2 compound $(CeS)_{0.6}NbS_2$. The main features appeared in the interband transition region of the spectra are well interpreted with the rigid-band model for the electronic band-structure of the host material NbS_2 by taking account of the charge transfer from the intercalate CeS layer. The one feature that cannot be attributed to the host NbS_2 layer is also seen and we have ascribed it to the S $3p$–Ce $5d$ transitions in the intercalate CeS layer. The plasma frequencies in the two compounds have been deduced from the oscillator fitting to the free carrier reflectivities in the spectra. They are considerably reduced from the value reported for 2H-$NbSe_2$, which confirms the large charge transfer from the intercalate CeS layer to the host d_z2 band. The optical effective mass is decreased in $(CeS)_{1.2}NbS_2$ from that

observed for 2H-$NbSe_2$. In this connection, we have discussed possible band broadening due to the increased interlayer bonding. As for this point, however, more experimental investigations such as photoemission measurements are necessary.

References

1) A. R. Beal and W. Y. Liang: Philos. Mag. **33** (1976) 121.

2) S.S.P. Parkin and A. R. Beal: Philos. Mag. B **42** (1980) 627.

3) F. Wooten: Optical Properties of Solids (Academic Press, New York, 1972).

4) L. F. Mattheiss: Phys. Rev. B **8** (1973) 3719.

5) G. Y. Guo and W. Y. Liang: J. Phys. C: Solid State Phys. **20** (1987) 4315.

6) G. A. Wiegers, A. Meetsma, R. J. Haange, and J. L. de Boer: J. Solid State Chem. **89** (1990) 328.

7) G. Campagnoli, A. Gustinetti, and A. Stella: Solid State Commun. **18** (1976) 973.

8) A. R. Beal and S. Nulsen: Philos. Mag. B **43** (1981) 985.

9) P. Wachter: Phys. Rep. **44** (1978) 159.

10) A. N. Gusatinskii, G. I. Alperovich, and A. V. Soldatov: Phys. Status Solidi B **112** (1982) 599.

Table I. Optical parameters obtained by the oscillator fitting [eq. (1)] of the reflectivity spectra of $(CeS)_{1.2}NbS_2$ and $(CeS)_{0.6}NbS_2$.

Parameter (unit)		ε_{core}	$\hbar\omega_p$ (eV)	$\hbar\gamma$ (eV)	$\hbar\omega_A$ (eV)	$\hbar\Omega_A$ (eV)	$\hbar\Gamma_A$ (eV)	$\hbar\omega_B$ (eV)	$\hbar\Omega_B$ (eV)	$\hbar\Gamma_B$ (eV)
$(CeS)_{1.2}NbS_2$	$E // a$	3.47	1.30	0.063	1.30	0.70	0.65	2.15	4.63	1.05
	$E // b$	3.58	1.32	0.065	1.28	0.75	0.64	2.11	4.77	1.01
$(CeS)_{0.6}NbS_2$	$E // a$	3.10	1.88	0.167	1.19	1.38	0.82	2.31	5.00	1.47
	$E // b$	3.20	1.93	0.160	1.19	1.38	0.82	2.31	5.35	1.45

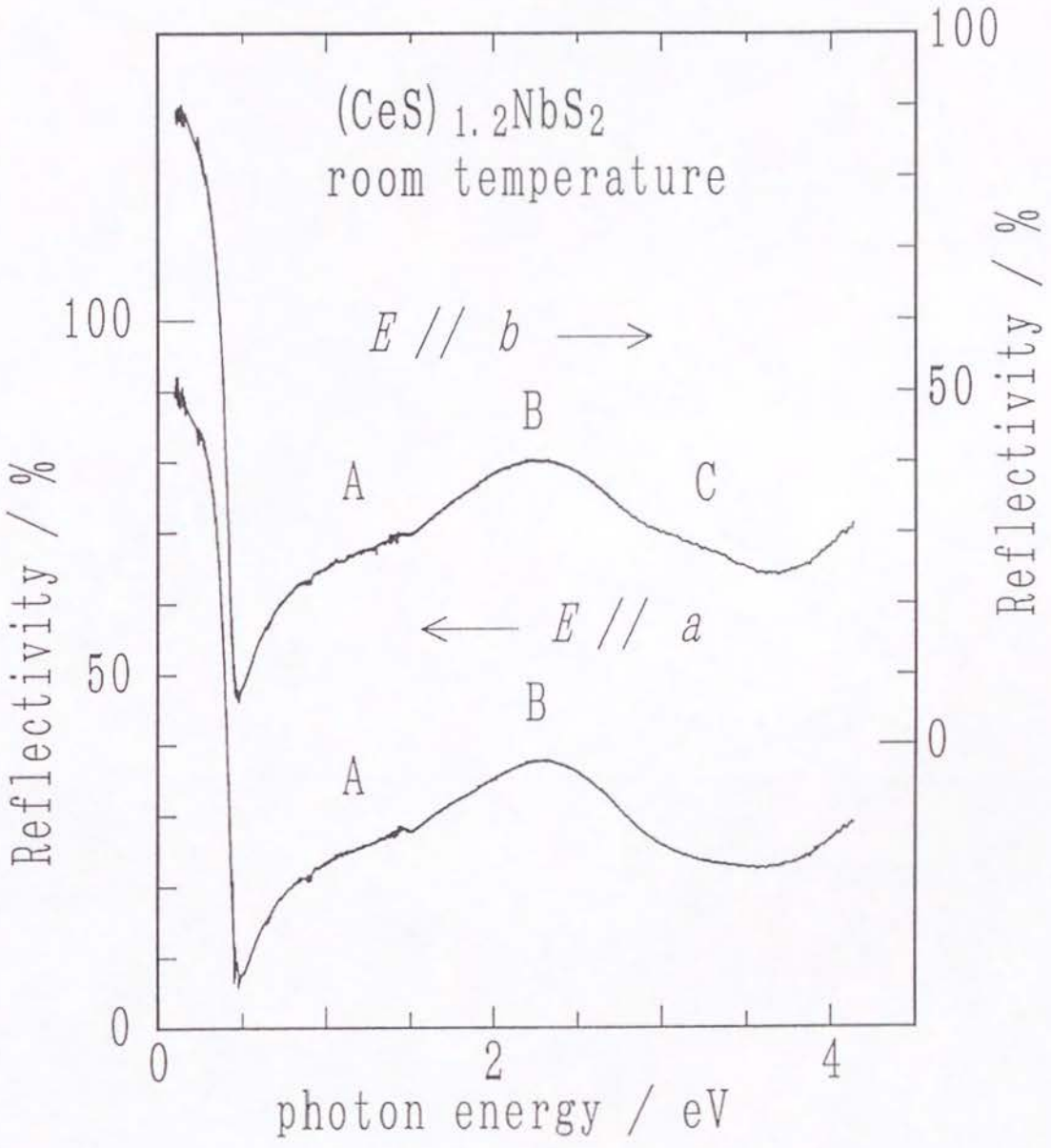

Fig.1. The optical reflectivity of the stage-1 compound $(CeS)_{1.2}NbS_2$ for light polarized $E//a$ (lower curve, left scale) and $E//b$ (upper curve, right scale) at room temperature.

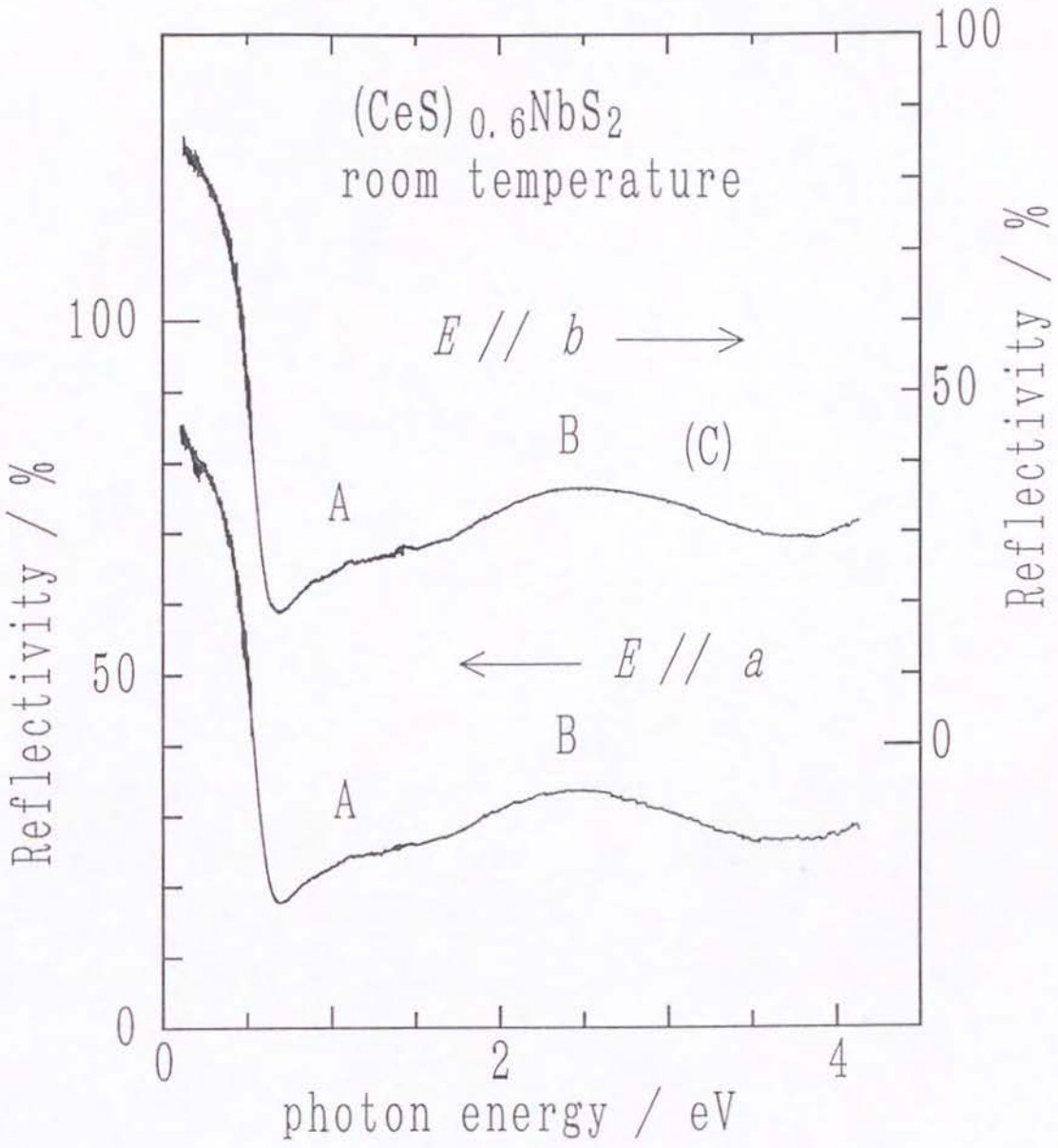

Fig.2. The optical reflectivity of the stage-2 compound $(CeS)_{0.6}NbS_2$ for light polarized $E//a$ (lower curve, left scale) and $E//b$ (upper curve, right scale) at room temperature.

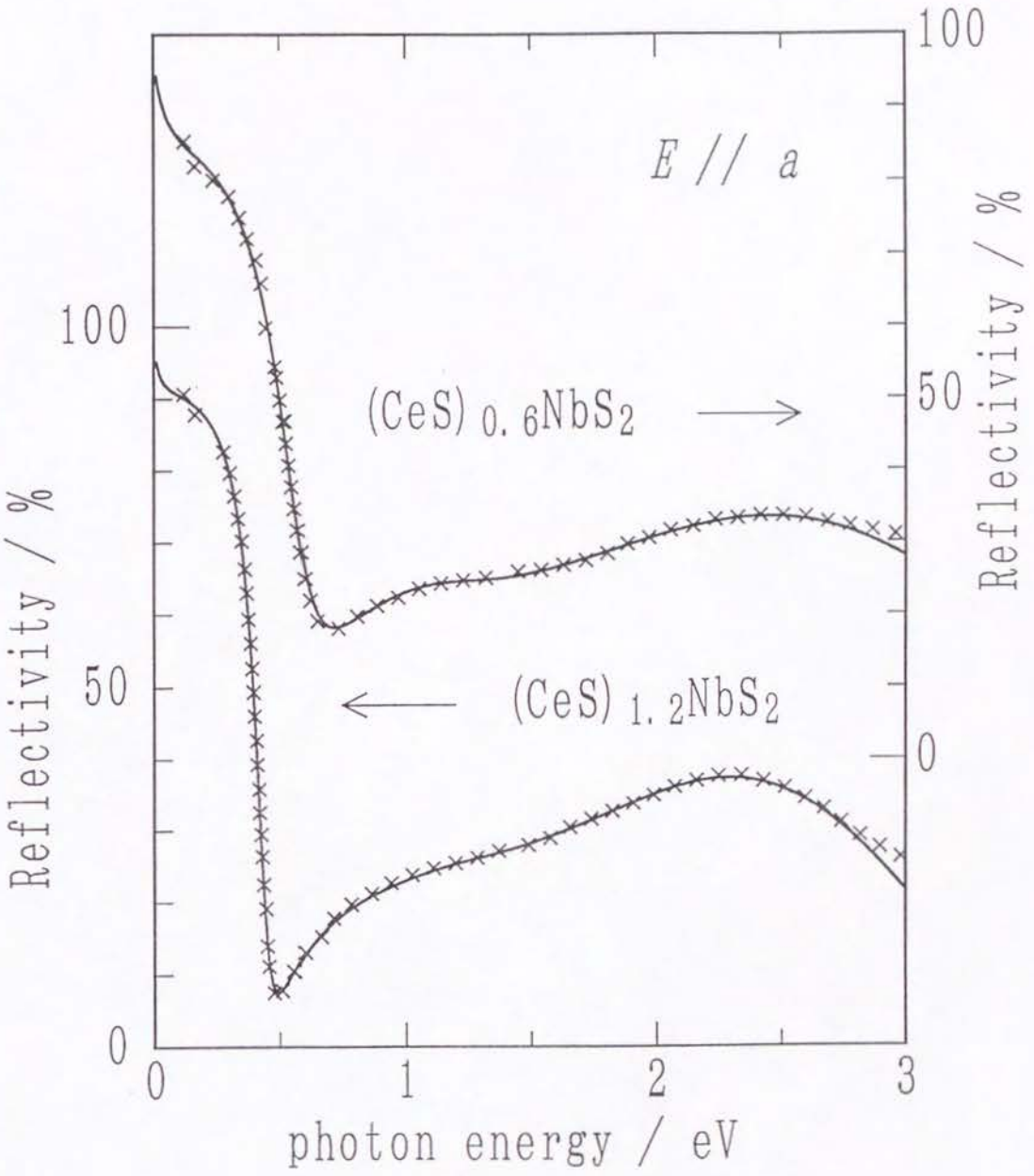

Fig.3. The oscillator fitting of the $E//a$ reflectivity spectra of $(CeS)_{1.2}NbS_2$ and $(CeS)_{0.6}NbS_2$ around the Drude edge (full line). A part of the measured data points (ca. 1/50 of the total measured points) is plotted together (cross).

Chapter 6

Magnetic Properties of the Stage-1 Compound $(CeS)_{1.2}NbS_2$ and the Stage-2 Compound $(CeS)_{0.6}NbS_2$ by Means of the Magnetic Susceptibility and Magnetization Measurements

§1. Introduction

In this chapter, we report experimental results on the magnetic susceptibility and magnetization for both the stage-1 compound $(CeS)_{1.2}NbS_2$ and the stage-2 compound $(CeS)_{0.6}NbS_2$.

We will analyze magnetic susceptibilities by taking into account the crystal field and molecular field effects. The magnetic exhange interaction and ordering will be also discussed.

§2. Experimental

Magnetic measurements down to 1.9 K and up to 42 kOe were carried out with a Faraday balance. Magnetic susceptibilities in the paramagnetic state were measured at 10 kOe.

Two single crystals of $(CeS)_{1.2}NbS_2$, #18-A and #26-B, were separately used in these measurements. The crystal #18-A weighing 1.01 mg was taken from the batch #18 and the crystal #26-B weighing 3.13 mg from the batch #26. The measurements were done along all the three crystallographic axes, which were determined from Weissenberg photographs.

In the case of $(CeS)_{0.6}NbS_2$, measurements were done parallel and perpendicular to the *c* axis. The sample consisted of twelve small crystals from the batch #103 whose *c* axes were oriented appropriately to the field direction. The total weight was 2.46 mg. The magnetization at a low field of 15 Oe and a hysteresis loop at 2.0 K of $(CeS)_{0.6}NbS_2$ were measured with a SQUID magnetometer.

AC magnetic susceptibility measurements in nearly zero field (86.9 Hz, less than 2 Oe) were performed between 1.2 and 4.2K by means of ac Hartshorn bridge. The measurements were carried out on four different batches of $(CeS)_{1.2}NbS_2$, #10, #15, #18, and #101 to elucidate the batch dependence of the transition temperature and also on the same sample for $(CeS)_{0.6}NbS_2$ as used in the Faraday

method. Magnetic field was applied parallel and perpendicular to the *c* axis. (The preparation conditions for each batch are given in Table I of chapter 2.)

§3. Results

3.1 $(CeS)_{1.2}NbS_2$ and $(CeS)_{0.6}NbS_2$ in the paramagnetic state

Reciprocal magnetic susceptibilities of $(CeS)_{1.2}NbS_2$ and $(CeS)_{0.6}NbS_2$ are shown as a function of temperature in Figs. 1 and 2 ,respectively. The reciprocal susceptibilities do not obey the Curie-Weiss law and exhibit a convex curvature. The effective magnetic moments calculated from the slopes between 200 and 250 K all deviate from the free Ce^{3+} ion value of $2.54\mu_B$ (Table I). The convex curvature and the deviation of the moment from the free Ce^{3+} value suggest large crystal field effects.

Below 30 K the reciprocal susceptibilities lie on straight lines [Figs. 1(b) and 2(b)], indicating that only the lowest lying doublet are virtually occupied. The effective moments and paramagnetic Curie temperatures determined from the lines in Figs. 1(b) and 2(b) are also listed in Table I. The obtained effective moments are rather isotropic. The paramagnetic Curie temperatures are positive along the *c* axis, whereas negative perpendicular to the *c* axis.

3.2 $(CeS)_{1.2}NbS_2$ near T_N

The nearly zero field ac susceptibility of $(CeS)_{1.2}NbS_2$ measured on #18 is shown for both parallel and perpendicular orientations to the *c* axis in Fig. 3. The anisotropy of susceptibility

$\chi_{//c}/\chi_{\perp c}$ at 4.2 K exceeds 9, reflecting the positive Curie temperature along the *c* axis. The *c* axis susceptibility $\chi_{//c}$ gradually increases on cooling, shows a broad maximum at 3.2 K, and then steeply decreases below 3.0 K tending to zero. The susceptibility perpendicular to the *c* axis $\chi_{\perp c}$ is almost featureless in the measured temperature range, except a sharp peak at 2.98 K. The behaviors of $\chi_{//c}$ and $\chi_{\perp c}$ are well understood as the parallel and perpendicular susceptibilities of an antiferromagnet, except the sharp peak in $\chi_{\perp c}$. The compound $(CeS)_{1.2}NbS_2$ is therefore basically an antiferromagnet where the *c* axis is an easy axis. The Néel temperature T_N which defined as the temperature where the $\chi_{//c}$ curve has a maximum slope is 2.96 K in this batch (#18). The Néel temperature, however, differs from batch to batch; 2.9 K in #15, 2.57 K in #10, and 3.48 K in #101.

Magnetization curves measured at 4.4 and 2.0 K are shown in Fig. 4. The measurements on two different single crystals are in fairly good agreement with each other. The *a*- and *b*-axis magnetizations increase linearly with field both above and below T_N. The *c*-axis magnetization at T=4.4 K shows a rapid increase at low fields and the tendency of saturation is apparent at high fields. The *c*-axis magnetization at T=2.0 K is small at low fields due to a small parallel susceptibility of an antiferromagnet, but increases abruptly at H_c=2.3 kOe, indicating a metamagnetic transition. The magnetization almost saturates above H_c, reaching the value of $0.76\mu_B$/Ce at 40 kOe which is considerably smaller than the free Ce^{3+} ion value of $2.14\mu_B$/Ce.

The sharp peak of the perpendicular susceptibility is located, within experimental error, just at the Néel temperature T_N and indicates that a weak-ferromagnetic moment develops in the basal plane below T_N, as is the case with various weak-ferromagnets. [1] We therefore measured the *a*- and *b*-axis magnetizations in a low field of 90 Oe as a function of temperature around T_N for the two crystals. (The results for the crystal #26-B are shown in Fig. 5.) As shown in Fig. 5, a weak-ferromagnetic moment develops only along the b axis, which corresponds to the fit direction. The moment reaches $0.02\mu_B$/Ce at 2.0 K, which is only 2% of the saturation moment along the *c* axis.

3.3 $(CeS)_{0.6}NbS_2$ near T_N

The nearly zero field ac susceptibility of $(CeS)_{0.6}NbS_2$ is shown in Fig. 6. The *c*-axis susceptibility shows a large sharp peak. Defining the transition temperature as the point of the maximum susceptibility, we derive T_N=2.97K. The *c*-axis magnetization at a small filed of 15 Oe is shown as a function of temperature in Fig. 7, where the magnetization measured perpendicular to the *c*-axis at 150 Oe is also depicted in a 1/10 scale for comparison. The *c*-axis magnetization exhibits a step-like increase at T_N, which indicates a magnetic ordering with a spontaneous magnetization along the *c* axis. The hysteresis loop at 2.0 K is shown in Fig. 8. The spontaneous magnetization is only $0.08\mu_B$/Ce and hence the ordered state cannot be accounted to be a simple ferromagnetic one with spins fully directed to the *c* direction. The magnetization at higher fields is shown in Fig. 9. The magnetization curves both above and

below T_N are fairly similar to those of $(CeS)_{1.2}NbS_2$. The *c*-axis magnetization curve at T=2.0 K, which has a spontaneous magnetization at nearly zero field, shows a metamagnetic transition at H_c=2.3 kOe. The saturation moment along the *c* axis is $0.69\mu_B$/Ce at 41 kOe.

§4. Discussion

4.1 Crystal field analysis

In this section, we will treat the crystal field theory to analyze the susceptibility data. The $^2F_{5/2}$ ground multiplet of a free Ce^{3+} ion splits into three Kramers doublets under a crystal field of a local symmetry lower than a cubic one. We make the following two approximations. First, Ce^{3+} ions for all the sites are treated as equivalent. Secondly, the most pronounced anisotropy observed in the measured susceptibilities is an axial one and hence we take the crystal field to be of tetragonal symmetry, neglecting an anisotropy in the basal plane. The crystal field Hamiltonian $\mathcal{H}_{CF}$ [2] in this case is written as

$$\mathcal{H}_{CF} = B_2^0 O_2^0 + B_4^0 O_4^0 + B_4^4 O_4^4 \quad , \qquad (1)$$

where O_m^n are the Stevens operators and B_m^n are the crystal field parameters to be empirically evaluated. We have taken the *c* axis as the *z* axis, and hence the total angular momentum operators expressed as $J_{//c}$ and $J_{\perp c}$ in the following mean J_z and J_x,

respectively. The eigen functions of the three Kramers doublets are expressed as

$$|1\pm\rangle = \cos\theta\,|\pm 5/2\rangle + \sin\theta\,|\mp 3/2\rangle \quad , \tag{2}$$

$$|2\pm\rangle = \sin\theta\,|\pm 5/2\rangle - \cos\theta\,|\mp 3/2\rangle \quad , \tag{3}$$

$$|3\pm\rangle = |\pm 1/2\rangle \quad , \tag{4}$$

where $\cos\theta$ and $\sin\theta$ are calculated from B_m^n so as to diagonalize the Hamiltonian (1). The crystal-field-only susceptibility χ_α^{CF} can be calculated from the formula, [3]

$$\chi_\alpha^{CF} = \frac{N_A g_J^2 \mu_B^2}{Z_0} \left(\sum_{i,k}^{E_i = E_k} |\langle k|J_\alpha|i\rangle|^2 \frac{e^{-E_k/k_B T}}{k_B T} \right.$$

$$\left. + \sum_{i,k}^{E_i \neq E_k} |\langle k|J_\alpha|i\rangle|^2 \frac{e^{-E_k/k_B T} - e^{-E_i/k_B T}}{E_i - E_k} \right) \quad , \tag{5}$$

where $\alpha = //c$ or $\perp c$ for the susceptibility parallel or perpendicular to the c axis respectively, and

$$Z_0 = \sum_k e^{-E_k/k_B T} \quad , \tag{6}$$

Here, N_A is the Avogadro's number, k_B the Boltzmann constant, g_J , Landé factor, which is 6/7 for the $^2F_{5/2}$ multiplet, μ_B the Bohr magneton, and E_i the energy of the crystal field eigen function $|i\rangle$ (i=1±,2±,3±). Note that $E_{1+}=E_{1-}$, $E_{2+}=E_{2-}$, and $E_{3+}=E_{3-}$.

In order to compare the theoretical susceptibility with experimental data, it is necessary to take into account the exchange

effects. In the molecular field approximation, [4] the paramagnetic susceptibility to be compared with experiments is given by

$$1/\chi_\alpha = 1/\chi_\alpha^{CF} - \gamma_\alpha \,. \tag{7}$$

Taking account of the observed anisotropy in the paramagnetic Curie temperatures, we have used a direction dependent molecular field constants γ_α (α=//c,$\perp c$). The molecular field constants can be related to the intralayer exchange constants $\mathcal{J}_\alpha$ by

$$\mathcal{J}_\alpha = \frac{N_A g_\alpha^2 \mu_B^2}{2z}\gamma_\alpha \,, \tag{8}$$

where z is the number of the intralayer nearest neighbors. According to the x-ray structural determination of $(CeS)_{1.2}NbS_2$, [5] within one CeS layer a given Ce^{3+} ion has four Ce^{3+} neighbors at 4.06Å on the same side of the layer and four at 4.50Å on the opposite side. These eight neighbors have a similar superexchange path via an intervening S atom and hence they are treated as the intralayer nearest neighbors as a whole, i.e., z=8. The g-factors of the lowest lying doublet g_α can be calculated from the formulae, [6]

$$g_{//c} = 2g_J|\langle +|J_{//c}|+\rangle| \,, \tag{9}$$

$$g_{\perp c} = 2g_J|\langle +|J_{\perp c}|-\rangle| \,, \tag{10}$$

where $|+\rangle$ and $|-\rangle$ denote the eigen functions of the lowest lying doublet. It is to be noted that in eq. (8) we have defined the

exchange constants referring to the lowest lying doublet described by a fictitious spin $s'=1/2$ as follows,

$$\mathcal{H}_{ex} = -2\sum_{<ij>} [\mathcal{J}_{//c} s_i^z s_j^z + \mathcal{J}_{\perp c}(s_i^x s_j^x + s_i^y s_j^y)] \quad , \qquad (11)$$

Using the crystal field parameters B_m^n and the molecular field constants γ_α as adjustable parameters, theoretical susceptibilities were fitted with the experimental data. In the case of $(CeS)_{1.2}NbS_2$, a numerically obtained average of the *a*- and *b*-axes susceptibilities was used in the fitting procedure of the perpendicular susceptibility. The parameters to give the best fits are listed in Table II. Resultant curves and energy levels are drawn with experimental data points in Figs. 1(a) and 2(a). One can see that the fits are satisfactory.

The obtained values of the crystal field parameters are much alike between the two compounds, which reflects a similarity in a local environment around Ce^{3+} ions. When taking into account the fact that the present compounds are metallic conductors, the found splittings over 500 K are surprisingly large. In a series of cerium sulfides, the crystal field splitting decreases from 385 K in semiconducting Ce_2S_3 through 250 K in metallic Ce_3S_4 to 120 K in metallic CeS, just in order as the carrier concentration increases. [7] This trend has been thought to arise from increasing screening of the crystal field by free carriers. Thus the observed large crystal field splittings, which are even larger than that of semiconducting Ce_2S_3, imply that the crystal field around the Ce^{3+} ion in $(CeS)_{1.2}NbS_2$ and $(CeS)_{0.6}NbS_2$ is hardly screened by free carriers.

As has been discussed in chapter 4, if we naively assume that the rigid-band approximation is applicable not only to the host electronic band-structure but also to the intercalate one, we can expect the intercalate band of mainly Ce 5*d* character to exist at the Fermi level. However this conjecture is quite inconsistent with the observed large splittings. We therefore suspect that the Ce 5*d* electrons are forced to be semiconducting by some mechanisms.

The lowest lying doublets are $|2\pm\rangle$ for both the compounds with similar values of the coefficients, $\sin\theta$ and $\cos\theta$;

$0.791|\pm5/2\rangle - 0.612|\mp3/2\rangle$ for $(CeS)_{1.2}NbS_2$,

and

$0.742|\pm5/2\rangle - 0.671|\mp3/2\rangle$ for $(CeS)_{0.6}NbS_2$.

The *g*-factors g_α calculated for these doublets are almost isotropic for both the compounds (Table II), which is consistent with the fact that the effective moments estimated below 30K are almost isotropic and that the magnetizations perpendicular to the *c* axis steadily increase and approach the *c* axis one at high fields. It is to be noted the theoretical saturation moment along the *c* axis, $(1/2)g_{//c}\mu_B$, agrees fairly well with the observed one for both the compounds. On the other hand, the exchange constants are quite anisotropic, which will be discussed later in connection with anisotropic exchange interactions.

4.2 Magnetic ordering and exchange interaction

The Néel temperature T_N of $(CeS)_{1.2}NbS_2$ shows the variation between 2.57 and 3.48 K from batch to batch. In general magnetic properties of cerium chalcogenides are very sensitive to chemical

composition and crystal perfection, as has been reported by several authors. [7,8] In our case crystals prepared at a higher temperature seem to have a higher T_N. The tendency might be related to the sulfur deficiency which would increase at a higher temperature. It is also to be considered that the oxidation of the starting cerium fillings during handling probably affects the magnetic properties of the compounds. More careful preparation and characterization is necessary for further study. It is also to be noted that Peña *et al.* [9] have reported a still smaller T_N of 1.95 K for the same compound $(CeS)_{1.2}NbS_2$. The value is out of the range of our T_N. This would partly be attributed to the fact that they determined T_N from the powder susceptibility at a large field of 1 kOe. The Néel temperature of a compound showing a metamagnetic transition, such as the present compound, is likely to be underestimated when evaluated from the susceptibility measured at a high field.

The Néel temperature of $(CeS)_{0.6}NbS_2$ is located in the same temperature range as those of $(CeS)_{1.2}NbS_2$, although the interlayer nearest neighbors are about twice more distant. This indicates that the magnetic transition in both the compounds is mainly ruled by the intralayer exchange interaction.

The exchange constants obtained from the analysis of the reciprocal susceptibilities are anisotropic for both the compounds; the *c*-axis component $\mathcal{J}_{//c}$ is positive, whereas the perpendicular one $\mathcal{J}_{\perp c}$ negative and much smaller. The anisotropy does not come from that in the *g*-factors, since the *g*-factors are almost isotropic and cannot account for the reversal in sign. It is an anisotropic interaction between magnetic $4f$ electrons of cerium ions that is

responsible for this anisotropy. Extensive theoretical studies [10] have shown that for ions with strong orbital contributions to their magnetic moments, as is the case with rare earth ions, one can expect a quite anisotropic exchange interaction, the magnitude of which is of the same order as isotropic one.

By the larger c-axis component $J_{//c}$, Ce^{3+} spins are constrained to point to the c direction and an Ising character of spins can be expected. This is well demonstrated by the metamagnetic transition of $(CeS)_{1.2}NbS_2$. The critical field H_c is only 2.3 kOe and we can safely attribute the exchange interaction responsible for this transition to an interlayer one. A simple relation $g_{//c}\mu_B H_c = z'|J'|$, where z' is the number of the interlayer nearest neighbors, i.e., z'=4, yields the interlayer exchange constants J' of −0.07 K. The ratio $|J_{//c}/J'|$ is about 18 and confirms a quasi two-dimensional character of the magnetic system. Consequently we can arrive at a natural description of a spin structure of $(CeS)_{1.2}NbS_2$ as follows; within one CeS layer the spins are aligned along the c axis and coupled ferromagnetically via the intralayer exchange interaction $J_{//c}$ and along the c axis such ferromagnetic layers are weakly coupled antiferromagnetically via the interlayer exchange interaction J'.

In the same line of discussion we can assume a spin structure of $(CeS)_{0.6}NbS_2$ consisting of ferromagnetic layers. In this assumption, a long-period structure along the c axis, for example a structure consisting of four up spin layers and five down spin layers, is necessary to explain the ordered phase with the spontaneous magnetization which is about one ninth of the saturation moment.

Such a long-period structure can be stabilized if the exchange interaction between layers is of a long-range and competing nature. In fact, theoretical studies on the axial next nearest neighbor Ising (ANNNI) model [11] have shown if the next nearest neighbor interlayer-interaction $\mathcal{J}_2$ is negative and if the ratio to the nearest neighbor interlayer-interaction $\mathcal{J}_1$ satisfies a condition $|\mathcal{J}_2/\mathcal{J}_1|>1/4$, long-period modulated phases occur below the transition temperature.

In the present compounds the RKKY exchange interaction mediated by conduction electrons associated with the host NbS_2 layer may give rise to such a long-range competing interaction. The RKKY interaction can be divided into two parts; the triggering exchange interaction, $\mathcal{J}_{cf}$, between the conduction electrons and the local $4f$ moments, and a long-range conduction electron spin polarization due to the former. In usual metals the former, $\mathcal{J}_{cf}$, arises from a direct exchange interaction between the conduction and $4f$ electrons. However, in the present compounds, a superexchange interaction between the conduction and $4f$ electrons through S atoms in the host NbS_2 layer may be an origin of $\mathcal{J}_{cf}$. The concept of superexchange mechanism between the conduction electrons and the local spins has been successfully applied to the π-d exchange interaction in the $CoCl_2$-graphite intercalation compounds. [12] The RKKY interaction oscillates with the separation of the moments, d, as $\cos(2k_F d)/d^3$ in the simplest approximation and is very sensitive to changes in the Fermi surface in real materials. [13] The Fermi wave vector k_F and hence the Fermi surface are changed drastically going from $(CeS)_{1.2}NbS_2$ to $(CeS)_{0.6}NbS_2$ as

has been indicated by the drastic change in the Seebeck coefficients (see chpter 4). This may account for the difference in the ordered state between the two compounds.

One final point of interest is the weak-ferromagnetism observed in $(CeS)_{1.2}NbS_2$. It is clear that the simple model introduced in §4.1 fails to account for this. Any spin canting from the *c* axis would be energetically unfavorable because $J_{//c} > |J_{\perp c}|$. Our speculation, which is somewhat reminiscent of weak-ferromagnetism arising from a single ion anisotropy like in NiF_2, [1] is as follows. Considering the incommensurate nature of the structure, the exact symmetry of the Ce^{3+} site is much lower than tetragonal and differs from site to site. Due to lower symmetry terms in a crystal field Hamiltonian, the principal magnetic axes do not necessarily coincide with the crystallographic *c* axis. In such a case, when Kramers degeneracy is lifted up by the exchange interaction, even a molecular field along the *c* axis alone can produce a magnetic moment perpendicular to the *c* axis. The magnetic moment of the individual spin differs from site to site and, we suppose, as a whole appears as a weak-ferromagnetic moment only along the *b* axis (the fit direction). If the above explanation is true, $(CeS)_{0.6}NbS_2$ can also have a net magnetic moment in the basal plane. However a definite experimental evidence could not be obtained, since only small amounts of crystals were available and they were arranged randomly as to the intralayer axes.

§5. Summary and Conclusions

We have measured the magnetic susceptibility and magnetization of $(CeS)_{1.2}NbS_2$ and $(CeS)_{0.6}NbS_2$.

The magnetic susceptibilities in the paramagnetic region can be successfully described with the simple model including the tetragonal crystal field and the molecular field of an axial symmetry. The large crystal field splitting of Ce^{3+} over 500K gives an evidence that the Ce 5*d* electrons are induced to become semiconducting. By the anisotropy in the exchange interaction the spins at low temperatures behave as an Ising-like spin bound along the *c* axis.

The two compounds both order magnetically near 3K. The Néel temperatures are somewhat scattered from batch to batch, which indicates the magnetic properties of these compounds are sensitive to the stoichiometry and crystal perfection.

The magnetic structure in the ordered state can be modeled as a system consisting of the ferromagnetic CeS layers; the layers couple antiferromagnetically in $(CeS)_{1.2}NbS_2$, while they seem to form a long-period structure in $(CeS)_{0.6}NbS_2$. The ratio of the intralayer to the interlayer exchange interaction in the former compound is estimated at about 18, which confirms these compounds are quasi two dimensional magnetic systems.

Another significant feature appearing in $(CeS)_{1.2}NbS_2$ is weak-ferromagnetism, which we have attempted to correlate with the incommensurate structure.

References

1) T. Moriya: *Magnetism*, eds. G.T. Rado and H. Suhl (Academic Press, New York, 1963) Vol.1, p.86.

2) U. Walter: J. Phys. Chem. Solids **45** (1984) 401.

3) T. Murao: *Kotaibutsurigaku* (Solid State Physics) (Kyoritsu, Tokyo, 1985) p.157 [in Japanese].

4) J. S. Smart: *Effective Field Theories of Magnetism* (W.B.Saunders, Philadelphia, 1966).

5) G.A. Wiegers, A. Meetsma, R.J. Haange and J.L. de Boer: J. Solid State Chem. **89** (1990) 328.

6) R.J. Elliott and K.W.H. Stevens: Proc. Roy. Soc. A **218** (1953) 553.

7) I. Mörke, E. Kaldis and P. Wachter: Phys. Rev. B **33** (1986) 3392.

8) F. Hulliger, B. Natterer and H.R. Ott: J. Magn. Magn. Mater. **8** (1978) 87.

9) O. Peña, P. Rabu and A. Meerschaut: J. Phys.: Condens. Matter **3** (1991) 9929.

10) W.P. Wolf: J. Phys.(Paris) **32** (1971) Suppl. C-1, p.26

11) J. Yeomans: *Solid State Physics*, eds. H. Ehrenreich and D.Turnbull (Academic Press, Orlando, 1988) Vol.41, p.151

12) K. Sugihara, N.C. Yeh, M.S. Dresselhaus, and G. Dresselhaus: Phys. Rev. B **39** (1989) 4577.

13) A.J. Freeman: *Magnetic Properties of Rare Earth Metals*, ed. R.J. Elliott (Plenum Press, London, 1972) p.245.

Table I. Values of the effective moment μ_{eff} and the paramagnetic Curie temperature θ_p.

	$(CeS)_{1.2}NbS_2$			$(CeS)_{0.6}NbS_2$	
	H//c	*H//a*	*H//b*	*H//c*	*H⊥c*
			200 K < *T* < 250 K		
μ_{eff} (μ_B)	3.03	2.20	2.70	3.23	2.48
			T < 30 K		
μ_{eff} (μ_B)	1.73	1.72	1.50	1.61	1.67
θ_p (K)	3.8	−1.6	−2.6	3.4	−1.9

Table II. Values of fitted crystal field parameters and molecular field constants.

	$(CeS)_{1.2}NbS_2$	$(CeS)_{0.6}NbS_2$
B_2^0 (K)	18.0	16.5
B_4^0 (K)	0.26	0.62
B_4^4 (K)	11.0	9.3
$\gamma_{//c}$ (mol Ce/cm^3)	18	42
$\gamma_{\perp c}$ (mol Ce/cm^3)	−2.2	−5.6
cosθ	0.612	0.671
sinθ	0.791	0.742
$g_{//c}$	1.72	1.20
$g_{\perp c}$	1.85	1.91
$\mathcal{J}_{//c}$ (K)	1.2	1.4
$\mathcal{J}_{\perp c}$ (K)	−0.2	−0.5

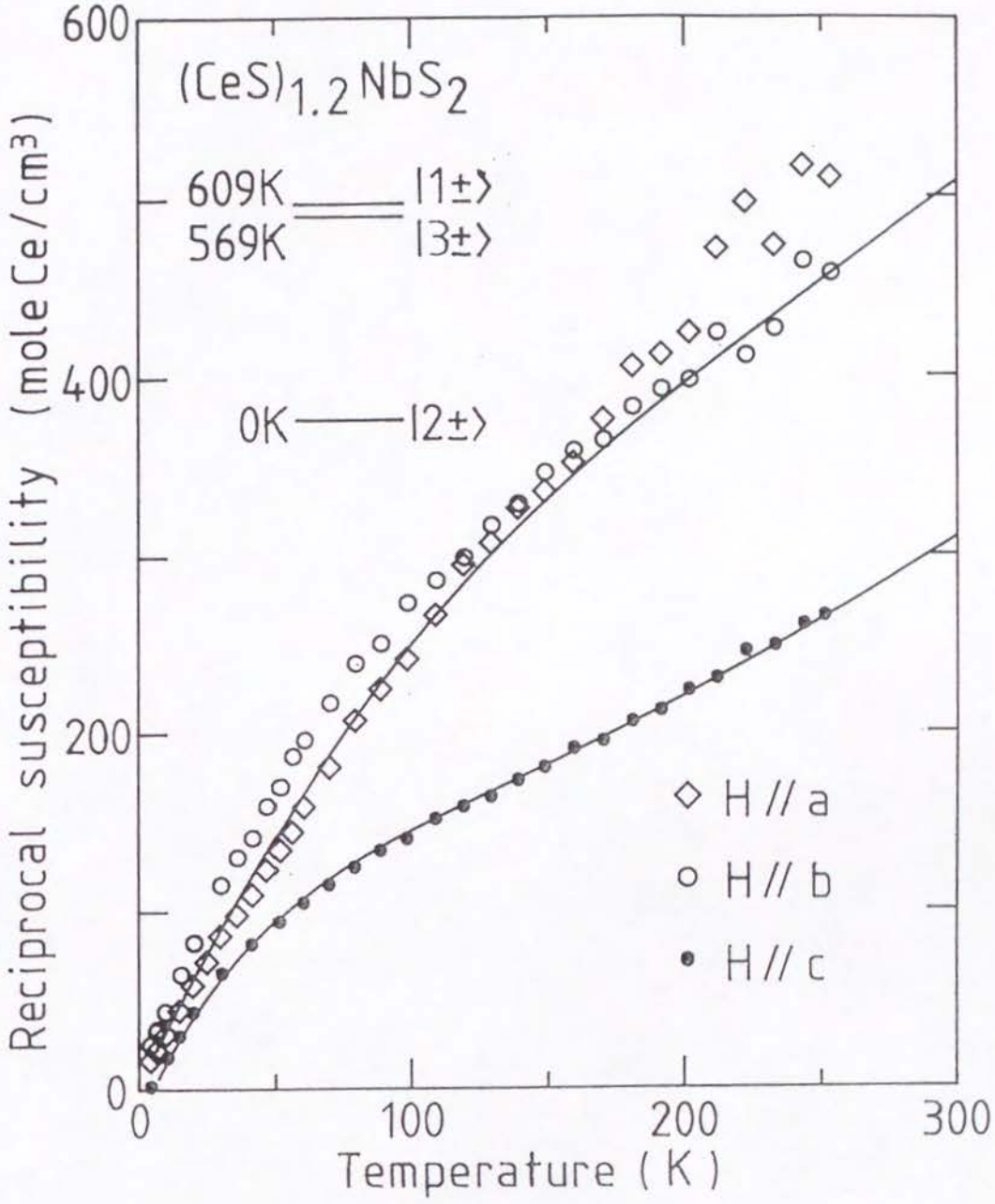

Fig. 1(a). Reciprocal magnetic susceptibility of $(CeS)_{1.2}NbS_2$ along all the three crystallographic axes. The solid lines are calculated ones using the crystal field and molecular field parameters given in Table I. The crystal field level scheme is also shown.

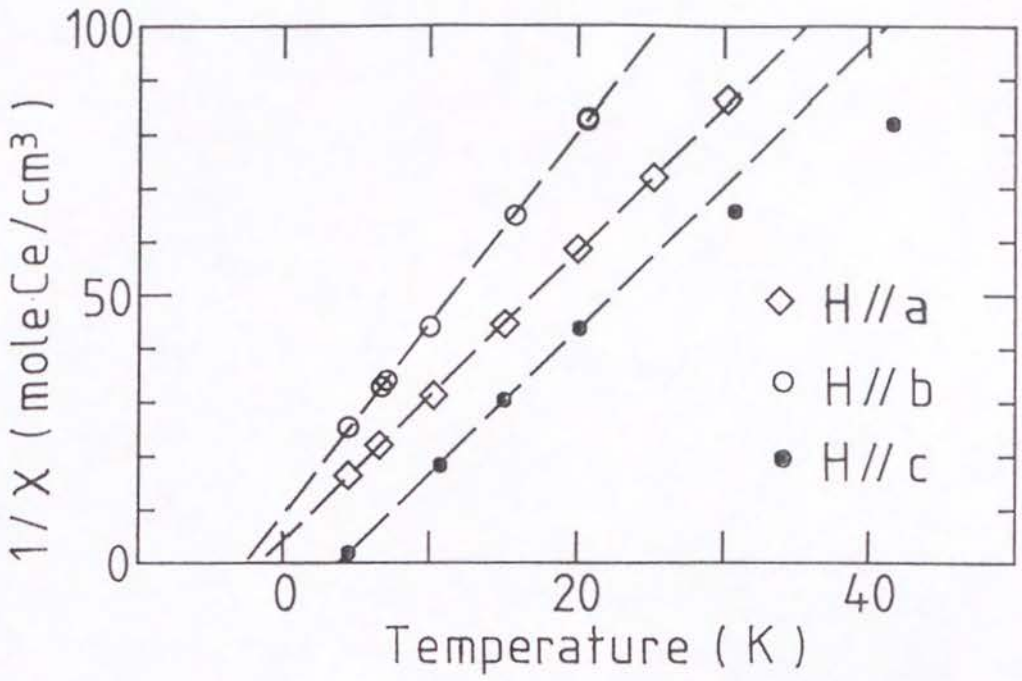

Fig. 1(b). An enlargement of the low temperature region of Fig. 1(a). The dashed lines indicate the approximate Curie-Weiss behavior.

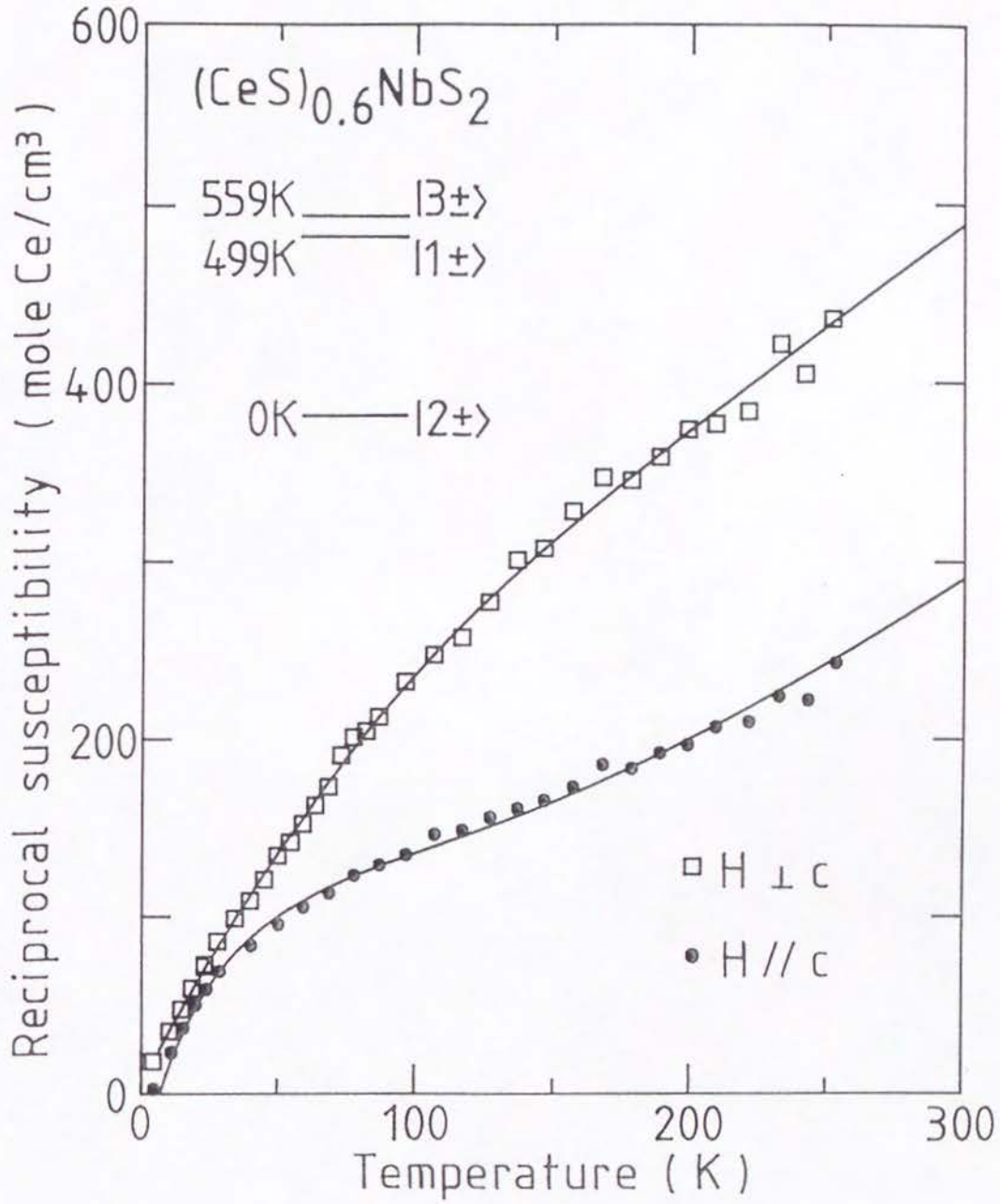

Fig. 2(a). Reciprocal magnetic susceptibility of $(CeS)_{0.6}NbS_2$ parallel and perpendicular to the *c* axis. The solid lines are calculated ones using the crystal field and molecular field parameters given in Table I. The crystal field level scheme is also shown.

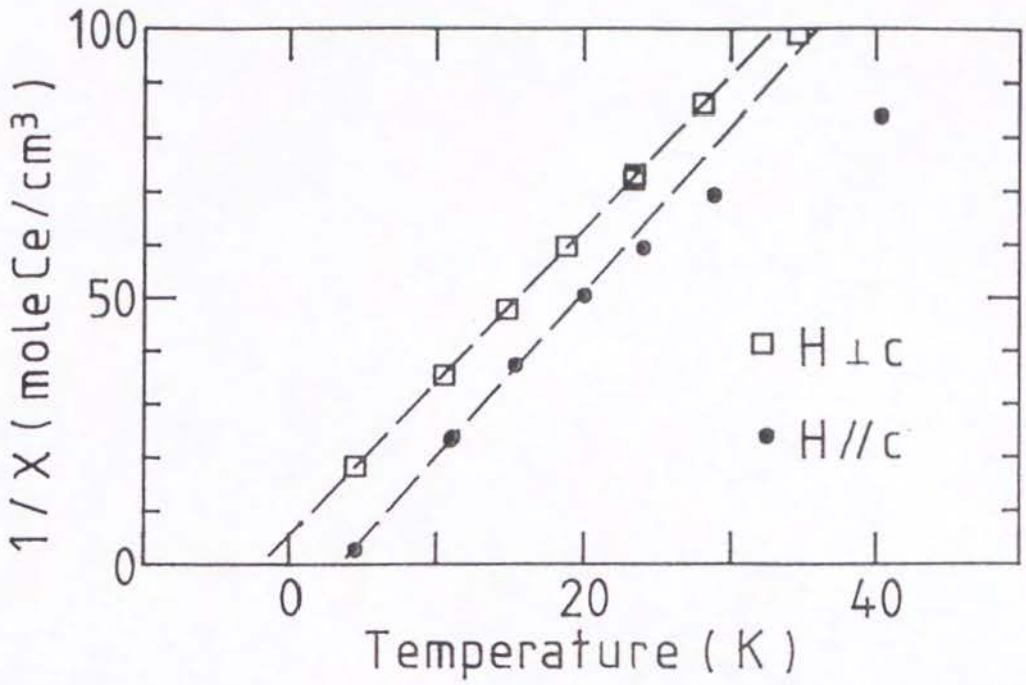

Fig. 2(b). An enlargement of the low temperature region of Fig. 2(a). The dashed lines indicate the approximate Curie-Weiss behavior.

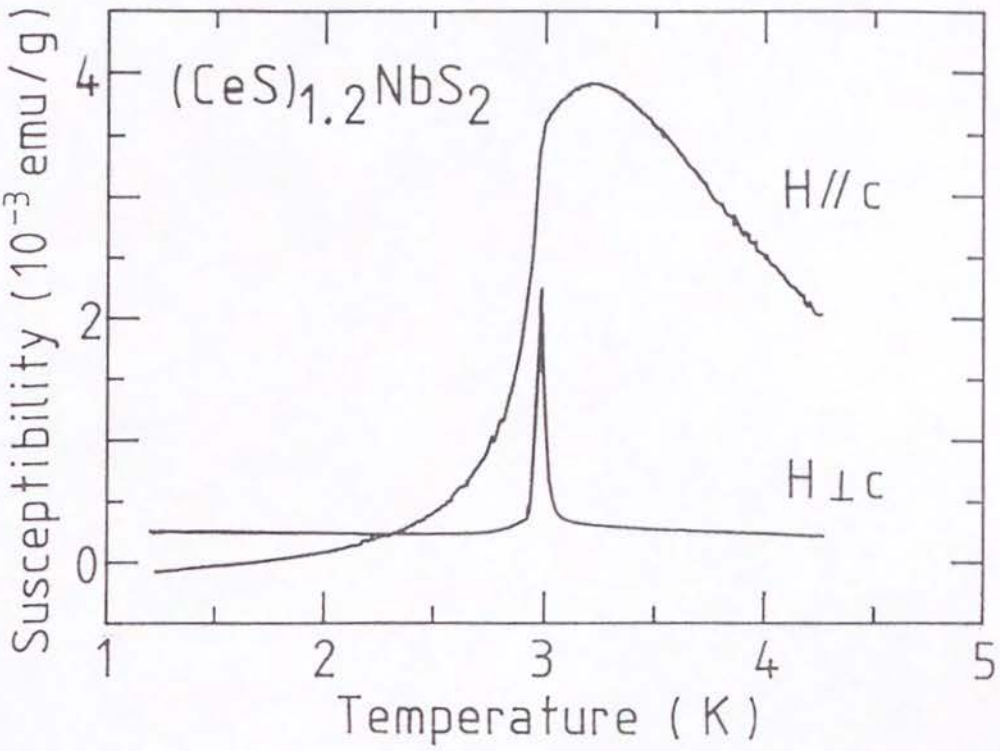

Fig. 3. Nearly zero field ac magnetic susceptibility of $(CeS)_{1.2}NbS_2$ around T_N along the fields parallel and perpendicular to the c axis.

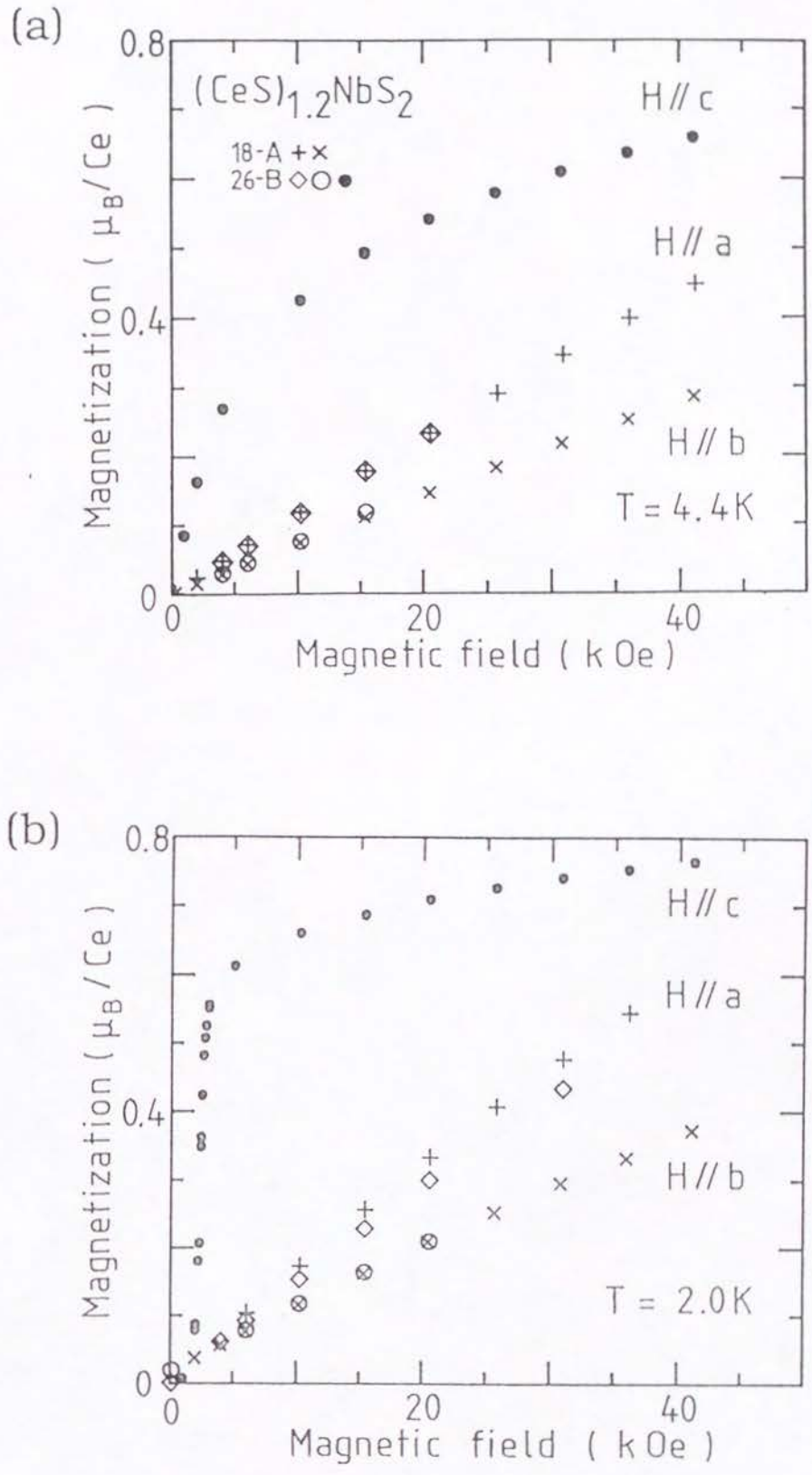

Fig. 4. Magnetization of $(CeS)_{1.2}NbS_2$ along all the three crystallographic axes at (a) 4.4K and (b) 2.0K. Two single crystals, #18-A and #26-B, were separately used.

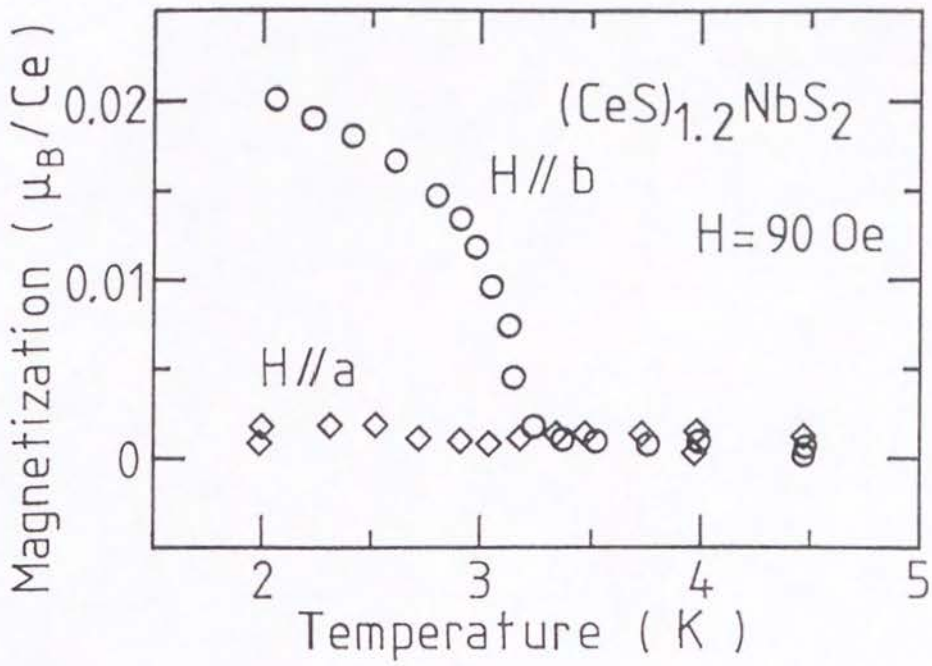

Fig. 5. The *a*- and *b*-axes magnetizations of $(CeS)_{1.2}NbS_2$ at 90 Oe.

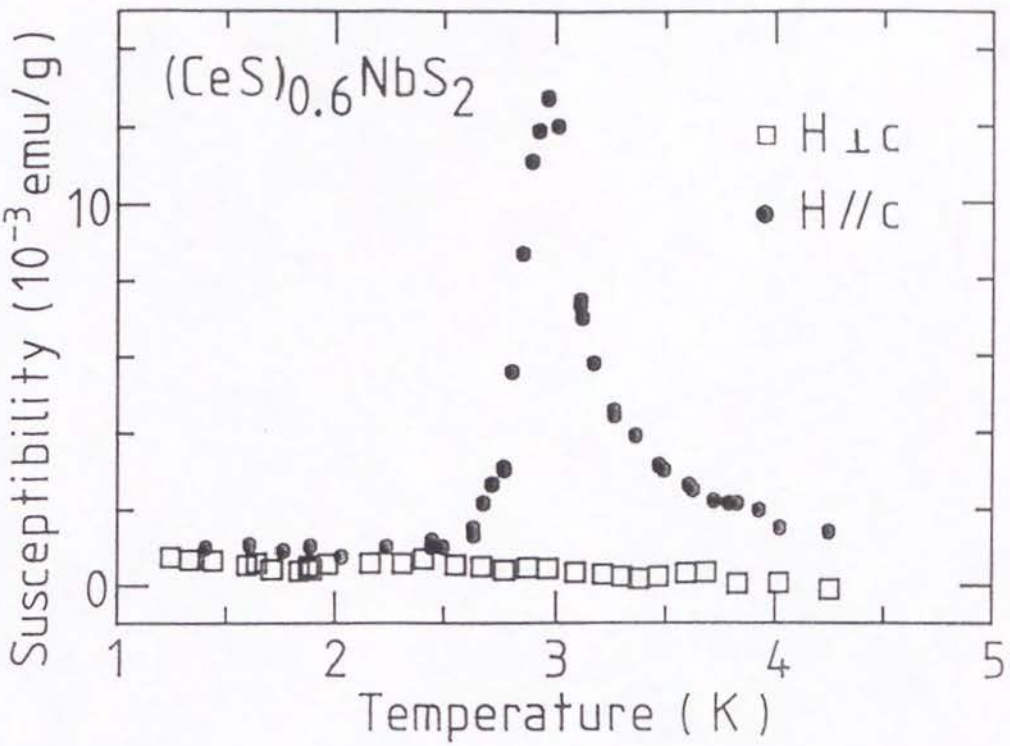

Fig. 6. Nearly zero field ac magnetic susceptibility of $(CeS)_{0.6}NbS_2$ around T_N along the fields parallel and perpendicular to the c axis.

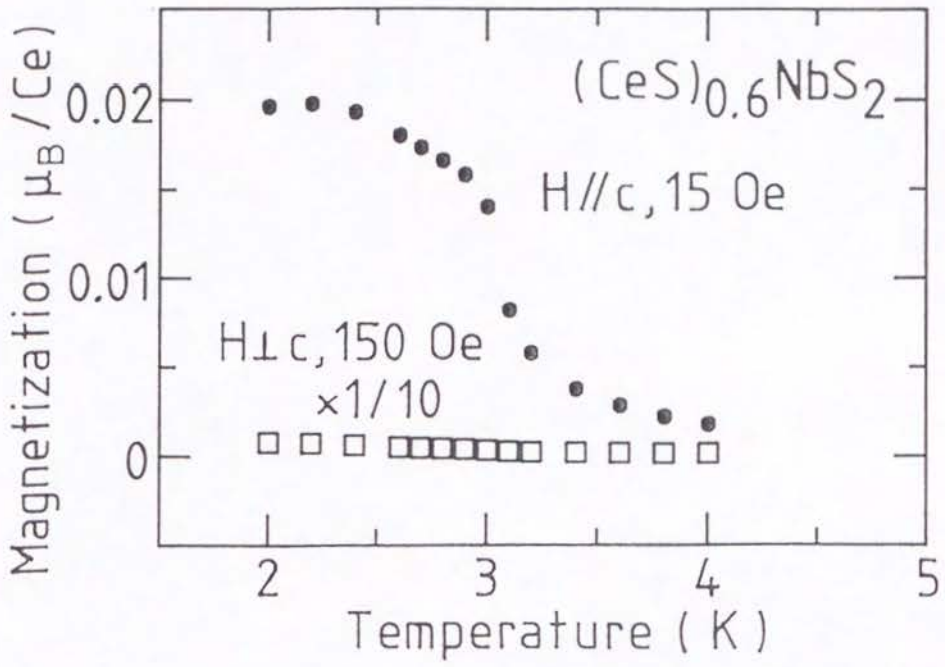

Fig. 7. The *c*-axis magnetization of $(CeS)_{0.6}NbS_2$ at 15 Oe. The magnetization perpendicular to the *c* axis at 150 Oe is also shown in a 1/10 scale for comparison.

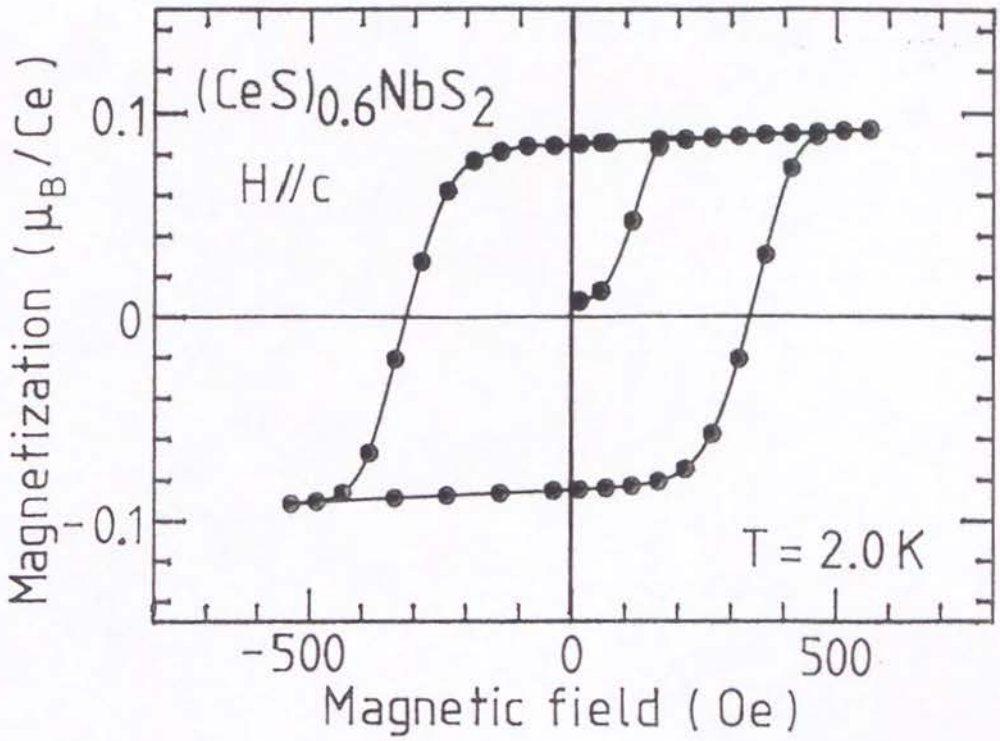

Fig. 8. Hysteresis loop of the *c* axis magnetization of $(CeS)_{0.6}NbS_2$ at 2.0K.

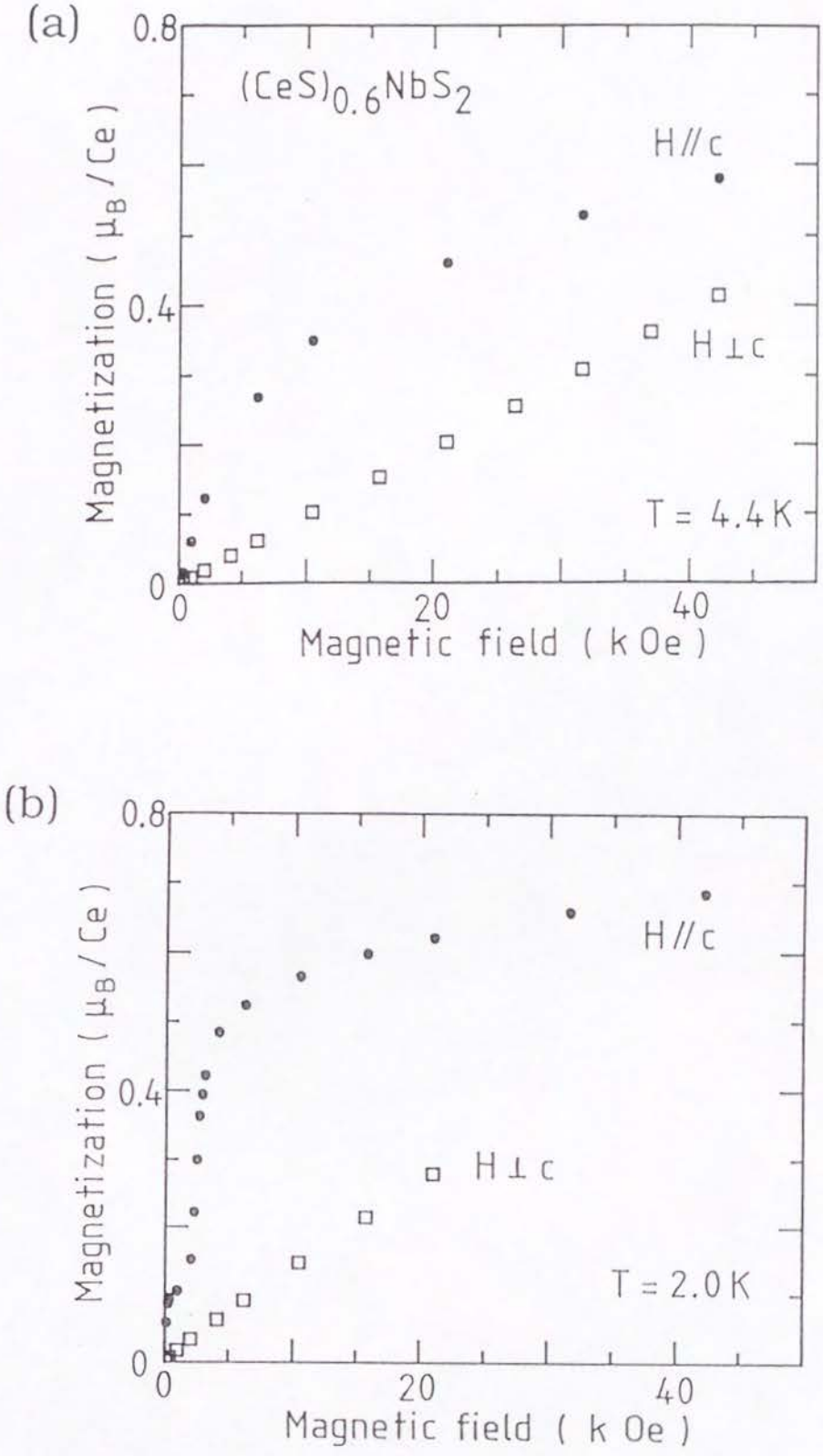

Fig. 9. Magnetization curves of $(CeS)_{0.6}NbS_2$ when the fields applied parallel and perpendicular to the *c* axis at (a) 4.4K and (b) 2.0K.

Chapter 7

Magnetic Properties of the Stage-1 Compound $(CeS)_{1.2}NbS_2$ by Means of the Specific Heat Measurement

§1. Introduction

In this chapter, we report the magnetic specific heat of $(CeS)_{1.2}NbS_2$. The specific heat measurement is a useful tool to examine the dimensionality of the magnetic system. The magnetic entropy and energy are estimated from the experimental specific heat and compared with the theoretical results for various types of $s=1/2$ Ising system.

§2. Experimental

Crystals of $(CeS)_{1.2}NbS_2$ were taken from the preparation batch #101. Several tens of thin crystal platelets with the total weight of 86.9 mg were used in the specific heat measurement. Taking into account the batch dependence of the Néel temperature mentioned in the preceding chapter, the Néel temperature of the sample (T_N=3.48 K) was determined from the ac magnetic susceptibility measurements made on the same sample that used for the specific heat measurement.

The specific heat was measured between 1.66 and 9.99 K using a standard adiabatic heat-pulse technique. The temperature jump was about 30 mK. The sample was attached to a holder with Apiezon-N grease. The heat capacity of the addenda was measured separately and subtracted from the data. The heat capacity of the sample was about three times larger than that of the addenda near T_N, while it was less than 8% of the total heat capacity above 8 K.

§3. Results and Discussion

The experimental specific heat of $(CeS)_{1.2}NbS_2$ is shown in Fig. 1. A well-developed anomaly can be seen, confirming the magnetic transition. In order to obtain the magnetic specific heat C_{mag}, it is necessary to subtract the electronic and lattice contributions from the total specific heat. Because of the limited temperature range of the measurements, it was difficult to extract the non-magnetic contributions from our own data and hence we tentatively used the specific heat of the non-magnetic compound $(LaS)_{1.2}NbS_2$ [1] as the non-magnetic contributions in $(CeS)_{1.2}NbS_2$.

We think, however, this procedure overestimated the non-magnetic contributions, since the resultant C_{mag} above 7 K decreases very rapidly as almost T^{-5}. Such a rapid decrease is quite unlikely for the magnetic specific heat at temperatures much higher than T_N, which in general decreases gradually as T^{-2}.

The peak of C_{mag} is located at 3.49 K, which is in accordance with T_N deduced from the susceptibility data within experimental accuracy. The C_{mag} curve around T_N is rather rounded off and the maximum value of C_{mag} reaches only a small value of $0.66R$, which is even smaller than the molecular field value of $(3/2)R$. These probably arise from not only the poor temperature resolution of the measurements but also the distribution of T_N due to the crystal imperfection or inhomogeneity. The shape of the anomaly in the C_{mag} curve does not resemble the lambda-type anomaly expected for three-dimensional magnetic systems, but is reminiscent of Onsager's solution for the two-dimensional Ising model, [2] which is characterized by a symmetric divergence around T_N and a large high temperature tail. Another feature to be mentioned is a fairly slow decrease of C_{mag} below 3 K, which appears as a shoulder in a C_{mag}/T vs. T plot [Fig. 1(b)]. For the ideal Ising spin system, the specific heat is expected to decrease exponentially at low temperatures. However in the present compound, the perpendicular component of the exchange interaction $J_{\perp c}=-0.2$ K exists besides the Ising term $J_{//c}=1.2$ K and hence spin wave excitations, which cause a power-law temperature dependence of the specific heat, may not be negligible in the temperature range under concern.

The magnetic entropy S and energy E can be calculated by numerical integration of

$$S(T_2)-S(T_1)=\int_{T_1}^{T_2}(C_{mag}/T)\,dT\ , \qquad (1)$$

and

$$E(T_2)-E(T_1)=\int_{T_1}^{T_2}C_{mag}\,dT\ . \qquad (2)$$

The magnetic specific heat below the lowest temperature of the measurements, T_L=1.66 K, was extrapolated as the straight line connecting the origin and the data point at T_L in the C_{mag}/T vs. T plot. From this extrapolation, $S(T_L)-S(0)$ and $[E(T_L)-E(0)]/RT_N$ were estimated to be 0.09 and 0.03, respectively, though these values can vary by up to 20% or so with extrapolation schemes. An appropriate extrapolation to $T\rightarrow\infty$ was impossible because of the false rapid fall of C_{mag} caused by the overestimation of the non-magnetic contributions. If the overestimation is corrected, C_{mag} around the highest temperature of the measurements, T_H=9.99 K, will be larger and decrease much more gradually, which will bring a certain contribution to the entropy and energy above T_H. The experimental values of the magnetic entropy and energy thus obtained are shown in Table I together with the theoretical values for the two-dimensional Ising (2DI) simple quadratic (sq) and triangular (t) lattices and the three-dimensional Ising (3DI) bcc and fcc lattices. [3]

The total entropy change of $0.60R$ is somewhat smaller than $R\ln 2(=0.69R)$ expected for the ground doublet. The discrepancy can

probably be accounted for by the experimental inaccuracy including the overestimation of the non-magnetic contributions and the uncertainty involved in the extrapolation. The total energy gain E/R $(=[E(\infty)-E(0)]/R)$ is 2.0 K, from which we can derive the exchange constant $\mathcal{J}_{//c}$=1.0K, using the relation $E/R=s'^2 z\mathcal{J}_{//c}/k_B$ and assuming the coordination number z=8 for the number of the nearest neighbors of Ce^{3+}. The obtained value of $\mathcal{J}_{//c}$=1.0 K is smaller than $\mathcal{J}_{//c}$=1.2 K derived from the magnetic susceptibility measurements in chapter 6, which will be explained as the shortage of the total entropy.

Despite the shortage of the total magnetic entropy and energy just discussed, we can clearly see the following two facts from the data summarized in Table I. First the entropy change above T_N is definitely larger than the theoretical values for the 3DI systems. Considering the overestimation of the non-magnetic contributions and a possible contribution from above T_H, the value may become still larger. Secondly, the system gains more than 60% of the total magnetic energy above T_N, which shows a remarkable contrast to the fact that the 3DI systems gain most of the magnetic energy (ca. 75%) below T_N. Both these facts indicate a significant short-range ordering above T_N and confirm the quasi two-dimensionality of this system.

However, compared with the 2DI systems, the present system shows one noticeable difference; the ratio of the total magnetic energy to T_N, i.e. $[E(\infty)-E(0)]/RT_N$, is only 70% of the theoretical values for the 2DI systems. When the experimental problems discussed above are removed, the total magnetic energy may

increase by 20% or so at most; even so this difference will remain distinct. This may be attributed to the fact that the ratio $[E(\infty)-E(0)]/RT_N$ decreases as the coordination number z increases. The CeS layer in $(CeS)_{1.2}NbS_2$ has the double-layer structure corresponding to a somewhat distorted two-atomic-plane thick (100) slice of the NaCl structure. [4] Consequently, each Ce^{3+} ion on one atomic-plane has four Ce^{3+} neighbors at 4.06 Å on the same plane and four at 4.50 Å on the other atomic-plane. These two types of neighbors have a similar nearly-90° superexchange path and approximately can be regarded as the nearest neighbors as a whole, i.e., z=8. In addition to this , a Ce^{3+} ion has the four next nearest neighbors, two at 5.73 Å and two at 5.77 Å, via a nearly-180° superexchange path. If these next nearest neighbors contribute to the exchange interaction, the coordination number becomes effectively still larger. To support this, it is to be noted that in EuS, which crystallizes in the NaCl structure, the next nearest neighbor exchange interaction via a 180° path differs only by a factor of 1/2 from the nearest neighbor one via a 90° path. [5]

In conclusion, the specific heat anomaly of $(CeS)_{1.2}NbS_2$ at T_N exhibits a pronounced high temperature tail characteristic of the two-dimensional magnetic systems. The analysis of the magnetic entropy and energy changes below and above T_N also confirms the quasi two-dimensionality of the present system. Compared with the usual 2DI models which take account of only the nearest neighbor interaction, the present system seems to be characterized by the effectively larger coordination number due to the double-layer structure.

References

1) D. Reefman, J. Baak, H.B. Brom and G.A. Wiegers: Solid State Commun. **75** (1990) 47.

2) L. Onsager: Phys. Rev. **65** (1944) 117.

3) C. Domb and A.R. Miedema: *Progress in Low Temperature Physics*, ed C.J. Gorter (North-Holland,Amsterdam,1964) vol.IV,ch.VI.

4) G. A. Wiegers, A. Meetsma, R. J. Haange, and J. L. de Boer: J. Solid State Chem. **89** (1990) 328.

5) P. Wachter: *Handbook on The Physics and Chemistry of Rare Earths*, eds. K.A. Gschneidner,Jr. and L. Eyring (North-Holland,Amsterdam,1979) vol.2,ch.19.

Table I. The magnetic entropy $S(T)$ and energy $E(T)$ in $(CeS)_{1.2}NbS_2$. The experimental values are compared with theoretical values.

	$(CeS)_{1.2}NbS_2$	2DI		3DI	
	present work	sq	t	bcc	fcc
z	8	4	6	8	12
$[S(T_N)-S(0)]/R$	0.34	0.31	0.33	0.59	0.59
$[S(\infty)-S(T_N)]/R$	0.25	0.39	0.36	0.11	0.10
$[S(\infty)-S(0)]/R$	0.60	0.69	0.69	0.69	0.69
$[E(T_N)-E(0)]/RT_N$	0.22	0.26	0.28	0.46	0.46
$[E(\infty)-E(T_N)]/RT_N$	0.36	0.62	0.55	0.17	0.15
$[E(\infty)-E(0)]/RT_N$	0.58	0.88	0.82	0.63	0.61

The number z is the coordination number. The experimental values were estimated from the measurements between T_L=1.66K and T_H=9.99K and the extrapolation to $T\rightarrow 0$. No extrapolation to $T\rightarrow\infty$ was made.
The theoretical values are taken from ref. 3.

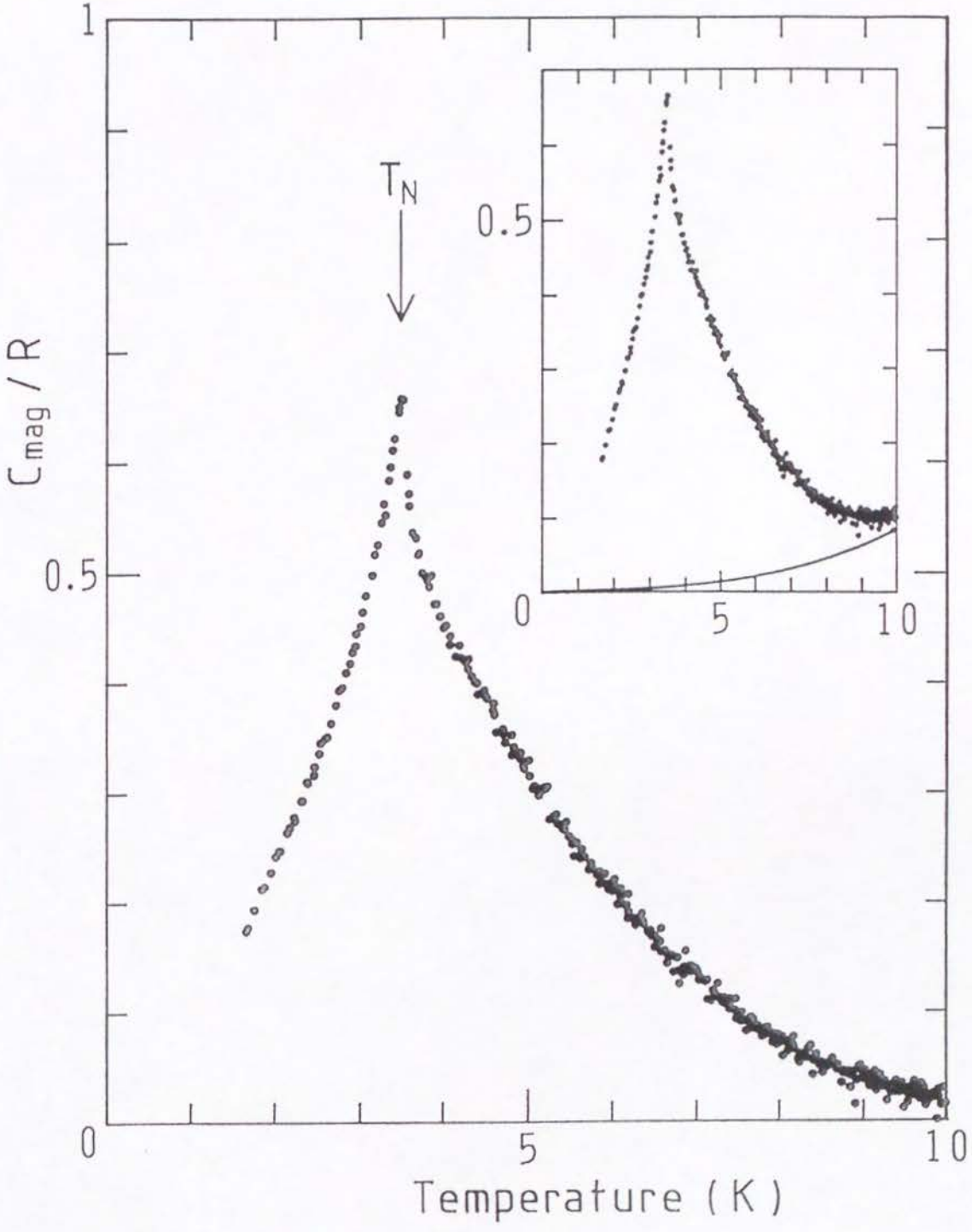

Fig. 1. (a) Magnetic specific heat C_{mag} of $(CeS)_{1.2}NbS_2$. Inset shows the total specific heat of $(CeS)_{1.2}NbS_2$ (dot) and that of $(LaS)_{1.2}NbS_2$ (solid curve) after ref.1.

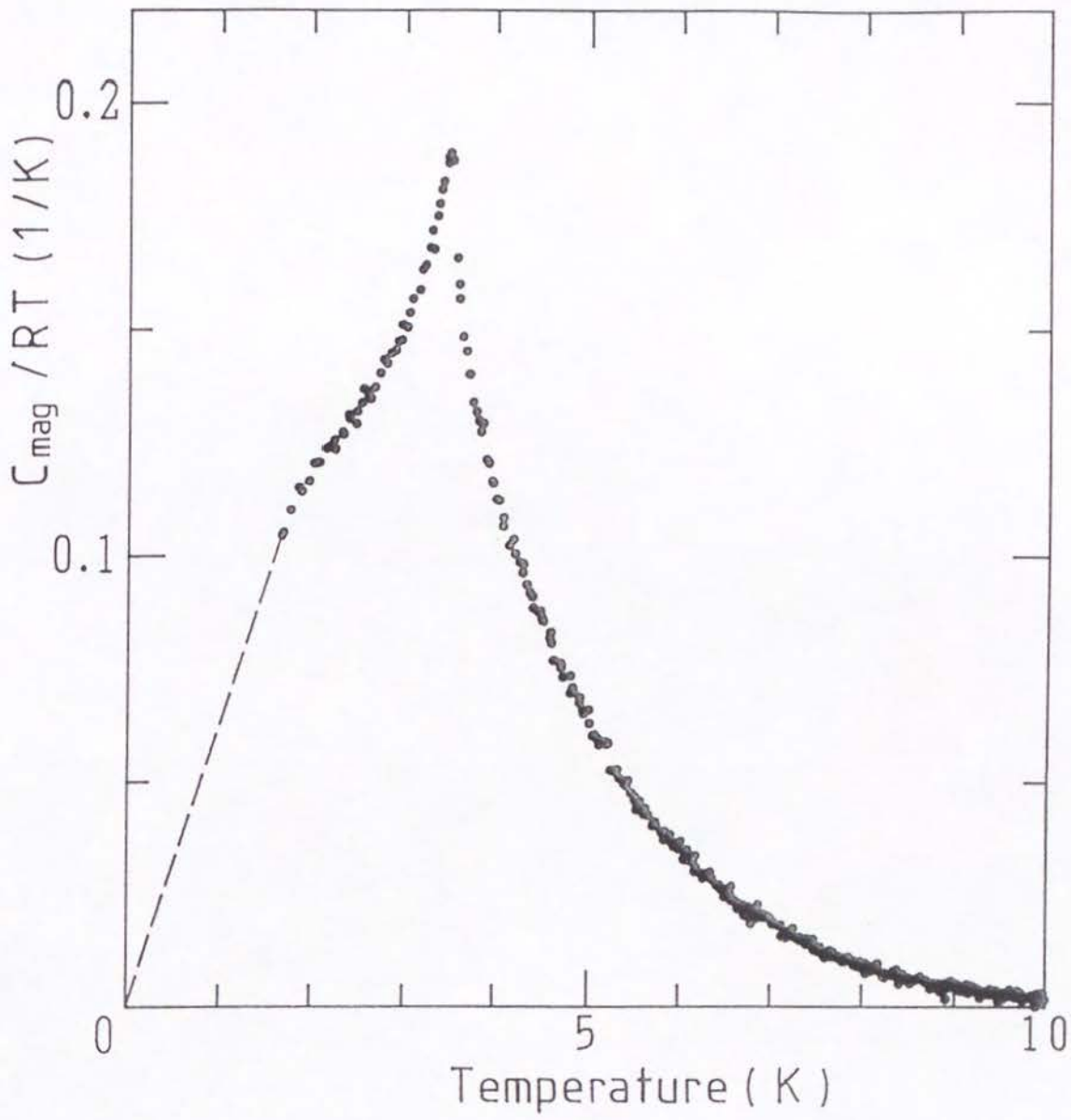

Fig. 1(b). C_{mag}/T vs. T plot. The dashed line represents straight extrapolation used to estimate the magnetic entropy and energy below the lowest temperature of the measurements.

Chapter 8

Concluding Remarks

The present transport and optical studies have shown that the electronic properties of the incommensurate layer compounds $(RES)_xNbS_2$ are fairly well interpreted within the rigid-band model for the host electronic band-structure. The optical reflectivity spectra of $(CeS)_{1.2}NbS_2$ and $(CeS)_{0.6}NbS_2$ have clearly demonstrated that the outlines of the host electronic structure are maintained in them. We have seen that the transport properties are dominated by the Nb d_{z^2} band. The drastic change in the Seebeck coefficient between the stage-1 and the stage-2 compounds has reasonably been accounted for by applying the rigid-band model. In spite of the possible formation of the intercalate band of RE 5*d* character, the intercalate RES layer seems to have very little contribution to the conduction. We will discuss this point again at the end of this chapter.

The magnetic study carried out on $(CeS)_{1.2}NbS_2$ and $(CeS)_{0.6}NbS_2$ has shown that these compounds can be modeled as quasi two-dimensional Ising systems. The large high temperature tail in the magnetic specific heat of $(CeS)_{1.2}NbS_2$ is a good evidence of the quasi two-dimensionality. Another interesting feature in their

magnetic properties is the anisotropy in the intralayer exchange interaction. (We are referring not to the anisotropy between the intralayer and the interlayer interaction but to the anisotropy between the exchange interaction acting on the c-axis component of spins, $J_{//c}$, and that on the basal-plane component, $J_{\perp c}$.) As mentioned in chapter 6, in general, the exchange interaction can be anisotropic when orbital contributions to the magnetic moments are large. In this connection, it will be interesting to investigate magnetic properties of $(GdS)_{1.2}NbS_2$, since Gd^{3+} is in the S state.

Finally we discuss why the intercalate RES layer is inactive in the conduction. As mentioned in chapter 4, if we impose the rigid-band model not only on the host band-structure but also on the intercalate one, we can expect that the intercalate band of RE 5*d* character crosses the Fermi level. However there has been found no evidence to support this in the transport study. The evidence against this have been found in the course of the magnetic study. The large crystal-field splittings observed in $(CeS)_{1.2}NbS_2$ and $(CeS)_{0.6}NbS_2$ indicate that the RE 5*d* electrons are not free carriers; otherwise the crystal field would effectively be screened by them.

This semiconducting nature of the RE 5*d* electron implies that the electronic band-structure of the intercalate RES layer differs from that of pristine RES. Moreover, it cannot be explained as far as we assume that the lattice periodicity of the intercalate layer is described in the sublattice unit cell of $a_{RES} \times b$; whatever charge transfer occurs and whatever modification of the electronic structure occurs, this unit cell always contains a fractional number of valence electron and hence some intercalate energy-band must

remain partially filled. Thus it seems necessary to take into account the extra periodicity forced on the intercalate RES layer by the host NbS_2 layer. In other words, we have to consider a superzone effect on the intercalate band-structure due to the mutual modulation.

From this point of view, the author speculates a mechanism that makes the intercalate RE 5*d* electrons semiconducting as follows. The true unit cell of the intercalate layer is much larger due to the extra periodicity brought about by the mutual modulation and hence we can expect a zone folding in the reciprocal lattice space and a gap opening at the new zone boundaries. In terms of the density of states, such gaps are only pseudo gaps, since the zone boundary does not necessarily lie on the same energy surface. However, even then, it will be more energetically favorable that all the RE 5*d* electrons above one of such gaps are transferred to the host layer so that the Fermi level can fall in the gap of the intercalate band than that some of RE 5*d* electrons remain above the gap. Moreover, the structural distortion of the intercalate layer may adjust itself at the cost of the lattice strain energy so as to more deepen the gap. Thus it is possible that the intercalate RE 5*d* band has a considerably small density of states at the Fermi level. Furthermore, if the density of states at the Fermi level is small enough, the screening of the random potential arising from impurities or defects becomes insufficient and even the remaining carriers will be localized.

In relation with this conjecture, it is worth while noting a recent report on related incommensurate layer compounds $(RES)_xVS_2$ (RE=La,Ce,Nd,Sm). [1] These compounds show a

semiconducting behavior of the conduction. This might imply that the above mechanism acts not only on the intercalate RES layer but also on the host VS_2 layer in these compounds. Further investigations are hoped.

The compound composed of two mutually incommensurate structural subsystems as the present compounds is a novel concept in the solid state physics. Further studies in this field will bring us a new insight into the solid state physics. The author hopes that the present study will offer a firm ground for future studies.

Reference

1) T. Kondo, K. Suzuki, and T. Enoki: Solid State Commun. in press